



Developing a Wildfire Surveillance Algorithm for Geostationary Satellites

A thesis submitted in fulfilment of the requirements for the degree of Doctor of Philosophy

Chathura Hasanka Wickramasinghe

Master of Science (Remote Sensing and Geographic Information Systems)
Asian Institute of Technology

School of Science

College of Science, Engineering and Health

RMIT University

December 2018

Declaration

I certify that except where due acknowledgement has been made, the work is that of the author alone; the work has not been submitted previously, in whole or in part, to qualify for any other academic award; the content of the thesis is the result of work which has been carried out since the official commencement date of the approved research program; any editorial work, paid or unpaid, carried out by a third party is acknowledged; and, ethics procedures and guidelines have been followed. I acknowledge the support I have received for my research through the provision of an Australian Government Research Training Program Scholarship.

Chathura Hasanka Wickramasinghe

06/12/2018

Acknowledgements

First of all, I would like to thank my parents for their support and encouragement without them I would not be where I am today. The work I have done during the last few years would not have been possible if my father hadn't got me on to JAVA programming. I am truly grateful for his foresight. I also want to thank my wife Arosha who has been supporting me and keeping me on track to finish my PhD.

All the work and success that I have achieved during the last three and half years was only possible, thanks to the great supervisory team that I was fortunate to have. I thank my supervisors Professor Simon Jones, who took me on board almost after nine months into my PhD. Providing invaluable guidance, knowledge and advice throughout this thesis. Dr Luke Wallace, for his knowledge, technical expertise, encouragement and support that he provided going out of his way to ensure work is completed on time. Dr Karin Reinke for her invaluable advice, knowledge and guidance.

I would also like to thank Dr Lal Samarakoon for his support to complete my Master's degree. Finally, I thank RMIT PhD International Scholarship (RPIS) programme and the RMIT school of Science for providing me with this PhD opportunity.

List of Publications

- Wickramasinghe, C., Jones, S., Reinke, K. and Wallace, L. *Development of a multi-spatial resolution approach to the surveillance of active fire lines using Himawari-8*. Remote Sensing, **8(11)**, p.932, (2016).
- Wickramasinghe, C., Wallace, L., Reinke, K. and Jones, S. : *Inter-comparison of Himawari-8 AHI-FSA with MODIS and VIIRS active fire products*. International Journal of Digital Earth, **pp.1-17**, (2018)
- Wickramasinghe, C., Wallace, L., Reinke, K. and Jones, S. *New algorithm implementation resulting in improvements in accuracy and resolution of SEVIRI hotspot products*. Remote Sensing Letters, **9(9)**, **pp.877-885**, (2018)
- Wickramasinghe, C., Wallace, L., Reinke, K. and Jones, S. *Multi-level wildfire surveillance using geostationary satellites*, (in review) Remote Sensing

Abstract

Wildfire surveillance is an important aspect of effective wildfire management, requiring near continuous observations to detect and monitor fires. Geostationary satellites have the potential to meet this challenge, capturing full disk images every 10 to 30 minutes at ground sample distances down to 500 m for some sensors. However, the MIR (Middle Infrared) and TIR (Thermal Infrared) channels on geostationary satellite sensors have a coarse ground sample distance of 2-4 km. Currently, fire detection algorithms depend on these channels to detect thermal anomalies. The coarse spatial resolution in the MIR and TIR channels limits the application of geostationary satellite for wildfire surveillance. This thesis looks to fully exploit the potential of geostationary satellites for wildfire surveillance through a multi-spatial and multi-temporal approach.

The first research question in this thesis, develops and tests an algorithm to improve the wildfire surveillance capabilities of the geostationary satellites. The new algorithm utilises the MIR, NIR and visible channels, linking them to biophysical processes on the ground. The MIR channel is used to detect thermal anomalies, the NIR channel is used to detect changes in vegetation cover, and the visible channel detects smoke from the fire. By combining these detections, or observations, fire surveillance can be achieved at the highest ground sampling resolution available (typically in the visible wavelength channels). Initial algorithm development and testing were conducted on the Advanced Himawari Imager (AHI) sensor onboard the Himawari-8 satellite. The MIR, NIR and RED channels on AHI have 2 km, 1 km and 500 m ground sampling distances respectively, enabling the new algorithm to detect 2 km thermal anomalies and 500 m fire-line pixels. Fire-line pixels is a new product designed to

detect the trailing edge of the fire.

Quantifiable methods for assessing algorithm performance in geostationary satellites are difficult to apply due to their high temporal resolution and lack of concurrent in-situ information. The second research question investigates methods for assessing the performance by considering the near continuous temporal sampling of geostationary satellites and the higher spatial ground sampling resolution afforded from LEO (Low Earth Orbiting) satellite observations. The study examines different evaluation methods and suggests a three-step process to provide the optimum performance evaluation for geostationary wildfire surveillance products, inter-compared with LEO satellite-based thermal anomaly detections.

Algorithm performance is further evaluated in research question three using the inter-comparison method developed in research question 2 and applied to case study fires over Northern Australia. Subsequently, the algorithm is evaluated using an annual dataset (2016) comprising of nine study areas across Australia (totalling 360.000 km²) stratified by tree canopy cover. The algorithm reported an omission error of 27 % at 2 km ground resolution when compared to VIIRS (Visible Infrared Imaging Radiometer Suite) hotspots over the nine study grids. In Northern Australia, the algorithm detected fires up to three hours before LEO observations due to the high temporal frequency of observations. Furthermore, in comparison to MODIS (Moderate Resolution Imaging Spectroradiometer) hotspots, there was a 73 % chance of detecting fire activity at the location of the MODIS hotspot, before the MODIS overpass. The algorithm also demonstrated a 40 % detection probability for fires less than 14 ha over Northern Australian woodlands. The fire-line pixels with a ground sampling distance of 500 m demonstrated a 25 % commission error when compared to VIIRS hotspots over the nine study grids. Over Northern Australia, this figure was 7 % inter-compared to Landsat-8 burnt scars.

The fourth research question applied the developed algorithm to the SEVIRI (Spinning Enhanced Visible and Infrared Image) sensor onboard the European Meteosat Second Generation (MSG) satellite. SEVIRI has an operational fire product (FIR (Active Fire Monitoring)) which provides 3 km ground resolution hotspots using the MIR and TIR channels. The algorithm initially developed for AHI was modified to work with SEVIRI 3 km MIR channel and the High-Resolution Visible (HRV) channel (1 km). An inter-comparison

of the modified algorithm with FIR products showed a 28% and 16% improvement in commission and omission errors respectively over a large case study fire in Portugal. The modified algorithm also improved the SEVIRI wildfire surveillance ground sampling resolution to 1 km taking advantage of the HRV channel.

The algorithm developed in this study demonstrates a novel approach to utilise geostationary satellites for wildfire surveillance with improved spatial resolution. Compared to the 2 km thermal anomaly hotspots derived through existing algorithms for AHI, the new algorithm provides 2 km thermal anomaly detections and 500 m fire-line pixels with performance comparable to that of medium resolution LEO satellites. Near-real time implementation of the algorithm has the potential to provide high temporal fire surveillance capabilities. The fire-line pixels from the algorithm could also be used to derive fire behaviour parameters such as heading and speed, providing an essential tool for wildfire surveillance in remote parts of Australia and other areas, where resources can only be deployed for a hand full of high-risk fires.

Contents

Acknowledgements	v
List of Publications	vii
Abstract	ix
List of Figures	xvii
List of Tables	xxi
1 Introduction	1
1.1 Background	1
1.1.1 Wildfire	1
1.1.2 Wildfire surveillance	2
1.2 Satellite-based wildfire surveillance	3
1.3 Validation/intercomparison of geostationary wildfire surveillance products	5
1.4 Gap in knowledge	7
1.5 Aim & research questions	8
1.6 Thesis structure	9
2 Multi-spatial active fire lines using Himawari-8	13
2.1 Introduction	14
2.1.1 Remote Sensing Fire Detection	15

2.2	Algorithm Development	16
2.2.1	AHI Data	18
2.2.2	Data Preparation	19
2.2.3	MIR Condition	19
2.2.4	NIR Conditions	20
2.2.5	RED Conditions	21
2.2.6	Fire-line and Hotspot Classification	21
2.3	Case Study Method	22
2.3.1	Case Study Fires	22
2.3.2	Cross-Comparison Evaluation Method	23
2.4	Results	23
2.5	Discussion	26
2.6	Conclusions	28
3	Intercomparison of Himawari-8 AHI-FSA with MODIS and VIIRS active fire products	29
3.1	Introduction	30
3.1.1	Geostationary Fire Detection Algorithms	31
3.1.2	AHI-Fire Surveillance Algorithm(AHI-FSA)	31
3.1.3	Algorithm Summary	31
3.2	Materials	32
3.2.1	Study Area	32
3.2.2	Comparison Products	33
3.2.3	MODIS Thermal Anomaly Products	34
3.2.4	VIIRS Thermal Anomaly Products	34
3.2.5	LANDSAT-8 Burnt Area Data	35
3.3	Imagery Navigation and Registration	35
3.4	Comparison Method	37
3.4.1	Active Fire-line Pixels and Thermal Anomaly Detections	37
3.4.2	Intercomparison of Thermal Hotspots	38

3.4.3	Calculation of Detection Time Differences	39
3.4.4	AHI-FSA Commission and Omission Error Calculation	39
3.5	Results	39
3.5.1	Thermal Hotspots Detection	40
3.5.2	Detection Time	41
3.5.3	AHI-FSA Commission and Omission Errors	43
3.5.4	AHI-FSA in a Single Fire	43
3.6	Conclusion	46
4	Multi-level wildfire surveillance using geostationary satellites	49
4.1	Introduction	50
4.2	Materials and Methods	51
4.2.1	VIIRS hotspots	51
4.2.2	Study Area	52
4.2.3	Tree/Vegetation Cover	53
4.2.4	AHI-Fire Surveillance Algorithm(AHI-FSA)	54
4.3	Intercomparison Method	56
4.3.1	Cloud cover	57
4.3.2	AHI-FSA 2 km commission and omission error calculations	58
4.3.3	AHI-FSA 2 km fire detection probability	58
4.3.4	AHI-FSA 500 m commission and omission error calculation	59
4.4	Results	59
4.4.1	Fire occurrence	59
4.4.2	Background temperature estimation	59
4.4.3	AHI-FSA 2 km Commission and Omission	61
4.4.4	Detection probability VIIRS hotspots	62
4.4.5	AHI-FSA 500 m Commission and Omission	63
4.5	Discussion	63
4.6	Conclusions	66

5	Implementation of a new algorithm resulting in improvements in accuracy and resolution of SEVIRI hotspot products	69
5.1	Introduction	70
5.1.1	The AHI-Fire Surveillance Algorithm(AHI-FSA)	70
5.1.2	Objectives	71
5.2	SEVIRI Active Fire Monitoring (FIR)	71
5.3	SEVIRI-FSA	71
5.4	Intercomparison	73
5.5	Case Study	74
5.6	Results and Discussion	74
5.7	Conclusion	78
6	Conclusion	79
6.1	Algorithm development	80
6.2	Algorithm evaluation	80
6.3	Algorithm Versatility	81
6.4	Synthesis	82
	References	87

List of Figures

1.1	Structure of thesis, research objectives and publications.	10
2.1	AHI-FSA algorithm flow diagram.	17
2.2	Study area map.	22
2.3	Compares the algorithm results with MODIS thermal anomalies hotspot products for Camballin fire on 10 September 2015. The sequence of images are from 01:30 UTC ten minutes before Terra a.m. (01:40 UTC) observation, followed by 01:40 UTC, and there after 03:00, 04:00, 05:00, 05:30 and again ten minutes before Aqua a.m. observation (05:50), followed by 06:00 and finally at 06:10 UTC. MODIS thermal anomaly product, which are at 1 km spatial resolution, are overlaid as pixel boundary in red . Algorithm results are overlaid in yellow which includes ‘fire-line’ as well as ‘possible fire-line’ pixels. The background image is a Landsat-8 post fire image acquired on 24 September.	25
2.4	Three fires in Western Australia on the 10 September 2015, the Fitzroy Crossing fire (on the left (a)), the Camballin fire (on the middle (b)) and the Broome fire (on the right (c)). The first two rows of images (1,2) shows fire detection at 01:40 and 06:00 UTC, respectively, from the algorithm (yellow) and MODIS thermal anomaly hotspots (red pixel boundary) with the Landsat-8 post fire image as the background; the last row (3) is a composite of all detected pixels from the algorithm 01:40 to 06:00 UTC, between MODIS Terra and Aqua observations.	26

3.1	The study area showing the land cover present and the 880 hotspots (MOD14) detected by MODIS during the study period from 02-06 and 25-29 July 2016.	33
3.2	Landsat-8 scene footprints used for burn area mapping in the study area. Shown in yellow are the digitised burn scars.	35
3.3	MODIS and AHI-FSA product detections are compared for a single fire on 6 th July 2016. The background image is that observed by the MODIS sensor onboard Aqua at 04:40 UTC. Fire detections from MODIS, AHI-FSA and AHI-FSA MIR condition at 04:40 UTC is shown in image (a). MODIS and AHI-FSA MIR condition detections are shown as pixel boundaries and AHI-FSA detections are shown in green. Figure (b) shows AHI-FSA detections from 00:00 to 04:40 in green illustrating that the AHI-FSA has detected essentially the same fire hotspots as MODIS, but as an earlier observation.	38
3.5	Daily comparison of AHI-FSA detections compared to MODIS hotspots on (a) 4 th July and (b) 6 th July 2016.	42
3.6	AHI-FSA early detection; fire near Bulman Weemol on 2 nd July 2016. (a) Histogram showing the time difference between the AHI-FSA detection and the nearest MODIS detection for the fire. (b) Image showing the spatial distribution of the detections(pixel detections are converted to point data) showing pre and post detections on top of the post fire image captured on 10 th July 2016 from Landsat-8.	42
3.7	Single fire monitoring near Claravale, Northern Territory, Australia via AHI-FSA and MODIS on 2016-07-04. The Figure shows the sequence of hourly aggregations of AHI-FSA fire-line pixels overlaid with near synchronous MODIS hotspot detections. Images (a) to (g) show detections from 00:00 to 06:50 UTC and (h) shows the total AHI-FSA fire-lines during the day overlaid with MODIS Terra and Aqua daytime detections. Landsat-8 post-fire imagery was used as the background, showing dark-green/brown area as burn area.	45
3.8	AHI-FSA fire-line pixels detection animation; large fire near Claravale on July 4 th .	46

3.4	AHI-FSA MIR condition thermal anomaly detection probability compared to MODIS, VIIRS hotspots and MODIS FRP values. AHI-FSA MIR hotspot counts shown as a histogram.	47
4.1	Study area grids selected across Australia for the study.	52
4.2	The percentage of VIIRS hotspots that fall within in each tree cover category in each grid for the year 2016. Tree cover data are based on Australia-wide vegetation height and structure data available at http://data.auscover.org.au/ (Joint Remote Sensing Research Program, 2012).	53
4.3	The intercomparison work flow illustrating how the AHI cloud mask is used when intercomparing AHI-FSA with VIIRS hotspots. AHI-FSA 2 km commission and omission errors are calculated with, and without, the AHI cloud mask. AHI-FSA 500 km commission/omission errors and AHI-FSA 2 km fire detection probability was calculated with the AHI cloud masked VIIRS hotspots data.	57
4.4	Commission and omission error calculation compared to VIIRS hotspots. Results for both intercomparison and cloud-free intercomparison are computed for a range of threshold values. The blue vertical lines mark the MIR threshold values used to calculate the balance AHI-FSA 500 m fire-line pixels in Section 4.4.5.	62
4.5	AHI-FSA 2 km detection probability of fires based on the number of VIIRS hotspots within the over lapping AHI MIR pixel. Detection probability is computed for three MIR-TH scenarios 1.0,5.0 and 10.0. Count of recorded number of fires for each fire class is shown by the column value in the right y-axis (on \log_2 scale) and the detection probability is shown in the left y-axis as a percentage of total hotspots in each class.	64
4.6	AHI-FSA 500 m commission and omission error are shown for compared to VIIRS cloud-free intercomparison data. (a) MIR-TH threshold values are selected to optimize AHI-FSA 500 m commission and omission error;(b) MIR-TH values are selected to minimize omission error; (c) MIR-TH values are selected to to minimize commission errors.	65

5.1	The study area covering two Landsat scenes path-204 row-31 and row-31 are shown. Background Landsat true colour imagery captured on 15th August 2016 shows the burnt area. MODIS MYD14A1(13:55 UTC) hotspots are also overlaid on top.	75
5.2	SEVIRI-FSA, FIR and MODIS hotspots detected at 10:30 UTC (a) and 13:55 UTC.	76
5.3	SEVIRI-FSA and SEVIRI-FIR detection as a percentage of the total detections and distance to Landsat-8 burn scars. Where distance categories are based on the maximum distance along the diagonal from the sensor pixel center. . . .	77
5.4	SEVIRI-FSA and SEVIRI-FIR detection as a percentage of the total detections and distance to the nearest MODIS hotspots.	77

List of Tables

2.1	AHI channels used in the AHI-FSA algorithm and application.	17
2.2	Weekly mean radiance/reflectance differences between two non-fire images for MIR, NIR and RED channels across five generic land-cover types. The maximum difference between two images was six days.	18
2.3	Total burnt area during the 10 September 2015 case study fires, mapped using MODIS Terra and Aqua 7-2-1 channel false colour imagery. The AHI-FSA detections from 01:40 to 06:00 UTC are combined to calculate the total area detected by AHI-FSA as in Figure 2.4 images a-3, b-3 and c-3. Commission error values are calculated based on the area detected using the AHI-FSA outside of the burnt area.	24
3.1	Primary specifications of the comparison datasets used in this study	34
3.2	Commission and omission errors for AHI-FSA detections synchronous with LEO hotspots.	41
3.3	AHI-FSA detection times compared to MODIS detections as a proportion of MODIS hotspots and average FRPs	41
3.4	The daily relative omission error between AHI-FSA, MODIS and VIIRS hotspot products, and the commission error in comparison to Landsat-8 burnt areas.	43

4.1	The number of VIIRS hotspot within each study grid in the study period (2016). As grids 3, 4, 5, 6 and 7 have less than 500 VIIRS hotspots they were not analysed further.	54
4.2	The percentage of VIIRS hotspots pixels that are unobstructed by the AHI cloud mask for three scenarios. When AHI cloud mask is applied only for the fire day, when a minimum of three days of cloud free data are available to compute the non-fire day image from 14 day period and finally when minimum of four day of cloud free data are required for non-fire days image computation.	60
5.1	AHI and SEVRI channel comparison.	72
5.2	The Omission and Commission rates of the FIR and FSA algorithm. Omission error is calculated against MODIS hotspots, while commission is calculated against Landsat-8 burnscars.	78

1

Introduction

1.1 Background

1.1.1 Wildfire

Wildfire, often referred to as bushfire in Australia, is the burning of vegetation such as forest, woodland or grassland. Fire supports ecological diversification, and also breaks down organic matter into soil nutrients (Melorose et al., 2006). Wildfire also contributes to changes in global climate and carbon cycles. Increasing dry season periods and record high temperatures have contributed to an overall increase in wildfire frequency and intensity. Bowman et al. (2009) reported increases in the incidence of large, uncontrolled fires on all vegetated continents suggesting that global climate change will continue to increase the risk of high-intensity wildfire events. Jolly et al. (2015) showed from 1979 to 2013 there was a doubling of global

fire prone areas and a 18.5% increase in fire season duration. When fires occur close to populated areas, there is the potential for high social and economic losses. There are also health risks due to smoke and haze resulting from the fire. Conservation efforts can also be hindered, causing a negative impact on the environment.

One of the largest fires in recent years was the 2003 Siberian Taiga fire, which burned over 190 000 km² of land (Ploscariu, 2018). In 2014, the Northwest Territories fires in Canada destroyed 33 000 km². The smoke from the fire was reported to reach far as 2000 km south of the fire (Ploscariu, 2018). Australia has also recorded some of the world's largest wildfires in recent history. In 1939, the Black Friday fires caused the loss of 71 lives and destroyed an area of 20 000 km² (Booth, 2009). More recently the Black Saturday fire in 2009 destroyed 2000 houses and 173 lives were lost (Booth, 2009). With the rapidly growing population and the expansion of outer suburbs into fire-prone areas, more and more people are potentially exposed to wildfire. Thus, early detection and effective wildfire management through high-frequency wildfire surveillance tools are critical for minimising the impact of wildfire.

1.1.2 Wildfire surveillance

Wildfire management involves a number of activities ranging from fuel management, fire prediction and modelling through to fire suppression and prevention (Minas, 2013; Martell, 2007). Fuel management involves controlled burning of undergrowth to reduce fuel hazard, which minimises ignition and spread of wildfire. Communication tools such as fire danger ratings express an assessment of the fire environment taking into account the ignition, rate of spread, the difficulty of control and potential fire impact (Merrill et al.; Merwe, 2015), providing a simple matrix for assessing the fire risk and informing precautions. Each of these key activities supports fire suppression in the event of a wildfire. However, early fire detection is key to effective fire suppression. The earlier the fire is detected after the initial ignition, the higher the chance of control over the fire, with fewer resources. Near real-time wildfire surveillance systems have been shown to provide valuable information for fire management authorities to act quickly (Hefeeda & Bagheri, 2007; Watts et al., 2012; Stipani et al., 2010).

There are a number of platforms with a range of capabilities that are currently used for

wildfire surveillance. Ground-based systems such as manned watchtowers and smoke detection sensor networks are used in high wildfire risk areas. A community-based approach to report fire activity is also commonly used for wildfire surveillance near populated areas (Slavkovikj et al., 2014). Aerial sensor-based systems, on the other hand, can provide relatively large area coverage compared to ground systems. Such systems are ideal for targeted fire surveillance after the fire has been initially reported, providing a detailed and frequent overview of the fire. However, having a dedicated aircraft fly daily to detect fire activity can be expensive (Slavkovikj et al., 2014). Ideal fire detection platforms should be able to provide continuous monitoring over a large area with a low operational cost. A satellite-based system can provide near continuous monitoring with substantial area coverage and low operational cost. A number of satellite-based thermal hotspot products are currently used for wildfire surveillance around the world.

1.2 Satellite-based wildfire surveillance

There are number of satellite-based thermal hotspot products that exist for wildfire detection and surveillance. Low Earth Orbiting (LEO) satellite sensors such as, the Moderate Resolution Imaging Spectroradiometer (MODIS), the Advanced Very High-Resolution Radiometer (AVHRR) and the Visible Infrared Radiometer Suite (VIIRS) provide global coverage with 375-1000m ground sampling resolution. In Australia a number of web mapping services provide fire hotspots information derived from satellite imagery. These include, the Sentinel Hotspots provided by Geoscience Australia, MyFireWatch from the Western Australian Land Information Authority and North Australia Rangelands Fire Information Platform by Charles Darwin University. These service depend on associated MODIS, AVHRR and VIIRS thermal anomaly products. As these sensors are based on low earth orbiting satellites, the total combined temporal resolution from the three sensors are limited to 6-7 observation per day over a given area. Thus, only providing limited wildfire detection and surveillance capabilities.

In contrast, geostationary satellites can provide near real-time surveillance with observations every 10–20 min covering a full disk area. Geostationary satellite-based earth

observation sensors have coarse ground resolutions (2–4 km) compared to the polar orbiting satellites (0.0375–1 km), yet, due to their geostationary orbit, they can provide high temporal observations every 10 to 30 min making it ideal for wildfire monitoring in terms of temporal resolution. Currently, the GOES (Geostationary Operational Environmental Satellites) satellite covers most of North and South America, EUMETSAT (European Organisation for the Exploitation of Meteorological Satellites) covers Europe and Africa, and the Himawari-8 satellite covers most of Asia including Australia. The main purpose of these three satellites are for weather monitoring, however, they are also used for wildfire detection. For example, the Wildfire Automated Biomass Burning Algorithm (WF-ABBA) provides a 4 km hotspot product over Northern and Southern America with a 30-minute temporal resolution (Prins & Menzel, 1994a; Pereira, 1999). The SEVIRI (Spinning Enhanced Visible and Infrared Image) Active Fire Monitoring (FIR) product is available every 15 minutes with a 3 km ground resolution over Europe and Africa (Laneve et al., 2006; Sifakis et al., 2011a).

The idea of detecting fires at a sub-pixel level using an earth observation satellite with more than one channel in the thermal infrared region was originally introduced by Dozier (1981). This method is based on the premise that *"If one part of a pixel is much warmer than the remainder, that warm part will contribute proportionally more radiance to the signal in shorter wavelengths in the thermal Infrared than in longer wavelengths"* (Dozier, 1981, p. 221). Taking on this approach Kaufman et al. (1998) introduced a contextual threshold-based algorithm to detect thermal anomalies using earth observation satellites. Contextual thresholds enable the algorithm to distinguish thermal variation due to fire from the background pixels (Justice et al., 2002a; Morgan et al., 2001; Roberts & Wooster, 2008a). The current MODIS active fire algorithm version 4 (Giglio et al., 2008a) is the latest version of the initial Kaufman et al. (1998) algorithm with improvements made to detect smaller fires and reduce the number of false detections. MODIS has two thermal anomaly products MOD14 and MYD14 providing 3-4 detections per day using the Terra and Aqua satellites respectively. Over Australia MODIS has shown a 1% commission error and 26% probability of detecting a fire the size of 27 ASTER (Advanced Spaceborne Thermal Emission and Reflection Radiometer) sensor pixels (30 m) equating to 0.6 km² (Giglio et al., 2016). VIIRS sensor onboard the Suomi National Polar-orbiting Partnership (Suomi-NPP) satellite provides 375 m and 750 m ground

resolution thermal anomaly hotspot product with twice daily coverage (Schroeder et al., 2014). VIIRS thermal anomaly detection algorithm is also based on the MODIS active fire detection algorithm. VIIRS has demonstrated 100 % detection capability of fires larger than 100 ha over the Northern Territory of Australia (Oliva & Schroeder, 2015).

The Automated Biomass Burning Algorithm (ABBA) is another fire detection algorithm that was developed for the GOES sensor (Prins et al., 1998). The algorithm uses the visible wavelength channels to correct for surface albedo, that aids in reducing the effects of solar contamination in the thermal channels. It has been demonstrated that the GOES sensor with 4 km thermal channels can detect fires as small as 0.9 ha at 838 K (Kelvin) using the ABBA algorithm (Prins et al., 1998). In the year 2000, a modified version of the algorithm WF-ABBA (WildFire-ABBA) was implemented on the GEOS satellite that provides near real-time wildfire surveillance every 20 min with 4 km ground sampling resolution. WF-ABBA reported a detection probability of 80 %, for fires over 500 ha in size and a minimum detectable fire size of 2.1 ha (Koltunov et al., 2012). Over Europe, the SEVIRI sensor onboard MSG satellite is used to provide wildfire surveillance data every 30 min at a 3 km ground sampling resolution. Calle et al. (2006b) showed that SEVIRI was able to detect fires less than 1 ha in size at 600 K. Overall, both LEO and geostationary satellite-based sensors are used for wildfire surveillance; LEO sensors providing higher spatial resolution and lower temporal resolution, whereas the geostationary sensors providing higher temporal resolution with coarse spatial resolution.

1.3 Validation/intercomparison of geostationary wildfire surveillance products

Validation and intercomparison is an important part of assessing the performance of an algorithm. The term intercomparison is used when results are presented compared to another product or data-set with known errors. Whereas data-sets used for validation must not contain known errors and are considered as the truth. In the case of wildfire surveillance the best validation data-set would be on ground wildfire records. However, collecting a large

enough data-set to validate a wildfire hotspot product across different landscapes and seasons can be challenging. Thus the majority of the work done on evaluating geostationary wildfire surveillance algorithms have been based on pixel-wise intercomparison with higher resolution LEO products (Xu et al., 2017; Roberts & Wooster, 2008b; Schroeder et al., 2008a; Calle et al., 2008; Feltz et al., 2003). For example, Schroeder et al. (2008a) used 30 m ASTER and Landsat 7 Enhanced Thematic Mapper Plus (ETM+) sensors to evaluate the performance of MODIS and WF-ABBA hotspots products.

The two main metrics used to understand the performance wildfire surveillance algorithm is through commission error (that is, the percentage of detections that are false detections) and the omission error (that is, the percentage of reference detections that have not been detected) calculations. The significance of the error varies depending on the intended application. For example, when wildfire detections are used for early warning, commission errors could incur added costs to fire managers who have to send out fire suppression teams in anticipation of a wildfire (Koltunov et al., 2012).

Products from low earth orbiting MODIS and VIIRS sensors provide higher spatial resolution compared to geostationary satellites. For example, compared to Himawari-8 AHI (Advanced Himawari Imager) thermal channels, which have a 2 km spatial resolution at nadir, the MODIS thermal anomaly product is four times smaller (1 km at nadir) and VIIRS hotspots are 25 times smaller (0.375 km at nadir). This discrepancy between spatial and temporal resolutions creates challenges for intercomparison analyses. Commonly, a pixel-wise intercomparison is conducted using near-synchronous geostationary observations to that of the LEO satellite overpass considering a single observation for the available high temporal data-set. Koltunov et al. (2012) presented the need to aggregate the fire pixels across time and space to account for timeliness nature of geostationary products, and to minimise the bias toward low temporal resolution when intercomparing with LEO hotspot products.

The minimum detectable fire size is also an important parameter in evaluating the performance of fire surveillance algorithms. The majority of fires detected by geostationary satellites are sub-pixel fires due to the coarse ground resolution of the satellites. Morissette et al. (2005b) used logistic regression to determine the probability of MODIS hotspots detecting a fire that is detected by the higher spatial resolution ASTER sensor. A similar

approach was also used by Schroeder et al. (2008a) to calculate the fire detection probability of WF-ABBA algorithm compared to ASTER hotspots. This technique provides an estimation of the sub-pixel fire detection capabilities of the algorithm intercompared to higher resolution products.

1.4 Gap in knowledge

Himawari-8 is a new geostationary weather satellite launched in October 2015 by the Japan Meteorological Agency (JMA). Onboard is the Advanced Himawari Imager (AHI) 16 channel multi-spectral sensor. This satellite provides improved temporal and spatial resolutions over its predecessor, Multi-functional Transport Satellites (MTSAT). The potential of the satellite for wildfire surveillance is yet to be fully explored. Recent studies conducted on the feasibility of using AHI for thermal anomaly detection have shown great potential for wildfire detection. Xu et al. (2017) using the FTA algorithm, and Xu & Zhong (2017) by implementing the MODIS thermal anomaly detection algorithm, have demonstrated the potential of AHI for thermal anomaly detection at a 2 km spatial resolution. Hally et al. (2018) adopted a multi-temporal approach by using the high temporal observations available via AHI for fire detection. The existing body of work on wildfire detection using satellite sensors has been focused on thermal anomaly detection. In contrast, the fire surveillance capabilities, to continuously track a fire have been less explored. AHI provides an opportunity to utilise the 1 km near infrared (NIR) and 500 m RED channels to improve the wildfire surveillance product ground sampling resolution. The possibility to use MIR, NIR and visible channels, to detect biophysical processes on the ground due to fire and linking them to wildfire surveillance have not been explored. For example, the NIR channel may be used to detect changes in vegetation due to burning, and the changes in RED reflectance may be used to pickup smoke from the fire. A common attribute in almost all the currently operational geostationary earth observation sensors is the comparatively higher resolution visible channel. The possibility of using this attribute to improve the wildfire surveillance using geostationary satellites is an opportunity that should be investigated.

It is a standard practice for any new remote sensing algorithm to undergo an accuracy

assessment, usually in the form of an intercomparison or validation analysis. As highlighted by (Koltunov et al., 2012), there is recognition that any evaluation method should take into account the high temporal frequency and timeliness offered by geostationary products. Evaluation of geostationary satellite hotspots products has mostly been conducted intercompared with synchronous LEO hotspots. Such an approach does not account for the high-frequency data available in the geostationary product. For example, Himawari-8 satellite provides imagery every ten minutes, a total of six observations per hour. A fire detected by LEO satellites at the time of overpass could be missed by the coarse resolution geostationary satellites. This introduces a false negative in an intercomparison with a LEO satellite based hotspots product. However, when the fire has grown sufficiently in size and/or intensity that is detectable by the geostationary satellite, it will be a true detection. This heightens the need for a new method to evaluate the geostationary satellite-based wildfire surveillance products. A method that will provide a performance matrix intercompared with LEO hotspots products taking into account the high-frequency nature of geostationary satellite-based products.

1.5 Aim & research questions

This thesis investigates new approaches to utilising geostationary satellites for wildfire surveillance. Attributes from geostationary earth observation sensors are explored to identify new techniques and solutions for wildfire surveillance. Furthermore, optimum methods for evaluation of geostationary wildfire surveillance products are also explored. This thesis investigates the following four Research Questions (RQ):

RQ 1: How can the attributes of geostationary satellites be combined to create a new algorithm to provide improved wildfire surveillance?

Wildfire surveillance via geostationary satellites has been limited due to the dependency on the coarse resolution MIR and TIR channels. Almost all geostationary earth observations sensors have higher spatial resolution visible channels. It is possible to detect biophysical changes due to fire such as smoke and burning of vegetation through these visible channels. The first research question investigates the unexplored potential of using the higher resolution

visible channels to identify the location of the sub-pixel fire within the thermal anomaly detected pixel, thereby improving the spatial resolution of thermal-based outputs.

RQ 2: What are the best methods for evaluating the performance of geostationary-based wildfire surveillance algorithms?

The body of existing work evaluating the performance of wildfire detection algorithms indicates a number of methods or techniques are available. However, no single method for evaluating geostationary-based wildfire products has been clearly defined in the literature. In addition, existing methods to evaluate high-frequency wildfire surveillance products have failed to take into account the discrepancy between the resolutions of the high temporal observations available from geostationary satellites, compared to those observations from LEO satellites. Thus, it becomes important to investigate the suitability of existing evaluation methods, and potentially develop new approaches for the evaluation of high-frequency wildfire products when intercompared with low-frequency wildfire products.

RQ 3: What is the performance of the new algorithm intercompared with standard satellite fire products across selected fire-prone landscapes?

Evaluating the performance of the algorithm is important to understand the limitations of the algorithm and also to understand the errors of commission and omission in the context of currently used wildfire surveillance products. The performance of the new algorithm developed is quantified using case study fires, as well as an annual data-set across different landscapes over Australia.

RQ 4: Can the new algorithm be applied to other geostationary sensors?

The new algorithm development and testing are performed initially on the Himawari-8 satellite. This research question explores the possible application of the algorithm to other sensors. To test the algorithm in other platforms, a modified version of the algorithm is tested on the European SEVIRI geostationary sensor.

1.6 Thesis structure

This thesis consists of six chapters. Chapter 1 introduces the research aim and research questions. Chapter 2 explores the attributes of the Himawari-8 AHI sensor and develops

a new wildfire surveillance algorithm. In chapter 3 different methods for the evaluation of geostationary wildfire surveillance algorithms are explored. Chapter 4 evaluates the performance of the new wildfire surveillance algorithm over Australia using AHI sensor onboard the Himawari-8 satellite. Chapter 5 looks at a modified version of the new algorithm implemented on the SEVIRI sensor onboard the European Meteosat Second Generation satellites, exploring the platform-independent properties and adaptability of the algorithm. The thesis is concluded in Chapter 6, where the study findings are discussed and an outlook of the future research is presented.

		Chapter 1: Introduction and Background
RQ 1		Chapter 2: Development of a multi-spatial resolution approach to the surveillance of active fire lines using Himawari-8. Wickramasinghe, C.H., Jones, S., Reinke, K. and Wallace, L., 2016. Development of a multi-spatial resolution approach to the surveillance of active fire lines using Himawari-8. <i>Remote Sensing</i> , 8(11), p.932.
RQ 2	RQ 3	Chapter 3: Inter-comparison of Himwari-8 AHI-FSA with MODIS and VIIRS active fire products. Wickramasinghe, C., Wallace, L., Reinke, K. and Jones, S., 2018. Inter-comparison of Himawari-8 AHI-FSA with MODIS and VIIRS active fire products. <i>International Journal of Digital Earth</i> , pp.1-17.
		Chapter 4: Multi-level wildfire surveillance using geostationary satellites. Wickramasinghe, C., Wallace, L., Reinke, K. and Jones, S., (in review <i>Remote Sensing</i>)
	RQ 4	Chapter 5: New algorithm implementation resulting in improvements in accuracy and resolution of SEVIRI hotspot products. Wickramasinghe, C., Wallace, L., Reinke, K. and Jones, S., 2018. Implementation of a new algorithm resulting in improvements in accuracy and resolution of SEVIRI hotspot products. <i>Remote Sensing Letters</i> , 9(9), pp.877-885.
		Chapter 6: Conclusion

FIGURE 1.1: Structure of thesis, research objectives and publications.

Figure 1.1 illustrates the how each chapter addresses the research question. Chapter 2 details the development of the AHI-FSA algorithm and testing the algorithm in case study fires. Chapter 3 investigates the different techniques that can be used for intercomparison of geostationary wildfire surveillance products. Chapter 4 conducts a detail intercomparison of

AHI-FSA over Australia. Chapter 5 investigates the application of the algorithm in other geostationary weather satellites. The conclusion and synthesis chapter (chapter 6) details, how the thesis objectives are addressed through the work and provides current limitations of the developed algorithm and further actions.

2

Development of a Multi-Spatial Resolution Approach to the Surveillance of Active Fire Lines Using Himawari-8

This chapter is based on: *Wickramasinghe, C.H., Jones, S., Reinke, K. and Wallace, L., 2016. Development of a multi-spatial resolution approach to the surveillance of active fire lines using Himawari-8. Remote Sensing, 8(11), p.932.*

Abstract

Satellite remote sensing is regularly used for wildfire detection, fire severity mapping and burnt area mapping. Applications in the surveillance of wildfire using geostationary-based sensors have been limited by low spatial resolutions. With the launch in 2015 of the AHI (Advanced Himawari Imager) sensor on board Himawari-8, ten-minute interval imagery is available covering an entire earth hemisphere across East Asia and Australasia. Existing active fire detection algorithms depend on middle infrared (MIR) and thermal infrared (TIR) channels to detect fire. Even though sub-pixel fire detection algorithms can detect much smaller fires, the location of the fire within the AHI 2×2 km (400 ha) MIR/TIR pixel is unknown. This limits the application of AHI as a wildfire surveillance and tracking sensor. A new multi-spatial resolution approach is presented in this paper that utilizes the available medium resolution channels in AHI. The proposed algorithm is able to map fire-lines at a 500 m resolution. This is achieved using near infrared (NIR) (1 km) and RED (500 m) data to detect burnt area and smoke within the flagged MIR (2 km) pixel. Initial results based on three case studies carried out in Western Australia shows that the algorithm was able to continuously track fires during the day at 500 m resolution. The results also demonstrate the utility for wildfire management activities.

2.1 Introduction

Wildfire is an important environmental driver influencing ecosystem processes including the regeneration and diversification of plants and habitat. However, wildfires near semi-urban areas pose a significant risk to both life and property. Effective wildfire management and early warning systems are of key importance in saving lives and property. Wildfires are highly unpredictable making them difficult to predict and control. Firefighters depend on fire behaviour information to plan and carry out control measures. For example, fire front velocity is key when planning firebreaks, which typically involves clearing strips of vegetation in front of the fire to prevent the fire spreading. Fire surveillance data can provide the necessary information such as fire front speed and direction.

Several techniques are routinely used for wildfire surveillance such as ground sensor networks, aerial line-scans and satellite remote sensing (Mengod, 2015; San-Miguel-Ayanz et al., 2005). Ground based sensors are often deployed in small-localized high-risk areas, but are costly to install and maintain. Aerial imagery provides more flexibility in terms of coverage, with a high initial investment. Satellite based remote sensing provides an ideal platform for wildfire surveillance in terms of both cost and coverage. Satellite based sensors can provide large area coverage, capturing a complete and comprehensive view of the fire. Depending on the sensor platform, observations range from once or twice daily observations to every 10 min. Moderate Resolution Imaging Spectroradiometer (MODIS) and Visible Infrared Imaging Radiometer Suite (VIIRS) are two widely used fire detection sensors. These polar orbiting sensors provide 1 km and 375 m spatial resolution

detection capabilities, respectively, with four time daily and two time daily observations (Giglio et al., 2003; Justice et al., 2002a; Morgan et al., 2001; Roberts & Wooster, 2008a; Laneve et al., 2006; Schroeder et al., 2014). Geo-stationary sensors, on the other hand, can provide observations every 10-30 min, making them ideal for near real-time fire surveillance. The main drawback of these sensors is that they are designed as weather satellites with coarse spatial resolutions of around 2-4 km².

Himawari-8 is a relatively new geo-stationary weather satellite launched in October 2015 by Japan Meteorological Agency (JMA). On board is the Advanced Himawari Imager (AHI) (Mitsubishi Electric for JMA, Japan) 16 channel multi-spectral sensor with a 500 m RED channel, 1 km GREEN, BLUE and NIR (Near Infrared) channels. The remaining 12 channels are in the MIR (Middle Infrared) and TIR (Thermal infrared) region ranging from 1.6- 13.3 μm with a 2 km spatial resolution. In terms of coverage, AHI currently captures an entire hemisphere every 10 min covering the East Asia region (Da, 2015). This paper investigates the use of the AHI sensor for near real-time wildfire surveillance. A new algorithm, AHI Fire Surveillance Algorithm (AHI-FSA), is proposed to map fire-lines at 500 m spatial resolutions every 10 min. The algorithm is based on utilizing three different spatial resolutions provided by the MIR, NIR and RED channels. Initial case studies of three fires shows the algorithm can effectively and accurately track the fire-line at 500 m resolution, demonstrating the viable applications of AHI-FSA algorithm for near-real time wildfire surveillance. The algorithm also shows potential for detecting small, low intensity fire compared to existing MODIS thermal anomalies data products.

2.1.1 Remote Sensing Fire Detection

The concept of assessment of fire at sub-pixel level for sensors with more than one channel in the thermal infrared region was originally introduced by (Dozier, 1981). This bi-spectral method is based on the idea that *If one part of a pixel is much warmer than the remainder, for example, that warm part will contribute proportionally more radiance to the signal in shorter wavelengths in the thermal Infrared than in longer wavelengths* (Dozier, 1981). Taking forward the bi-spectral sub-pixel assessment technique Kaufman et al. (1998) introduced a contextual threshold based detection algorithm, which is currently used in the MODIS active fire algorithm (Giglio et al., 2003). Contextual thresholds enable the algorithm to more effectively distinguish thermal variation due to fire from the background pixels that are non-fire or smoldering (Justice et al., 2002a; Morgan et al., 2001; Roberts & Wooster, 2008a). The Current MODIS active fire algorithm version 4 is the latest version of the initial algorithm with improvements made to detect smaller fires and reduce false detection (Giglio et al., 2008a) .

The Automated Biomass Burning Algorithm (ABBA) is another algorithm derived from the same bi-spectral, sub-pixel detection technique. This algorithm was primarily developed for Geostationary Environmental Operational Satellite (GEOS) sensors (Prins et al., 1998). The algorithm uses visible channels to correct for surface albedo value, which aids in reducing the effects of solar contamination in the thermal

channels. It has been demonstrated that the GEOS sensor with 4 km thermal channels can detect fires as small as 0.5 ha at 759 K (Kelvin) near the equator using ABBA algorithm (Prins et al., 1998). Several authors (Prins et al., 1998; Koltunov et al., 2012; Prins et al., 2001) have further demonstrated the use of ABBA with the Spinning Enhanced Visible and Infrared Imager (SEVIRI) on board European Meteosat Second Generation (MSG) with 3 km thermal channels. Showing the possibility to detect fires as small as 0.2 ha at 750 K near the equator using ABBA. Even though the discussed techniques have improved sub-pixel level fire detection, the reliability of the minimum fire size and intensity limits the use of geostationary sensor for fire monitoring (Laneve et al., 2006).

Based on the literature, it is assumed that by using existing sub-pixel thermal detection algorithms with the AHI sensor, fires as small as 0.5–0.2 ha could potentially be detected. Even though it is possible to detect much smaller fires at the sub-pixel level, the detection result can only point to the area of a 2×2 km pixel (400 ha), which is not ideal for active fire surveillance operations. To effectively utilize the sensor for wildfire surveillance, it is vital that the location of the actual fire within the 2 km thermal channel be mapped at higher resolution. Thus, the new algorithm, AHI-FSA, introduced in this paper adopts a multi-spatial resolution approach to map the fire-line at 500 m resolution. This is achieved via the 1 km NIR channels to detect burnt and un-burnt vegetation and the 500 m RED channel to detect the edge between smoke and non-smoke areas.

2.2 Algorithm Development

The AHI-FSA algorithm takes advantage of the multi-spatial resolution data available via the AHI to map a burning fire-line at a 500 m resolution every 10 min. A condition of the algorithm is that wind is present throughout the duration of the fire. This implies that the fire-line is also moving in the direction of the wind, thus, there is minimal or no smoke over the burnt area and dense smoke can be observed at the leading edge of the fire due to smoldering and burning. The algorithm also requires cloud free imagery, and dependence on the NIR and RED channels thus limiting the algorithm to daytime surveillance only.

The algorithm is implemented using a four-step process. The first step is for the algorithm to reference the MIR channel to detect thermal anomalies at a sub-pixel level. A contextual filter is applied to MIR radiance difference between fire and non-fire imagery to identify anomalous pixels, and this is discussed in more detail in Section 2.2.3. This will bound the fire to within a 2×2 km (400 ha) area. The second step utilises the NIR channel to distinguish between the burnt/partially-burnt and unburnt vegetation within the detected MIR pixel, improving the resolution to 1 km^2 . Once burning and partially burning areas have been identified, the RED channel is used in the third step to detect the edge between high smoke density and non-smoking pixels. The final step is to flag the edge pixels as non fire pixels, possible active fire-line pixels and fire-line pixels. This improves the spatial resolution of active fire mapping from 400 ha to 25 ha. Figure 2.1 shows a flow diagram of the algorithm and Table 2.1 summarises the AHI channels used. The

TABLE 2.1: AHI channels used in the AHI-FSA algorithm and application.

Channel	Wavelength (μm)	Resolution (Km)	Purpose
MIR	3.8853	2	Thermal differences
NIR	0.85670	1	Vegetation cover changes
RED	0.63914	0.5	Smoke density

algorithm is discussed in more detail in the following sections of this paper. In Section 2.2.1, the daily behaviour of the radiance/reflectance in MIR, NIR and RED channels is presented. In Section 2.2.2, input data for the algorithm are discussed. Sections 2.2.3, 2.2.4 and 2.2.5 describe the threshold conditions used in the algorithm.

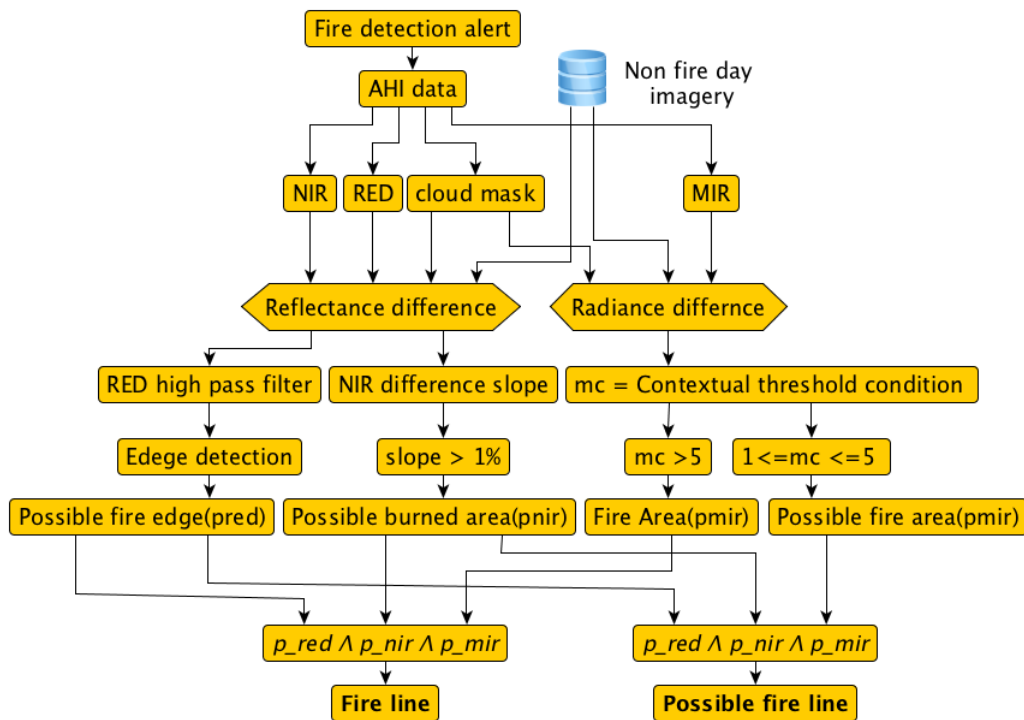


FIGURE 2.1: AHI-FSA algorithm flow diagram.

AHI:Advance Himawari Imager,AHI-FSA:AHI-Fire Surveillance Algorithm, MIR:Middle Infrared, NIR:Near Infrared

2.2.1 AHI Data

It is important to understand the diurnal cycle of land surface temperature observed by the AHI MIR channel to eliminate false detection of thermal anomalies. During a typical day, the earth's surface temperature rises reaching a maximum around mid-day, before falling in the afternoon. Monitoring MIR radiance observations demonstrates this behavior. This is also true for NIR and RED channels, where increasing and decreasing illumination conditions during the day result in variation in the reflectance observed by the sensor. Variations between observations taken at the same time in two consecutive days may also be observed due to changes in atmospheric conditions. Much larger variation can be observed when looking at monthly/annual variations in the data. To illustrate this, Table 2.2 shows the variation in differences in sensor observed MIR radiance and RED and NIR reflectance for five different landcover types urban, vegetation, grassland, bare earth and burnt areas. These values were calculated using data from 5 to 11 September 2015, for case study areas in Western Australia. The reflectance/radiance difference between two days from 9:00 a.m. to 4.00 p.m. (every 10 min) is calculated and averaged based on Equation (2.1) to derive the daily variation, where ρ_r is the daily average in reflectance/radiance between the selected d_i and d_j days, t is the time and n is the number of observations for the particular day. The gap between the two days, d_i and d_j is increased sequentially from one to six days. Land cover based daily averages ρ_r are calculated for one week of data, and weekly average and standard deviation values are calculated as shown in Table 2.2:

$$\rho_r = 1/n \left(\sum_t^{t+1} (d_i - d_j) \right). \quad (2.1)$$

TABLE 2.2: Weekly mean radiance/reflectance differences between two non-fire images for MIR, NIR and RED channels across five generic land-cover types. The maximum difference between two images was six days.

Radiance/Reflectance Differences						
	Mean Value			Standard Deviation		
Land Cover	MIR	NIR	RED	MIR	NIR	RED
Urban	3.524	0.013	0.011	0.021	0.008	0.008
Vegetation	2.899	0.009	0.015	0.027	0.006	0.005
Grassland	3.076	0.007	0.007	0.089	0.006	0.005
Bare earth	4.531	0.009	0.010	0.027	0.006	0.005
Burnt area	10.961	-0.068	-0.017	0.041	0.010	0.007

MIR:Middle Infrared, NIR:Near Infrared, Unit for MIR difference is Watts/(m²*µm).

The results show considerable variation in surface reflectance and radiance within the same land cover, due to the daily variation in surface temperature and reflectance during the day. However, variation between land cover classes were small except when comparing burnt area to all other land covers. Thus, for the area under investigation, when determining reflectance/radiance differences, there appears to be little influence due to land cover. As shown in Table 2.2, the maximum NIR reflectance difference between two land cover classes was 0.013 between urban and grass land (where burnt area is ignored), which is below the value for normal daily variation within a land cover type. Large drops in NIR and RED reflectance are observed due to removal/modification of the top vegetation layer in the burnt area. An increase in the difference of MIR radiance is observed, and this could be due smouldering or blackish surface heating up unevenly during the day.

2.2.2 Data Preparation

The input data for the algorithm include radiance/reflectance difference images computed using fire and non-fire day imagery with the same time stamp. To remove the impact of cloud cover, the non-fire day image is derived as an eight-day composite image. Existing cloud free procedures, such as the MODIS eight-day composite, have been shown to produce cloud free images using less than eight days of observation (Roy et al., 2006). When available, Himawari-8 cloud mask data products may be used to remove clouds from the fire day image (Imai & Yoshida, 2016). However, the current implementation of the algorithm requires the manual identification of cloud due to inaccuracy of the Himawari-8 cloud mask product as observed during the case study. The algorithm limits non-fire day imagery to be not earlier than eight days before the fire. This time constraint on the non-fire day imagery is to avoid the influence of seasonal changes that may affect the threshold conditions in the algorithm. For example, MIR radiance will be lower in winter compared to summer.

2.2.3 MIR Condition

The MIR $3\mu\text{m}$ channel is close to the spectral maximum for radiative emissions observed for objects radiating at temperatures found in fires, and in regions of low solar and terrestrial radiation (Robinson, 1991; Wooster et al., 2003). Wooster et al. (2003) demonstrated that MIR can be used to estimate the entire radiant energy from fire, while Calle et al. (2005) showed that a multi-temporal fire radiant energy calculation based on MIR radiance can be used to detect fires at sub-pixel level. Based on the above, the proposed algorithm depends only on the MIR channel to detect thermal anomalies. The proposed algorithm uses the MIR radiance difference image, produced from fire and non-fire day imagery to detect the fire. To increase the chances of detection of a small fire, a contextual threshold approach is adopted. Initially, a 3×3 pixel kernel is used, which is incrementally expanded up to a 15×15 pixel kernel stopping when 65% of pixels are classified as background pixels. Background pixels are then used to calculate the background mean and standard

deviation using the radiance differences image computed from fire and non-fire day images. Once background pixel statistics are computed, Equation (2.2) is applied to derive a contextual-based value (f) for each pixel. Based on this (f) value, the pixels are then classified as non-fire, possible-fire and fire as shown below.

Background Pixel

1. Non-cloud or water pixels plus the eight adjoining pixels (Queen's case).
2. Pixel should also satisfy the non-fire day condition to avoid fire pixels, bare soil and rock surfaces. Non-fire day pixels should be within two standard deviations for the similar region on a non-fire day. This condition is only required for non-fire day images:

$$f_i = \Delta M_i - [\mu_{\Delta M_{bp}} + 0.5 \times \sigma_{\Delta M_{bp}}], \quad (2.2)$$

where ΔM_i is the MIR radiance differences of the target pixel between fire day and non fire day pixels with similar time stamp for the target pixel, $\mu_{\Delta M_{bp}}$ and $\sigma_{\Delta M_{bp}}$ are the mean and standard deviation of the MIR radiance difference of all background pixels in the kernel:

$$\begin{aligned} f_f &= f > 5 : \text{Firepixel}, \\ f_{pf} &= 1 < f \leq 5 : \text{Possiblefirepixel}, \\ f_{nf} &= f \leq 1 : \text{nonfirepixel}. \end{aligned} \quad (2.3)$$

MODIS: moderate-resolution imaging spectroradiometer

2.2.4 NIR Conditions

The NIR is used by the algorithm to look at changes in vegetation cover in order to identify the burning edge at an improved spatial resolution of 1 km. There are a number of techniques that have been developed to identify changes in vegetation from remotely sensed imagery (Hayes & Sader, 2001; Lyon et al., 1998; Colditz et al., 2015), most of which depend on using vegetation indices such as NDVI (Normalized Difference Vegetation Index). AHI can also be used to calculate NDVI at 1 km by resampling the RED channel to this resolution. However, the proposed algorithm takes an alternative approach and does not use NDVI for vegetation change mapping for two reasons. Firstly, NDVI is sensitive to aerosols mainly due to high sensitivity of RED channel to aerosols (Kaufman & Remer, 1994). Secondly, the algorithm is not looking to quantify the vegetation changes but rather to identify the edge between burning and un-burnt areas. For example grass and forest will have difference NIR reflectance values and the drop in NIR due to fire in grass land and forest will be different. However, prior knowledge of the underlying landcover is not necessary as the NIR condition is only looking at sudden drop in NIR value.

The NIR channel has a relatively higher reflectance over vegetation in comparison to the Red, Green and Blue channels. This suggests that a greater reduction in reflectance will be observed as a result of the

burning of vegetation. The NIR channel is the least influenced by smoke out of the four channels (Kaufman et al., 1997). The algorithm calculates the gradient of change (expressed as a percentage) (Longley et al., 2005) using the reflectance difference image from fire and non-fire day. By calculating the slope, changes in the neighbouring pixels are also taken into account. High slope value means a higher drop in NIR compared to neighbouring pixels. The importance of calculating slope is that there is a positive and negative slope. A positive slope can be caused by smoke and a negative slope can only happen when vegetation cover is removed, in this case due to fire. Based on the three case studies, we have identified a slope value of -1% or lower as the threshold condition to flag NIR pixels as burning/burnt pixels. This slope value is subject to change based on landcover type

$$S_n = slope(\Delta N_i) = < -1, \% \quad (2.4)$$

where (ΔN_i) is difference NIR reflectance between fire and non-fire day imagery.

2.2.5 RED Conditions

In this step, the algorithm takes advantage of the RED channel to detect the edge of smoke affected areas within burning NIR pixels flagged using the NIR threshold condition. The RED channel is chosen because of its enhanced spatial (500 m) resolution and sensitivity to smoke. The RED channel typically shows higher reflectance over smoke (Kaufman et al., 1997). To further increase the detection of reflectance differences, a 3×3 high pass filter is applied to the RED reflectance difference (ΔR_i) image. When considering only a fire event, observed RED reflectance will change due to smoke in the pixels or when the pixel is burnt or burning. It is easier to identify the boundary of these changes using an edge detection technique compared to using a threshold value to identify the edge of smoking pixels. These boundaries or edges can fall into one of three types: (a) smoke/burnt; (b) smoke/unburnt; and (c) burnt/unburnt. The results for all three types of edges are carried over to the final fire-line classification stage, where (c) will be eliminated using MIR flagged fire pixels and (b) will be eliminated using NIR and MIR flagged pixels:

$$\begin{aligned} \Delta R_{hp} &= high_pass_filter(\Delta R_i), \\ R_{edge} &= edge(\Delta R_{hp}). \end{aligned} \quad (2.5)$$

2.2.6 Fire-line and Hotspot Classification

The fire-line pixels (that is, pixels identified as fire boundaries) are identified by eliminating (b) and (c) type edges detected in the RED condition. Simple intersection is applied as shown in Equation (2.6) to eliminate (b) and (c) edges; only flagged RED pixels that fall inside a flagged MIR and flagged NIR pixels will be identified as a fire-line pixel, which leaves only the ‘smoke-burnt’ edges that can satisfy all three conditions.

Based on the two confidence levels in MIR pixel, final fire-line are classified as either ‘fire-line’ or ‘possible fire-line’:

$$\begin{aligned} f_m \cap f_n \cap R_{edge} &: \text{Fire - linehotspots,} \\ f_{pm} \cap f_n \cap R_{edge} &: \text{Possible fire - linehotspots.} \end{aligned} \quad (2.6)$$

2.3 Case Study Method

2.3.1 Case Study Fires

Three fires were chosen for preliminary evaluation of the AHI-FSA algorithm. These fires were near Camballin, Fitzroy Crossing and Broome in West Australia (2.2) occurring on 9 to 14, 9 to 17 and 7 to 11 September 2015, respectively. The case study area shown in 2.2, is mostly covered with sparse hummock grasses and saltbush. A single fire day was chosen for detailed investigation. The study fire day was picked as 10 September to avoid cloud throughout the day. Non-fire, cloud-free images were generated by creating a composite image for every 10 min time stamp using imagery from 1 to 8 September 2015. The AHI-FSA was run from 01:00 to 06:30 UTC (Universal Time Coordinated), which also covers the two MODIS day time passes over the fires.

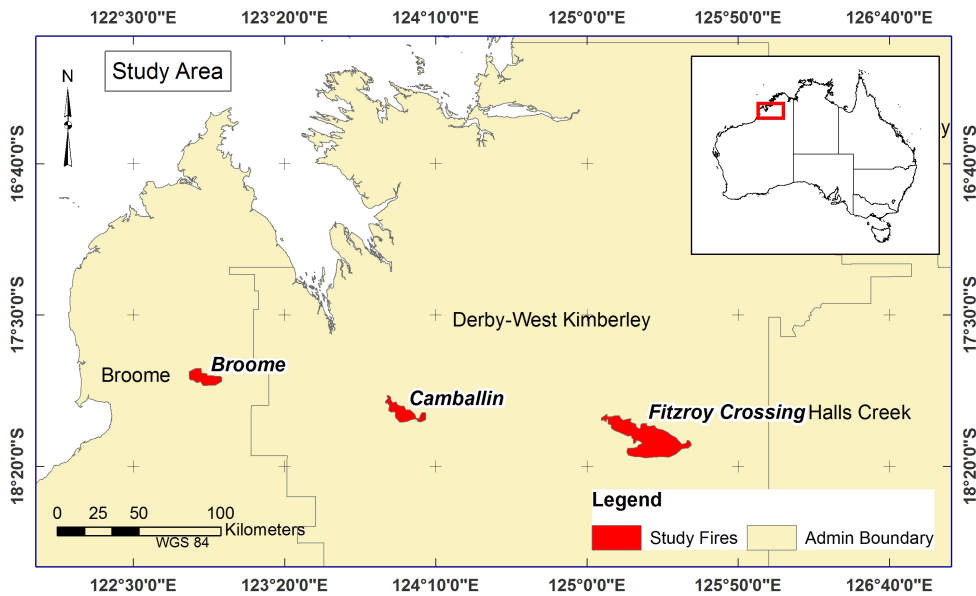


FIGURE 2.2: Study area map.

2.3.2 Cross-Comparison Evaluation Method

The AHI-FSA algorithm results are compared with MODIS active fire products, which provides thermal anomalies at 1 km ground resolution. MODIS sensor on board Terra and Aqua provides twice daily observations four hours apart. In this case, Terra observes at 01:40 UTC and Aqua at 06:00 UTC. MODIS active fire products provide the location of thermal anomalies typically associated with fires, including burning and smouldering/cooling-down areas. AHI-FSA fire-line pixels, on the other hand, maps the burning edge of the fire. Thus, a direct comparison of the two different products is not possible. However, a visual inspection can be carried out by comparing the location of the fire-line hotspots from the algorithm and the MODIS thermal anomalies.

Comparison to the burnt area from 01:40 to 06:00 UTC (260 min) allows errors of commission to be determined. In this case, we considered any fire-line pixels in the entire period, which occurred within the burnt area boundary to be true detections, and those outside of the boundary to be errors of commission. Errors of omission could not be determined using this method as the burnt area includes the area burnt outside of the case study time period. The burnt area was digitized, via visual inspection of changes in MODIS 7-2-1 false colour images from Terra and Aqua. AHI-FSA fire-line hotspots results from 01:40–06:00 UTC were stacked to create a composite AHI-FSA fire-line detection. Visual inspection was also carried out based on Landsat-8 post fire image. Landsat-8 imagery was not used to calculate the commission error as Landsat image was observed eight days after the fire day.

2.4 Results

Time sequences of fire-line hotspots derived from the algorithm for the Camballin fire on the 10 September 2015 is shown in Figure 2.3. The sequential progression of the fire is clearly visible from the algorithm results. From the sequence of images, it is clearly visible that the main fire front is progressing in a north-westerly direction, with a smaller fire to the east progressing in an easterly direction. At 01:40 UTC, the MODIS data shows a single fire, however, at 06:00 UTC, and two fire fronts are visible in the MODIS product. This strongly supports the algorithm results during the MODIS observation gap to be accurate. Similar findings can be shown for other case study fires. Two separate fires at Fitzroy Crossing and Broome on the same day are shown in Figure 2.4. Both show early detection and fire progression by the AHI-FSA algorithm. In particular, Figure 2.4 image (c-1) shows that the Broome fire was detected only by the AHI-FSA at 01:40 UTC. Visual inspection with the background Landsat-8 post fire image shows most of the detected pixels fall within the actual burnt area. This indicates that the agreement between AHI-FSA fire-lines and final burnt area. In comparison with MODIS data on Figure 2.4, images (a-1) and (a-2), it is clear that around 01:40 UTC, the fire was moving in a south-westerly direction but had changed direction by almost 90 degrees by 06:00 UTC. The algorithm was able to show the fire-line in the northern section of the fire beginning to burn with the changing wind direction, taking the fire in a north westerly direction. Demonstrating the importance of the high temporal information that is provided through the algorithm. Results of the cross-comparison

evaluation are reported in Table 2.3. Overall, the algorithm showed less than 20 % commission error for the three case study fires.

TABLE 2.3: Total burnt area during the 10 September 2015 case study fires, mapped using MODIS Terra and Aqua 7-2-1 channel false colour imagery. The AHI-FSA detections from 01:40 to 06:00 UTC are combined to calculate the total area detected by AHI-FSA as in Figure 2.4 images a-3, b-3 and c-3. Commission error values are calculated based on the area detected using the AHI-FSA outside of the burnt area.

	Digitized Burnt Area (km ²)	Total Area Detected (km ²)	Area Detected within Burnt Area (km²)	Commission Error (%)
Fitzroy Crossing	426.4	185.2	153.8	16.9
Camballin	97.1	49.2	37.6	23.6
Broome	60.6	43.2	32.45	24.8
Total	594.1	277.6	223.9	19.3

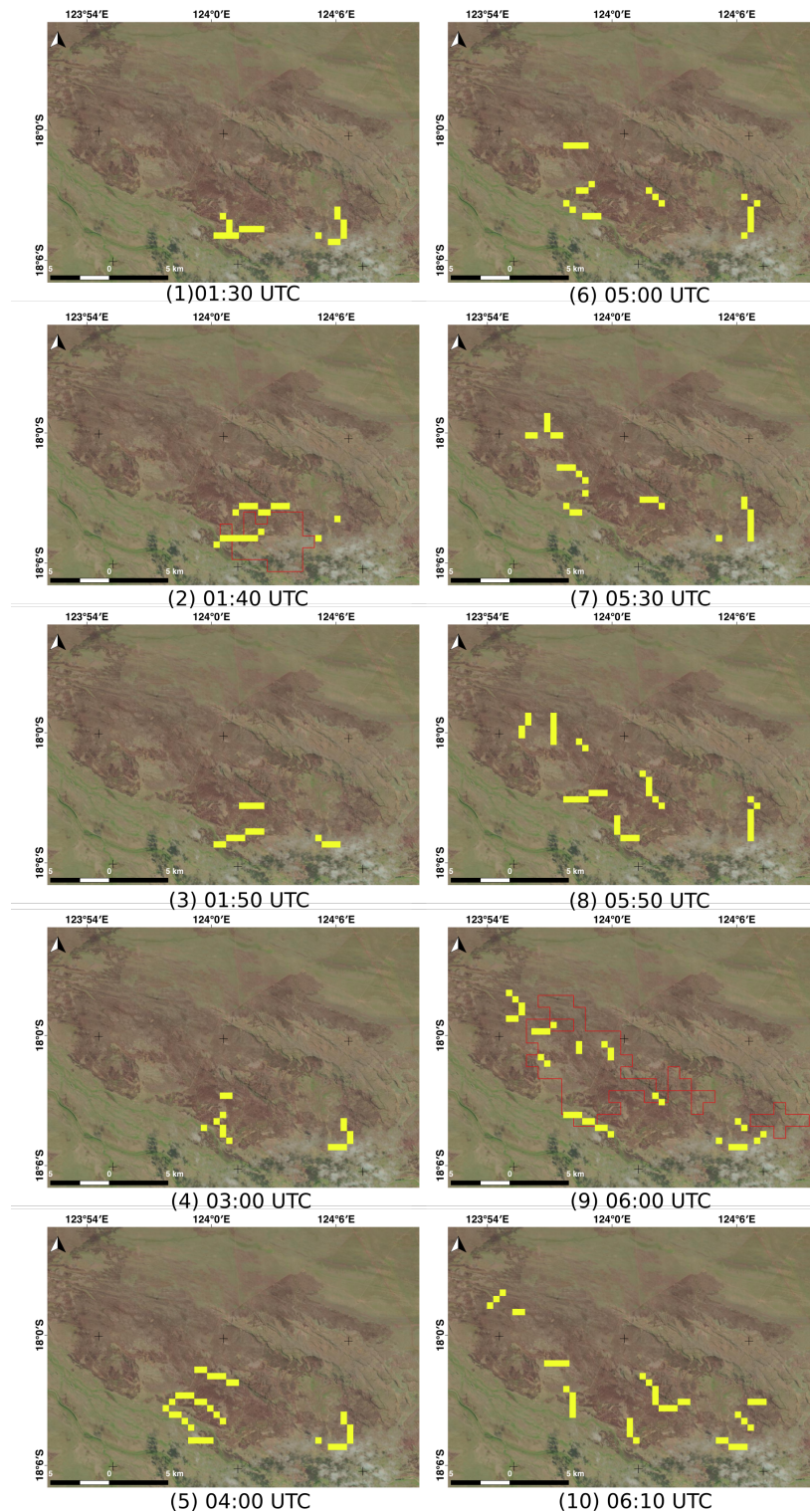


FIGURE 2.3: Compares the algorithm results with MODIS thermal anomalies hotspot products for Camballin fire on 10 September 2015. The sequence of images are from 01:30 UTC ten minutes before Terra a.m. (01:40 UTC) observation, followed by 01:40 UTC, and there after 03:00, 04:00, 05:00, 05:30 and again ten minutes before Aqua a.m. observation (05:50), followed by 06:00 and finally at 06:10 UTC. MODIS thermal anomaly product, which are at 1 km spatial resolution, are overlaid as pixel boundary in **red**. Algorithm results are overlaid in **yellow** which includes 'fire-line' as well as 'possible fire-line' pixels. The background image is a Landsat-8 post fire image acquired on 24 September.

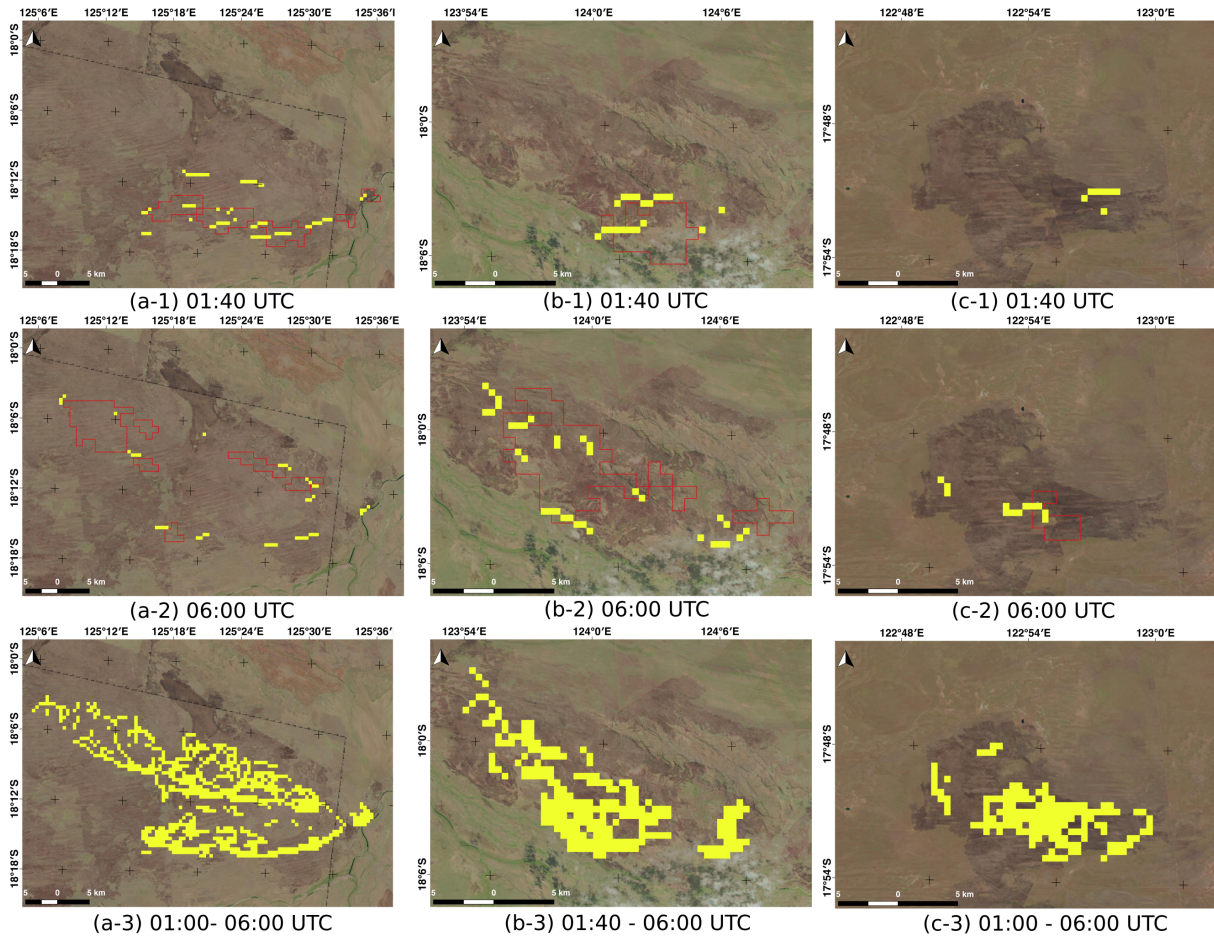


FIGURE 2.4: Three fires in Western Australia on the 10 September 2015, the Fitzroy Crossing fire (on the left (a)), the Camballin fire (on the middle (b)) and the Broome fire (on the right (c)). The first two rows of images (1,2) shows fire detection at 01:40 and 06:00 UTC, respectively, from the algorithm (yellow) and MODIS thermal anomaly hotspots (red pixel boundary) with the Landsat-8 post fire image as the background; the last row (3) is a composite of all detected pixels from the algorithm 01:40 to 06:00 UTC, between MODIS Terra and Aqua observations.

2.5 Discussion

Wildfire surveillance is an important aspect of fire management, as such near real-time satellite monitoring systems will provide great benefits to fire agencies for wildfire management and response. The current MODIS thermal anomalies product provides a very low temporal resolution in terms of wildfire monitoring. In contrast, Himawari-8 AHI provides high temporal resolution (10 min) imagery, making it ideal for wildfire surveillance. Additionally, 2 km spatial resolution in the MIR and TIR channels limits the use of existing fire detection algorithms, such as the MODIS active fire algorithm and WF-ABBA (Wildfire Automated Biomass Burning Algorithm), due to coarse resolution in these channels. In terms of wildfire monitoring applications,

a 2 km resolution will not be sufficient to map the spatial detail of the fire, thus limiting the usability of AHI as a wildfire surveillance sensor. To address this challenge, the new AHI-FSA adopted the 1 km NIR and 500 m RED channel to improve the detection of fire-line to 500 m. AHI-FSA tracks the boundary of the burning fire-line at the time of observation. Thus, at a single time stamp, the algorithm captures only the edge fire pixels that fall in the direction of the spreading fire. The frequent mapping of fire edge detections can provide useful information relating to the behaviour of the fire, such as the speed and direction of travel at temporal and spatial resolution that improves upon current satellite based systems.

The validation method adopted herein provides cross validation with MODIS active fire products. AHI-FSA fire-line detections and MODIS active fire products are compared at similar time stamps and over all performances of the algorithm during four hours of observation is also validated. Initial results suggest AHI-FSA is able to track wildfire at 500 m resolution. The algorithm is shown to continuously track the case study fires, which occurred in scrub/grass land cover. In the study, AHI-FSA was also able to detect sudden changes in the fire with changing weather conditions, as shown in the Fitzroy Crossing fire. AHI-FSA detected a small fire-line to the north of the MODIS hotspot at 01:40 UTC (Figure 2.4 image (a-1)) and tracked the gradual progression of the fire in the north-west direction; this was confirmed by the 06:00 UTC hot spots detected by MODIS Aqua observation. During the case studies, AHI-FSA was able to track the fire with less than 20% commission error, sufficient for fire surveillance activities. Results also demonstrate the effectiveness of the MIR threshold condition to identify thermal variation comparable to MODIS even though MODIS MIR pixels are four times smaller than the AHI pixels. For example, Figure 2.4 (c-1) shows only AHI-FSA detected the fire at 01:40, which is later confirmed by the MODIS Aqua hotspots. This could be due to the fact that the AHI-FSA is looking at radiance difference between fire and non-fire day images, compared to MODIS active fire products using only the fire day image. Further studies are needed to identify the minimum changes in fire temperature that could be detected by the MIR contextual threshold method presented in this paper.

The RED channel based edge detection also showed to be effective in mapping the edge between the smoking and burnt area. However, the dependence on wind to blow the smoke away from the burnt area means that low wind condition could affect the performance of the algorithm. The algorithm could also be affected by the burning material itself. For example, forests with thick undergrowth and dense canopies that can burn and smoulder continuously for a considerable length of time, thereby producing smoke long after the actual fire front has passed through, which could effect the edge detection. Thus, further studies must be carried out to test the performance of the algorithm in such different conditions.

To our knowledge, this is the first time three channels MIR, NIR and RED have been used in a fire surveillance algorithm. The algorithm has the potential to be used with other high temporal sensors such as Geostationary Operational Environmental Satellite (GOES) with 1 km visible bands and 4 km thermal bands. Furthermore, the algorithm can easily be adopted to pick up continuously smouldering pixels by tracking non-moving pixels. Fire duration data can also be used in fire severity mapping, where fire intensity as well

as duration is of importance.

2.6 Conclusions

This paper proposes a new algorithm that takes advantage of high temporal imagery provided by AHI for near real-time fire surveillance. The AHI-FSA algorithm overcomes the limitations of coarse resolution thermal channels in AHI by adopting a multi-spatial resolution approach. The AHI-FSA performed well in the Western Australian case study fires. Results showed the fire-line continuously tracked at a 500 m resolution for the duration of the study period for all three case study fires, filling in the gap between MODIS Terra and MODIS Aqua observations and showing the progression of the fire quite accurately. Over 80% accurate detection was achieved in the case study application, indicating that the multi-resolution approach has been effective in bringing the initial 2×2 km detection in thermal band to 500 m. Due to the high temporal resolution, it is possible to improve the timeliness and spatial accuracy of fire behavioural data, such as speed and direction of the fire, every 10 min. Initial validation shows that the algorithm can perform well in tracking fire using the multi resolution approach. However, further detailed validation must be carried out comparing with more MODIS active fire products and other remote sensing sensors such as Visible Infrared Imaging Radiometer Suite (VIIRS) hotspots. Tests must also be carried out to identify AHI MIR and RED channel sensitivity to thermal anomalies and smoke, respectively. AHI-FSA must also be validated in different land-cover conditions. Further development in terms of the algorithm would be to add temporal contextual awareness to the algorithm such as the state of the pixel in the previous time stamp. This would enable the algorithm to track status of the pixels such as non-fire, fire, and burnt area, and could reduce the false detection in the already burnt area.

3

Intercomparison of Himawari-8 AHI-FSA with MODIS and VIIRS active fire products

This chapter is based on: *Wickramasinghe, C., Wallace, L., Reinke, K. and Jones, S., 2018. Intercomparison of Himawari-8 AHI-FSA with MODIS and VIIRS active fire products. International Journal of Digital Earth, pp.1-17.*

Abstract

The AHI-FSA (Advanced Himawari Imager - Fire Surveillance Algorithm) is a recently developed algorithm designed to support wildfire surveillance and mapping using the geostationary Himawari-8 satellite. At present, the AHI-FSA algorithm has only been tested on a number of case study fires in Western Australia. Initial results demonstrate a high potential as a wildfire surveillance algorithm providing high frequency (every 10 minutes) fire-line detections. This paper intercompares AHI-FSA in the Northern Territory of Australia (1.4 million km²) over a 10 day period by comparing AHI-FSA to the well-established fire products from LEO (Low Earth Orbiting) satellites such as MODIS (Moderate Resolution Imaging Spectroradiometer) and VIIRS (Visible Infrared Imaging Radiometer Suite). This paper also discusses the difficulties in comparing high temporal frequency fire products with existing low temporal resolution LEO satellite products. The results indicate that the multi-resolution approach developed for AHI-FSA is successful in mapping fire activity at 500 m. When compared to the MODIS, thermal anomaly products and considering the increased temporal resolution of AHI, AHI-FSA omission error was only 7%. High temporal frequency data also results in AHI-FSA observing fires, at times, three hours before the MODIS overpass with much-enhanced detail on fire movement.

3.1 Introduction

Wildfire response management requires near real time information on fire behaviour such as fire intensity, speed and direction. In Australia, in addition to satellite data, fire behaviour information is sourced mainly from ground observations and aerial surveillance, and often limited to only high risk fires. Geostationary Earth observation satellites can provide the temporal resolution and coverage necessary for fire surveillance over a large area (Xu et al., 2017; Schroeder et al., 2008a). Such systems have high utility for a large country such as Australia, to map and monitor wildfires in remote regions. Currently, thermal anomaly products from Low Earth Orbiting (LEO) MODIS (Moderate Resolution Imaging Spectroradiometer) and VIIRS (Visible Infrared Imaging Radiometer Suite) sensors are used operationally to track fires. These satellites can provide up to six observations per day depending on the latitude. The AHI-FSA is a new fire surveillance algorithm developed to provide wildfire surveillance using the Himawari-8 satellite (Wickramasinghe et al., 2016). The AHI (Advanced Himawari Imager) sensor onboard the Himawari-8 geostationary satellite can provide observations every 10 minutes. Case studies carried out on single fires have shown the potential of the AHI-FSA algorithm to successfully monitor the fire every 10 minutes (Wickramasinghe et al., 2016). However, a detailed study has not been conducted to understand the capabilities of the algorithm, compared to existing Low Earth Orbiting Satellite active fire products. In this paper high temporal AHI-FSA fire products are intercompared with operational products from Low Earth Orbiting Satellites over the tropical savannas of the Northern Territory, Australia (1.4 million km²).

3.1.1 Geostationary Fire Detection Algorithms

In Northern America and Europe, geostationary Earth observation satellites are being used to provide high temporal frequency active fire products. For example, since 2000, WF-ABBA (Wildfire Automated Biomass Burning Algorithm) fire hotspot products have been operational, covering the American continents every 30 minutes (Schroeder et al., 2008a). WF-ABBA is a dynamic multispectral thresholding contextual algorithm that utilises the $3.9\mu\text{m}$ and $10.7\mu\text{m}$ bands onboard the Geostationary Operational Environmental Satellite (GOES). A recent study showed WF-ABBA was able to detect fires larger than 500 ha 80% of the time (Koltunov et al., 2012). However, it failed to detect the majority of short duration fires, as well as fires smaller than 100 ha (Koltunov et al., 2012). In Europe, the Spinning Enhanced Visible and Infrared Imager (SEVIRI) onboard European Meteosat Second Generation (MSG) provides near real time fire monitoring at a 15 minute interval. A MSG-SEVIRI fire detection algorithm was proposed by Calle et al. (2008). These authors demonstrated the use of this geostationary sensor as a highly useful tool in real-time forest fire management and monitoring. These operational examples of high temporal frequency fire detection has led geostationary satellites to be considered an important tool in wildfire management. As such the demand for robust high temporal frequency fire detection algorithms which make use of the opportunities such as the improvement in ground resolution available on new generation of geostationary satellites is high.

3.1.2 AHI-Fire Surveillance Algorithm(AHI-FSA)

Himawari-8 is a weather satellite launched by JAXA in late 2015. AHI (Advanced Himawari Imager) onboard Himawari-8 covers the entire disk area every 10 minutes. It is a 16 band multi-spectral sensor with a 500 m RED ($0.64\mu\text{m}$) band, and 1 km GREEN ($0.51\mu\text{m}$), BLUE ($0.47\mu\text{m}$) and NIR (Near Infrared) ($0.86\mu\text{m}$) bands. The remaining 12 bands are in the MIR (Middle Infrared) ($3.9\mu\text{m}$) and TIR (Thermal infrared) region ranging from $1.6 - 13.3\mu\text{m}$ with a 2 km spatial resolution.

AHI-FSA adopts a multi-temporal and multi-scale approach using $3.9\mu\text{m}$ MIR, NIR and RED bands to provide 500 m nominal resolution fire-line pixel detections. The main goal of the algorithm is to identify the fire activity within the $2\text{ km} \times 2\text{ km}$ MIR pixel that is used to detect thermal anomalies. The multi-scale approach takes advantage of variation in surface reflectance and radiance due to fire. In particular, looking at changes in vegetation cover and smoke activity. AHI-FSA fire-line pixels are generally detected at the trailing edge of the fire (Wickramasinghe et al., 2016). A summary of the AHI-FSA fire-line detection conditions are provided in section 3.1.3; readers are referred to chapter 2 for a complete description of the algorithm.

3.1.3 Algorithm Summary

AHI-FSA applies three independent threshold conditions to MIR, NIR and RED bands to detect fire-line pixels. The three conditions are designed to detect thermal anomalies, changes in vegetation cover due to

fire, and the edge between smoke and non-smoke pixels. If all three conditions are satisfied, a fire-line pixel is detected at a spatial resolution of 500 m. The three threshold conditions depend on the calculated non-fire day and fire day radiance/reflectance difference image as input. A fire day image refers to an image captured on the day of the fire. A non-fire day image is a cloud and fire free image with the same time stamp as the fire day image but captured before the fire. The non-fire image is generated as a composite image using up to 10 days of data going back from the day of the fire. The three threshold conditions are briefly explained below.

- **MIR Condition:** The MIR band is used to detect thermal anomalies using a contextual threshold. Fire day and non-fire day MIR band imagery are taken to calculate the radiance difference. A dynamic contextual threshold is then applied to the MIR difference image to detect thermal anomalies. The detections are classified as a possible fire pixel.
- **NIR Condition:** Change in the NIR band is used to identify changes in vegetation cover. A NIR difference image is calculated using fire day and non-fire day imagery. The rate of change in the difference NIR image is then calculated. Pixels with higher than -1% slope are flagged as a pixel with a rapid negative change in vegetation cover.
- **Red Condition:** In this condition, reflectance difference between a fire day and a non-fire day is calculated for the RED band. A high pass filter is then applied to amplify the variations in reflectance further. Edge detection is then used to determine the boundaries between smoking and burnt/burning area.

3.2 Materials

3.2.1 Study Area

For this comparison exercise, the study area extended across the Northern Territory of Australia between (128.30, 137.00) longitude and (-16.50, -12.30) latitude covering an area of 1.4 Million km². Two study dates were selected around the start of the dry season from 02nd-06th and 25th-29th July 2016 due to high fire activity. This tropical savanna landscape with dense grass, shrubs and scattered trees is affected by a large number of fires during the dry season (Williams et al., 1998, 1999). Figure 3.1 shows the study area demonstrating high fire activity with the fires detected by MODIS hotspots during the study period. The study area has also been used previously for validation of MODIS thermal anomaly, MODIS burn scars and VIIRS active fire products and as such the properties of these data are known (Oliva & Schroeder, 2015; Schroeder et al., 2015; Giglio et al., 2016; Roy et al., 2008).

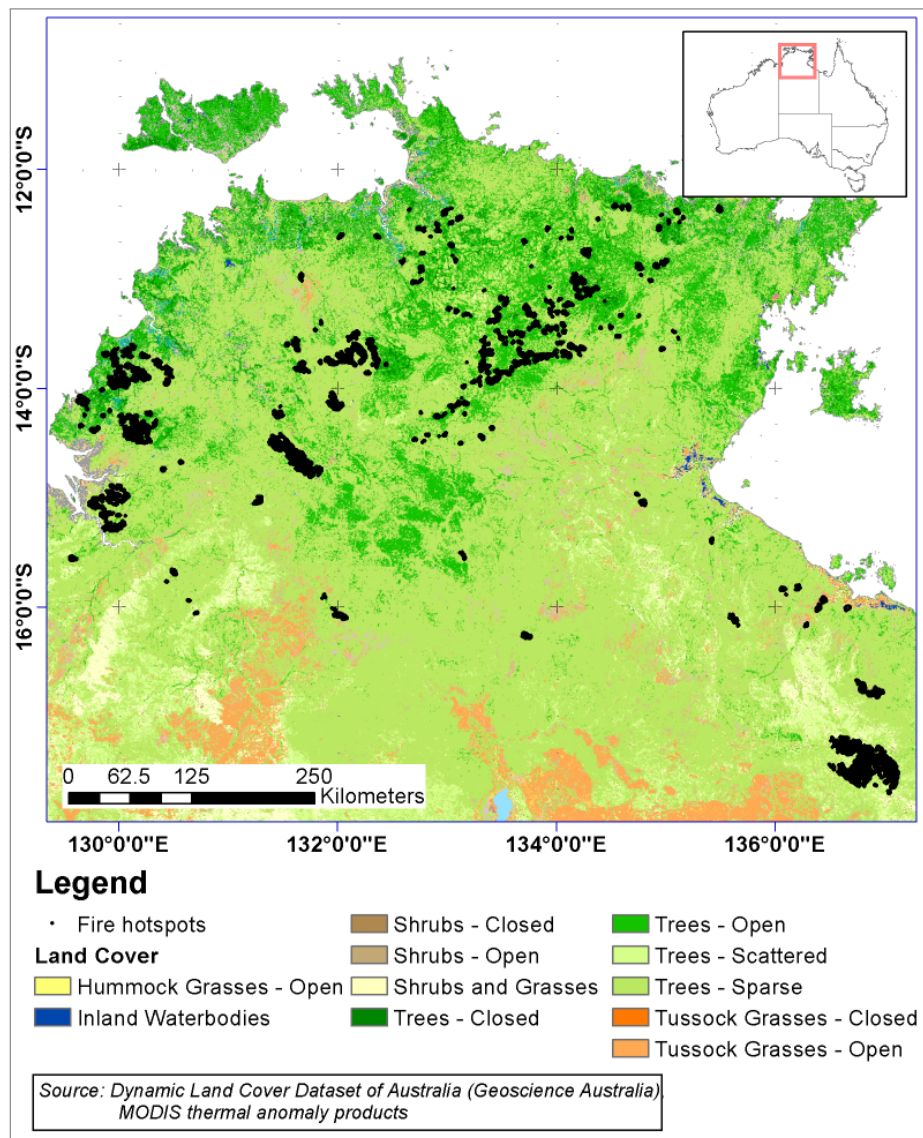


FIGURE 3.1: The study area showing the land cover present and the 880 hotspots (MOD14) detected by MODIS during the study period from 02-06 and 25-29 July 2016.

3.2.2 Comparison Products

The MODIS sensors onboard both Terra and Aqua satellites and the VIIRS sensor onboard Suomi National Polar-Orbiting Partnership satellite each provide day and night-time observations. The fire detection accuracy of the two products are discussed in detail below. Landsat-8 pre and post-fire imagery are used to map the burn area. A summary of spatial and temporal resolution of the image sources used in the study are provided in Table 3.1.

TABLE 3.1: Primary specifications of the comparison datasets used in this study

Products	Spatial Resolution	Temporal Resolution	Time of overpasses used (UTC time)
MODIS hotspots (MOD14,MYD14)	1000 m	3-5 daily	10:30 / 13:30 (02:00/05:00)
VIIRS hotspots	375 m	2 daily	13:30 (05:00)
Landsat-8 burn scars	30 m	every 16 days	10:00 (02:00)

3.2.3 MODIS Thermal Anomaly Products

MODIS provides two observations during the day, and two during the night. The first observation is from MODIS Terra at around 10.30 am local time and the second from MODIS Aqua around 1.30 pm local time. MODIS thermal anomaly products have been evaluated in a large number of studies and have become a standard product for satellite-based fire detection (Giglio et al., 2016). Based on previous studies MODIS, MOD14 and MYD14 products show relatively high commission errors in small forest clearings and omission errors in large fires due to obscuration by thick smoke. Giglio et al. (2016) showed that there is only 26% probability of detecting a fire, with a median fire size of 27 ASTER (Advanced Spaceborne Thermal Emission and Reflection Radiometer) sensor pixels (30 m) in the Australian region. The commission error for the region is around 1% of total detections (Giglio et al., 2016).

For this study, MODIS Thermal Anomalies/Fire products, Collection 6 data, available through the Fire Information for Resource Management System (FIRMS) (available at <https://firms.modaps.eosdis.nasa.gov/>) were used. The data are provided as point data generated by taking the centroid of MODIS MIR band pixel. Point attributes include date/time of observation (UTC), the sensor (Terra or Aqua) and FRP value (Fire Radiant Power). Points observed during overpass times mentioned in Table 3.1 were extracted for the study period. MODIS ground pixel size increases with scan angle as with all earth observation sensors. MODIS cross-track (Δs) and along track (Δt) pixel sizes can be derived from the derived from equations 3.2 and 3.3 (Ichoku & Kaufman, 2005) and pixel diagonal distance can be calculated using equation 3.4.

3.2.4 VIIRS Thermal Anomaly Products

The VIIRS active fire detection algorithm is an implementation of the MODIS thermal anomaly detection algorithm on the VIIRS sensor (Schroeder et al., 2014). A study by Oliva & Schroeder (2015) demonstrated VIIRS was able to detect 100% of the fire in Northern Australia with an area larger than 100 ha. However,

an omission rate of 60% was reported for fires ranging from 10 to 25 ha in size. For this study VIIRS fire hotspots (*VNP14IMGML*) data were used (available from: <ftp://ladsweb.nascom.nasa.gov>).

3.2.5 LANDSAT-8 Burnt Area Data

Landsat-8 is the latest earth observation satellite in the Landsat series. The multi-spectral, Operational Land Imager (OLI) sensor provides 30 m resolution imagery every 16 days. Existing burn scare products, depends on semi-automated change detection techniques to identify sudden changes in landcover, which can introduce errors due to cloud and smoke cover (Goodwin & Collett, 2014), thus manual digitization technique was used to map the burn scars. Further more due to the 16-day revisit period manually identifying the burn area ensured, only burn scars during the study period was mapped.

A total of 36 pre/post images were used in the study as shown in Figure 3.2. Pre and post fire imagery ranged from 2 to 10 days either side of the fire.

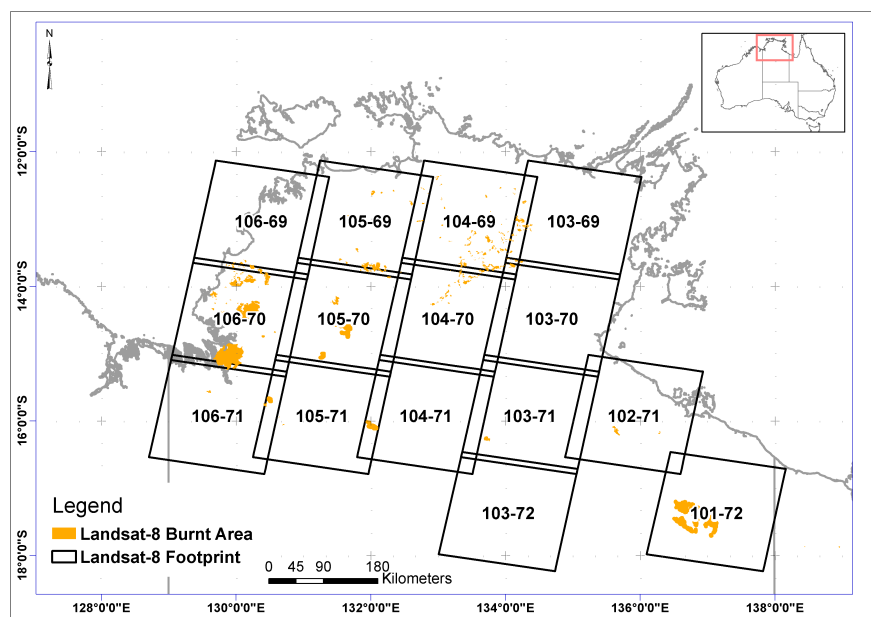


FIGURE 3.2: Landsat-8 scene footprints used for burn area mapping in the study area. Shown in yellow are the digitised burn scars.

3.3 Imagery Navigation and Registration

MODIS Terra and Aqua imagery have a reported geolocation accuracy better than 45 m and 60 m respectively. This is achieved using a global network of ground control points on top of the orbital and attitude data provided by the onboard sensors (Wolfe et al., 2012; Wolfe & Nishihama, 2009). The VIIRS imagery georeferencing algorithm uses a similar technique to MODIS and provides a geolocation accuracy of around

0.25 sensor pixel (0.1 km) (Wolfe et al., 2013; Yu et al., 2016). AHI image navigation and registration is calibrated with orbit and attitude information from star tracker and angular velocity sensors. Pattern matching between the database coastline and that of observation images are also used to improve the image geolocation accuracy (Bessho et al., 2016; Yu et al., 2016). Band to band co-registration is determined via linear pattern matching between different bands. Yu et al. (2016) in their independent assessment of AHI navigation and co-registration, found that mean navigation difference is less than 0.5 AHI pixels (1 km). It was also observed that band to band co-registration in the North-South direction is smaller than in the East-West direction. The mean navigation difference in the North-South direction is $-0.28(\pm 0.20)$ and $-0.35(\pm 0.23)$ AHI pixels at the short and long wavelength bands respectively, compared to RED band. In the East-West direction, the difference values are $0.12(\pm 0.24)$ and $-0.07(\pm 0.34)$ AHI pixels. AHI has the highest positional error of the three sensors, expected to be around 500 m. Positioning shifts in AHI imagery between observations, especially in the RED band, has been observed during the study. Thus to account for any geolocation errors, a 500 m buffer was applied when the commission and omission errors were calculated. This means up to a 500 m shift in AHI-FSA products is accepted when compared with other products. A similar buffering technique to account for navigation errors have been applied when validating the WF-ABBA fire hot-spots (Koltunov et al., 2012). As MODIS and VIIRS point data products were used, the AHI-FSA fire-line pixels were also converted to point data using the centre of the pixel.

AHI-FSA points were then spatially matched to a LEO hotspot, if the distance between the AHI-FSA fire-line pixel and the MODIS hotspot was equal or less than d (equation 3.1). Where d is the maximum diagonal distance between a MODIS/VIIRS pixel and AHI-FSA fire-line pixel center points when the boundaries of the two pixels are overlapping plus a 500 m buffer distance. Any AHI-FSA pixel within this distance was considered as a true detection of the MODIS hotspot.

$$d = (LEO_{dd} + AHIFSA_{dd})/2 + 500 \quad (3.1)$$

Where d is the maximum allowed distance between LEO and AHI-FSA pixel center points, LEO_{dd} is the LEO pixel diagonal distance corrected for scan angle errors and $AHIFSA_{dd}$ is AHI-FSA pixel diagonal distance.

$$\Delta S = R_e s \left(\frac{\cos\theta}{((R_e/r)^2 - \sin^2\theta)^{1/2}} - 1 \right) \quad (3.2)$$

$$\Delta T = r s (\cos\theta - ((R_e/r)^2 - \sin^2\theta)^{1/2}) \quad (3.3)$$

$$d = \sqrt{(\Delta S)^2 + (\Delta T)^2} \quad (3.4)$$

where $R_e = 6378.137 km$ (Earth radius), $r = R_e + h$, $h = 705 km$ (satellite altitude), $s = 0.004184397$, θ is the scan angle and d pixel diagonal distance.

3.4 Comparison Method

The validation of geostationary satellite products is complicated due to the high temporal frequency and lack of equivalent products. As such, the majority of previous attempts to validate such products have done so considering only near-synchronous observations from LEO satellites and ground data (Xu et al., 2017; Roberts & Wooster, 2008b; Koltunov et al., 2012; Schroeder et al., 2008a; Calle et al., 2008). Due to the difficulty in collecting ground truth data over the large study area, this paper looks at intercomparing AHI-FSA results with LEO satellite products. It is common practice to use detection-wise, intercomparison with other satellite products for the omission and commission error assessment of fire products (Feltz et al., 2003; Schroeder et al., 2008a).

The omission and commission errors can be classified into either relative errors or independent errors (Oliva & Schroeder, 2015). Relative errors refer to intercomparison with other products which also contain some level of known error (the LEO hotspot products in this case), whereas independent errors are calculated when the reference data has negligible or no errors. AHI-FSA fire-line pixels are not directly comparable to thermal hotspots products; but are a derived product that depends on vegetation changes and smoke from the fire. As discussed in detail in section 3.4.1. However, in the absence of high temporal comparison products, we are limited to use LEO satellite hotspots and burn scar products. AHI-FSA intercomparison was conducted in three steps. The first step looked at the potential of fire hotspots detections using the AHI-FSA algorithm MIR condition compared to MODIS and VIIRS hotspots. In the second step, the surveillance capabilities of the AHI-FSA was evaluated by comparing the time of a LEO hotspot and the time of its first matching AHI-FSA fire-line pixel. In the final step, the commission and omission error is calculated for the AHI-FSA fire-line pixels as a daily product.

3.4.1 Active Fire-line Pixels and Thermal Anomaly Detections

Fire hotspot products detect high thermal variations on the surface of the earth, and this may include both burning and smouldering pixels. AHI-FSA, on the other hand, produces active fire-line pixels, which are identified as the trailing edge of the fire. Smoke plays a significant part in the AHI-FSA fire-line pixel detection. Smouldering fires with light smoke are less likely to be flagged in the AHI-FSA RED condition, and thus will not be detected by AHI-FSA even if the MIR and NIR conditions are satisfied. This difference between fire hotspots and the fire-line pixels is illustrated in Figure 3.3 (a) where only four of the hotspots detected by MODIS have overlapping AHI-FSA fire-line pixels at the time of observation. Examining the AHI-FSA MIR condition on its own, reveals that all of the MODIS detections are identified. When the AHI-FSA detections from 00:00 UTC to 04:00 UTC are composited together, as shown in Figure 3.3 (b), it is clear that AHI-FSA has detected fire activity within the MODIS hotspot pixels before the MODIS overpass. This is most likely explained by the ephemeral nature of fire and changing conditions through this period. thus time-synchronous intercomparison with LEO hotspots products were compared with thermal anomaly

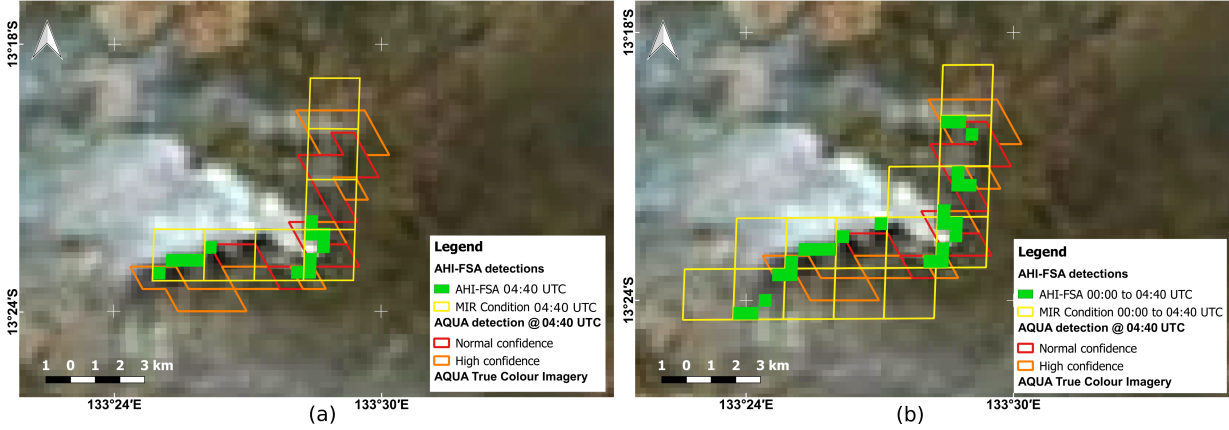


FIGURE 3.3: MODIS and AHI-FSA product detections are compared for a single fire on 6th July 2016. The background image is that observed by the MODIS sensor onboard Aqua at 04:40 UTC. Fire detections from MODIS, AHI-FSA and AHI-FSA MIR condition at 04:40 UTC is shown in image (a). MODIS and AHI-FSA MIR condition detections are shown as pixel boundaries and AHI-FSA detections are shown in green. Figure (b) shows AHI-FSA detections from 00:00 to 04:40 in green illustrating that the AHI-FSA has detected essentially the same fire hotspots as MODIS, but as an earlier observation.

hotspots detections from the AHI-FSA MIR condition to assess detection and surveillance capabilities. Due to a lack of high temporal intercomparable data, AHI-FSA was compared to the closest LEO hotspot based on time and distance.

3.4.2 Intercomparison of Thermal Hotspots

The AHI-FSA MIR condition detects thermal anomaly hotspots using a contextual threshold. To quantify the performance of AHI-FSA MIR condition, MIR condition detections were compared against MOD14, MYD14 and *VNP14IMGML* hotspot products. Spatial resolution of the three products varied from 0.375 km VIIRS, 1 km MODIS and 2 km in AHI-FSA MIR condition. Due to the fact that AHI-FSA MIR has the largest pixel size, the sum of LEO hotspot detections within an overlapping AHI MIR pixel was calculated. A statistical logistic regression model defined in equation 3.5 was then used to determine the performance of the AHI-FSA MIR condition. A similar technique has been used by Schroeder et al. (2008a) and Morisette et al. (2005a) to calculate the performance MODIS and GEOS hotspot products. AHI-FSA MIR condition commission and omission error values were then calculated with respect to MODIS and VIIRS using 2 km × 2 km grids.

$$P(x_i) = \frac{e^{\alpha + \sum_{j=1}^n \beta_j x_{ij}}}{1 + e^{\alpha + \sum_{j=1}^n \beta_j x_{ij}}} \quad (3.5)$$

Where $p(x_i)$ is the probability of detection (0-1) of LEO hotspots, $\sum_{j=1}^n \beta_j x_{ij}$ represent the linear combination of n LEO hotspots FRP(in case of MODIS) within the AHI MIR pixel j , α and β_j are parameters derived from the data (Agresti, 1990; Morisette et al., 2005b; Schroeder et al., 2008a).

3.4.3 Calculation of Detection Time Differences

To further evaluate AHI-FSA fire-line pixels, it is essential to look at the AHI-FSA detections in the temporal domain. However, the study was limited to MODIS Terra satellite 10:30 UTC observations and MODIS Aqua satellite at 13:30 UTC observations during the daytime. AHI-FSA, on the other hand, has 18 observations between the two MODIS overpasses. It would be fair to assume that the AHI-FSA detections should fall between, and around, the two MODIS observations. The first AHI-FSA detection time was computed for each matched MODIS hotspot. The difference in detection time between AHI-FSA and MODIS was then calculated, and detections were categorised into three classes: AHI-FSA pre-detection, AHI-FSA synchronous-detection and AHI-FSA post-detection. Equation 3.6 describes the time threshold used, where Δt is the time difference between MODIS detection and the AHI-FSA detection. To include a minimum of two AHI observations either side of the MODIS detection a 40 minute window was used for synchronous-detections. For each category, the mean and standard deviation of the MODIS FRP values were also determined to provide an overall indicator of the fire intensity and size in these categories.

$$\begin{aligned}
 t_d \leq -20min & : AHI - FSA : Pre - detection, \\
 -20min < t_d \leq 20min & : AHI - FSA : synchronousdetection, \\
 t_d > 20min & : AHI - FSA : Post - detection.
 \end{aligned} \tag{3.6}$$

3.4.4 AHI-FSA Commission and Omission Error Calculation

As discussed in section 3.4.1 the performance of AHI-FSA would be better evaluated using a temporal intercomparison technique. However, due to lack of high temporal reference data, AHI-FSA omission error was aggregated to a daily product and compared to MODIS and VIIRS hotspots. By aggregating the detections the, temporal information is lost, but intercomparison is facilitated. The AHI-FSA aggregation includes 36 images captured from a six-hour window from 00:00 to 06:00 UTC. MODIS Terra and Aqua daytime observations were also combined to create a daily MODIS hotspot product. Omission was calculated based on the number of LEO hotspots with and without a matching AHI-FSA fire-line pixel.

Commission error was calculated using Landsat-8 digitized burn area, following the method employed by Hantson et al. (2013) and Koltunov et al. (2012). If the AHI-FSA pixel did not intersect the burn area, it was considered as a false detection. Similarly, for the determination of omission errors, a 500 m buffer was also used to account for AHI positional errors.

3.5 Results

During the study period, a total of 2474 MODIS hotspots, 11024 VIIRS hotspots and 18970 AHI-FSA fire-line pixels points were detected. FRP values for MODIS hotspots ranged from 4 MW to 700 MW with an

average FRP value of 84 MW and standard deviation of 189 MW indicating a range of fire sizes and intensities observed during the study period.

3.5.1 Thermal Hotspots Detection

Figure 3.4(a) & (b) show the probability of the AHI-FSA MIR condition detecting MODIS and VIIRS hotspots. The MIR condition has a 90% detection rate when a minimum of three MODIS hotspots, an FRP > 250 MW or 10 VIIRS hotspots occur within the MIR pixel. However, when the NIR and RED conditions are applied, initial MIR condition detections are filtered out due to the lack of change in the NIR and RED bands. This resulted in drops of approximately 50% and 30% in detection probability with respect to MODIS and VIIRS hotspots from the MIR detection rate. For example, Figure 3.4(c) indicates a 60% detection probability of detecting a 100 MW fire but this drops to 20% when incorporating the other conditions. A recent study by Xu et al. (2017) has also shown that AHI can detect fire with FRP value of 80 MW with 35% omission rate. The probability of the AHI-FSA MIR condition detecting a fire of a similar intensity (80 MW FRP) was 50%.

To further understand the performance AHI-FSA MIR condition, relative commission and omission errors were computed and are shown in Table 3.2. Compared to MODIS, the AHI-FSA MIR condition commission and omission errors were 43% and 47% respectively. It was interesting to see a very low VIIRS commission error of 6%, a considerable reduction compared to MODIS. This indicates that MIR condition is likely to be detecting fires that are not detected by MODIS. For example on 6th July, the AHI-FSA MIR condition identified 209 hotspots at 04:40 UTC. The MODIS Aqua overpass at 04:40 UTC confirmed 157 of those detections. Out of the 52 detections that are false detections relative to MODIS, 41 were confirmed to be true detections by VIIRS hotspots observed at 04:50. However, the AHI-FSA MIR condition also failed to detect 47% of MODIS hotspots. This amounted to 83 MODIS hotspots, most of which were isolated single hotspots. Out of these 83 MODIS detections, 69 detections were also detected by VIIRS. These results indicate the AHI-FSA MIR condition is detecting more fire hotspots in comparison to MODIS, however, at the same time failing to detect the majority of MODIS single hotspots. The improved detections in the MIR condition compared to MODIS hotspots could be due to: firstly, 14-bit radiometric resolution in the AHI MIR band compared to 12-bit in MODIS. Thus AHI MIR band should be more sensitive to changes in electromagnetic energy within the pixel compared to MODIS. Secondly, the AHI MIR radiance difference between fire and non-fire days facilitates the contextual threshold to detect small changes in radiance.

It is clear from the results that the AHI-FSA as a fire surveillance product would benefit greatly from the inclusion of the MIR condition detections at the 2 km resolution, providing an extra layer of information on top of the fire-line pixels.

TABLE 3.2: Commission and omission errors for AHI-FSA detections synchronous with LEO hotspots.

AHI-FSA Condition	MODIS		VIIRS	
	Commission	Omission	Commission	Omission
MIR	43%	47%	6%	51%
MIR + NIR	43%	49%	5%	56%
MIR + NIR + RED	35%	69%	1%	75%

TABLE 3.3: AHI-FSA detection times compared to MODIS detections as a proportion of MODIS hotspots and average FRPs

Detection Type	Proportion of MODIS hotspots (%)	Mean time difference between detections (mins)	Mean FRP and standard deviation (MW)
Pre-fire	73.7	-205	60.2 (± 74.0)
Synchronous	8.3	-6	60.6 (± 46.0)
Post-fire	17.8	144	34.5 (± 31.3)

3.5.2 Detection Time

Table 3.3 summarises the time difference between AHI-FSA detections with MODIS hotspots, where the AHI-FSA fire-line pixel coincides with the location of a MODIS hotspot. The high temporal frequency of AHI data enables the AHI-FSA to detect fire activity at the location of MODIS hotspots on average three hours before the MODIS overpass in 73% of hotspots. Around 8% of the AHI-FSA detections were synchronous with the MODIS detections. This trend seen in the pre and post-detection ratios is also visible in Figure 3.5. The two histograms show the count of AHI-FSA detections in 30 min sampling intervals on 4th and 6th of July 2016 over the study area. A negative time difference refers to a pre-detection and a positive time difference refers to post detection. Both graphs are skewed to the left, indicating early detection of fire activity at, or near, MODIS hotspots. MODIS hotspot FRP values in Table 3.3 indicates post detected fires tend to have a lower FRP value compared to pre-detected fires, 34.5 MW to 60.2 MW. In other words, the AHI-FSA is detecting high-intensity fire activity before the MODIS overpass, with lower intensity fires detected after the MODIS overpass. This could be due to either the fire being not large enough to be detected by the MIR condition, or AHI-FSA NIR and RED condition are not satisfied.

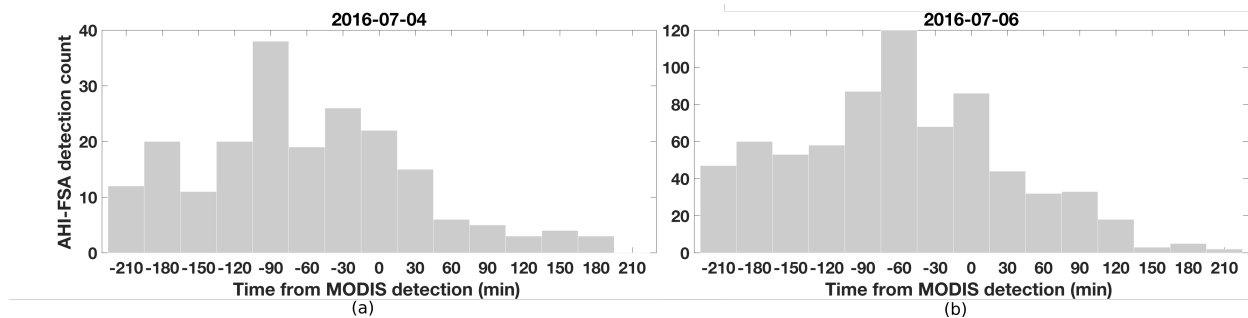


FIGURE 3.5: Daily comparison of AHI-FSA detections compared to MODIS hotspots on (a) 4th July and (b) 6th July 2016.

Figure 3.6 plots the time difference between the AHI-FSA detection and the nearest MODIS detection for a case study fire near Bulman Weemol (Northern Territory of Australia) on the 2nd of July 2016. The histogram in Figure 3.6(a), shows that AHI-FSA first detected the fire activity at the location of MODIS hotspots approximately 3.5 hours before the MODIS Aqua overpass. This is due to the extra five hours of observations available for AHI-FSA. The spatial distribution of the detections, as illustrated in Figure 3.6(b), shows that the contribution of high temporal observations also allowed AHI-FSA to describe the area of the fire with greater detail in comparison to MODIS hotspots. A total of 97% of the AHI-FSA fire-line pixels was within the visible burn area on the Landsat-8 image captured on 10th July 2016. A few synchronous pixels can be observed close to the MODIS detection, but most of the pixels surrounding the MODIS detection are detected before the MODIS overpass. This suggests that the AHI-FSA fire-line pixels are mapping the progression of the fire. Post MODIS detections tended to be observed at the edge of the burnt area.

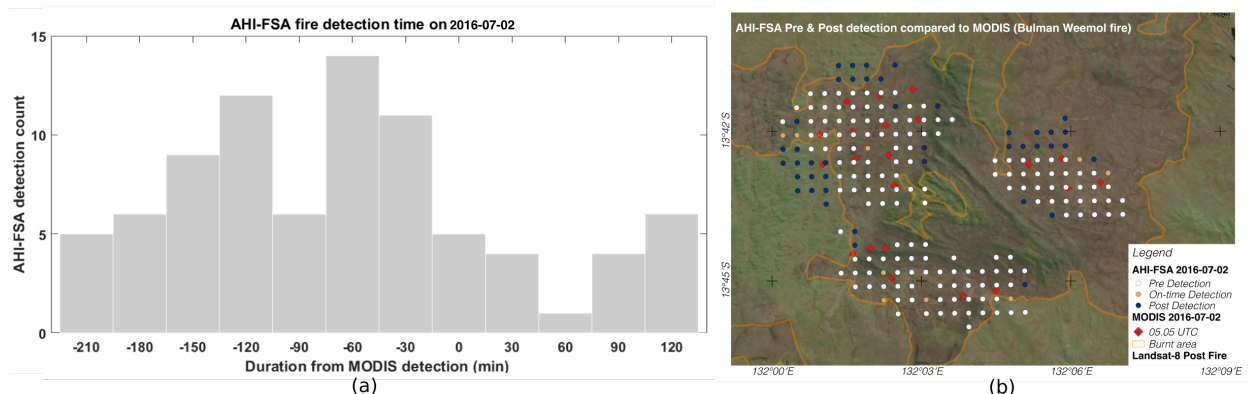


FIGURE 3.6: AHI-FSA early detection; fire near Bulman Weemol on 2nd July 2016. (a) Histogram showing the time difference between the AHI-FSA detection and the nearest MODIS detection for the fire. (b) Image showing the spatial distribution of the detections (pixel detections are converted to point data) showing pre and post detections on top of the post fire image captured on 10th July 2016 from Landsat-8.

3.5.3 AHI-FSA Commission and Omission Errors

Table 3.4 shows AHI-FSA as having a 7.1% relative omission error with MODIS, and 19.7% with VIIRS detections. These omission values are calculated using a six-hour AHI-FSA composite. Although this approach of calculating omission error does not account for the temporal accuracy of AHI-FSA detections, it facilitates an overall comparison of AHI-FSA with respect to LEO fire products.

In Table 3.4, the commission rate of AHI-FSA in comparison to the Landsat-8 burnt areas was 19.1% without applying a buffer for positioning correction, and dropped to 7% with the buffer applied. Hantson et al. (2013) calculated a commission rate of 3.6% over the same study area for MODIS hotspots when a 500 m buffer was applied to the burnt area product. Due to the lack of continuous observation for the duration of the fire, this method of calculating commission error loses some of the temporal detail. For example, for fires detected on 2nd of July 2016, the Landsat-8 pre-fire image was taken on June 24th, and the post-fire image on July 10th. This suggests that the actual area may have burnt after the detection, and therefore outside of the study period. In these cases, there is the potential for detections to be incorrectly flagged as correct. Nevertheless, the rate of commission calculated here is similar to previously reported commission errors for fire detection from geostationary satellites. For example, commission rates of 6-8% and 8% have been reported when comparing hotspots detected from the Fire Thermal Anomaly algorithm applied to Meteosat and AHI (Roberts & Wooster, 2008b; Xu et al., 2017) images respectively to synchronous MODIS hotspots.

Overall, the results shown here suggest that the AHI-FSA fire-line pixels product could potentially be used for coarse resolution fire burnt area mapping with 93% producer’s accuracy. In comparison, the MODIS fire hotspots based burnt area mapping accuracy is around 80% (Giglio et al., 2009)

TABLE 3.4: The daily relative omission error between AHI-FSA, MODIS and VIIRS hotspot products, and the commission error in comparison to Landsat-8 burnt areas.

Products (m)	Number of Hotspots	Without buffer	With buffer
MODIS Hotspot (1000 m)	2474	10.3%	7.1%
VIIRS Hotspot (375 m)	11024	33.4%	19.7%
Landsat-8 Burnt Area (30 m)	–	19.1%	7.0%

3.5.4 AHI-FSA in a Single Fire

The utility of AHI-FSA can be further understood by looking at a fire through a time sequence of detections. Figure 3.7 shows an hourly breakdown of a fire on July 4th near Claravale. AHI-FSA fire-line pixels are

aggregated into 50 minutes blocks. The background is post-fire Landsat-8 imagery taken on 10th July, which shows the burn scar as a dark-green/brown patch. Figure 3.7 (a) shows AHI-FSA fire-line pixels from 00:00-00:50 UTC. The previous nighttime MODIS hotspots are shown as green triangles and provide context to the fire before the AHI-FSA started mapping the fire-line pixels the following morning. The second Figure 3.7(b) shows AHI-FSA fire-line pixels from 01:00-01:50 with MODIS Terra detections at 02:05. Almost all of the AHI-FSA fire-line pixels fall around MODIS detections, except for the single MODIS detection in the south-east corner of the image. This isolated hotspot was never detected by AHI-FSA during the day and was also not detected by MODIS Aqua observation in the afternoon. Figure 3.7(c) shows a further progression of the two fire fronts in the southerly direction. A new fire is also observed to the centre of the image. Figure 3.7 (d), shows the growth in the new fire detected in the previous time stamp. There is also a new fire in the north-east corner of the image during 03:00 to 03:50. The VIIRS hotspots indicate that the AHI-FSA fire-lines pixels in the top north-east corner of the image at around 03:00 hours was a true detection that was not detected by MODIS. The next MODIS Aqua observation at 04:50 further confirms the new fire that was detected two hours earlier by AHI-FSA. It also confirms the top fire was moving in a southerly direction and the second (middle) fire was moving in a north-westerly direction. Figure 3.8 is a snapshot from the time series animation of the fire described in Figure 3.7 (the animation file is available with the digital copy of the paper). The animation shows the AHI true colour composite overlaid with AHI-FSA fire-lines every 10 minutes and synchronous MODIS detections when they occur. Figure 3.8 demonstrates the utility of the AHI-FSA as a fire surveillance tool, providing an indication of the fire size and moving direction of the fire.

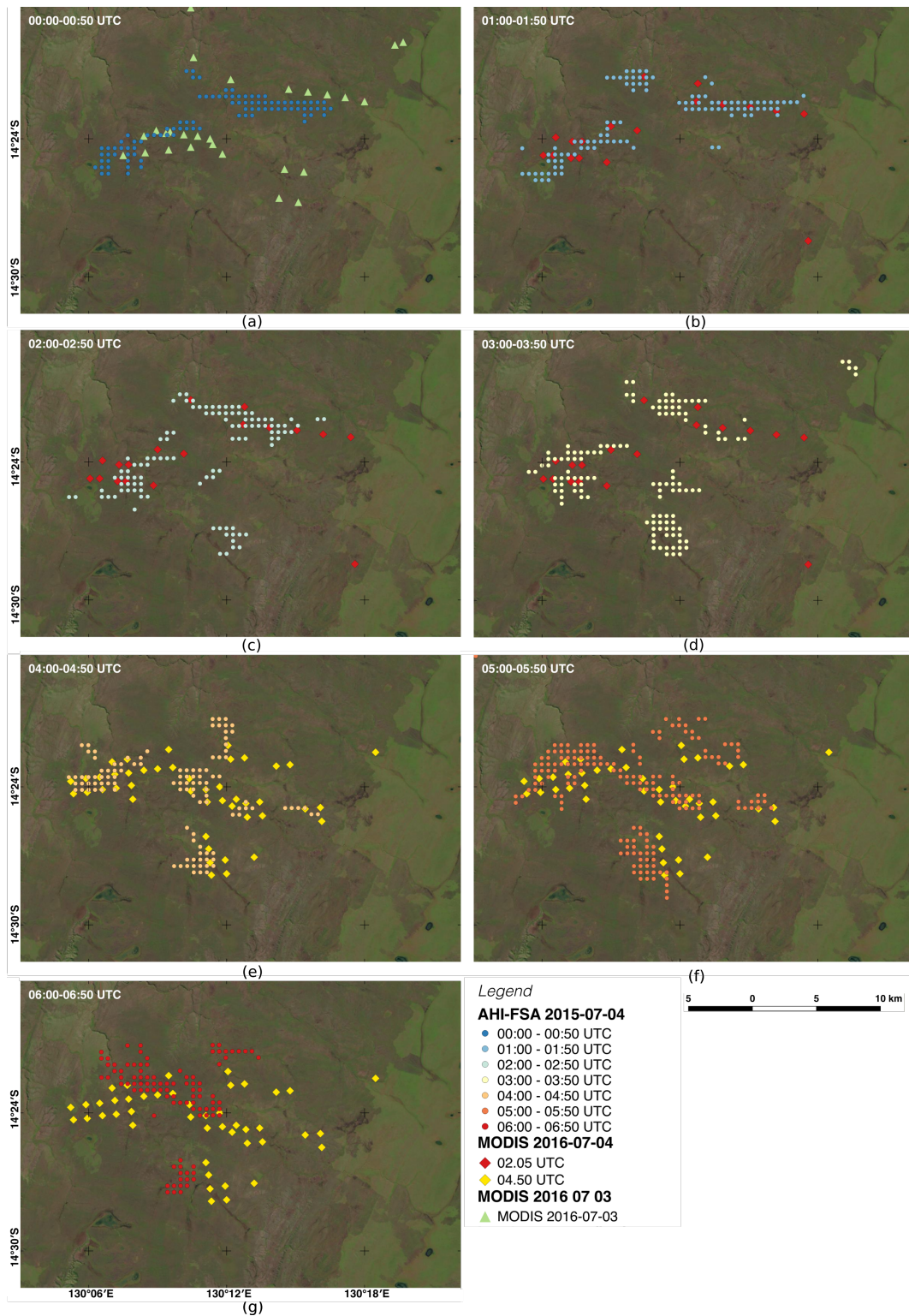


FIGURE 3.7: Single fire monitoring near Claravale, Northern Territory, Australia via AHI-FSA and MODIS on 2016-07-04. The Figure shows the sequence of hourly aggregations of AHI-FSA fire-line pixels overlaid with near synchronous MODIS hotspot detections. Images (a) to (g) show detections from 00:00 to 06:50 UTC and (h) shows the total AHI-FSA fire-lines during the day overlaid with MODIS Terra and Aqua daytime detections. Landsat-8 post-fire imagery was used as the background, showing dark-green/brown area as burn area.

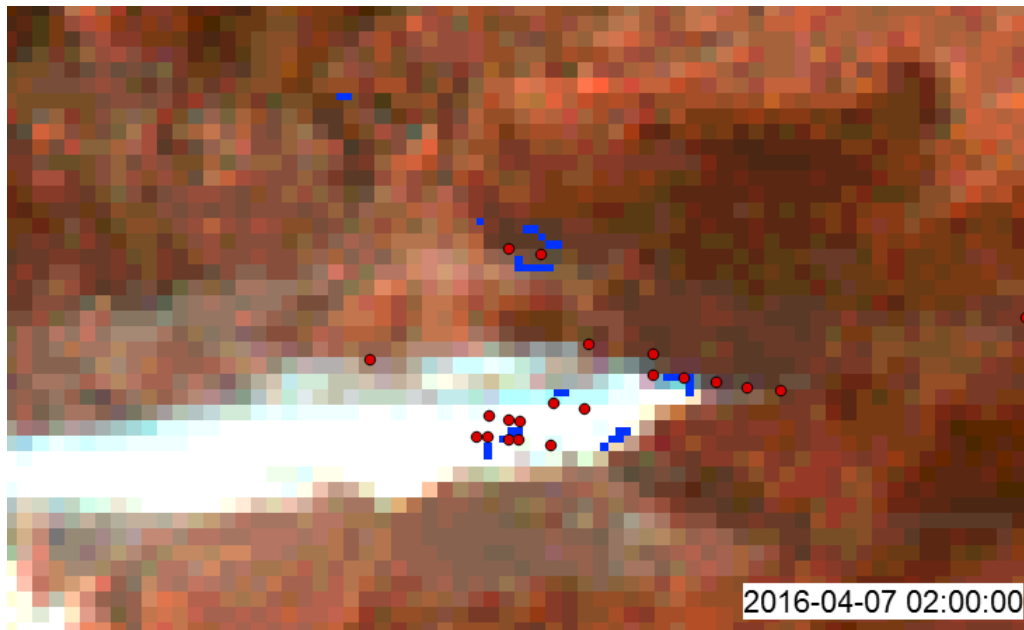


FIGURE 3.8: AHI-FSA fire-line pixels detection animation; large fire near Claravale on July 4th.

3.6 Conclusion

The purpose of this paper was to evaluate the application of AHI-FSA as a fire surveillance algorithm. A method for the intercomparison of high temporal fire surveillance products with existing LEO fire products was also presented. Using this method, AHI-FSA relative omission error was calculated compared to MODIS and VIIRS fire hotspots for an area of 1.4 million square kilometres in northern Australia. The AHI-FSA MIR condition reported over 90% probability of detecting a fire when at least three MODIS hotspots were within the MIR pixel. The relative accuracy of the AHI-FSA MIR condition reported 43% and 6% commission error when compared to MODIS and VIIRS respectively. Relative omission error was reported as 47% compared to MODIS and 51% compared to VIIRS hotspots. However, when all AHI-FSA conditions were applied, a relative omission error of 7.1% compared to MODIS was reported, with a 70% chance of detecting fire activity at the location of the MODIS hotspot before the MODIS overpass. AHI-FSA fire-line commission error was reported at 7% when compared to Landsat-8 burnt areas. The low commission error demonstrates the multi-scale approach used was successful in mapping the sub-pixel level fire within the AHI 2 km MIR band.

Using AHI-FSA, the progression of an individual fire was also determined. This fire progression description indicated that AHI-FSA could provide detailed and near-continuous fire behavior information, such as direction and the rate of fire spread. This documentation of fire movement demonstrates that AHI-FSA can effectively be used for wildfire surveillance in open woodland/grassland fires, providing valuable information to fill in the data gap between MODIS Terra and Aqua observations.

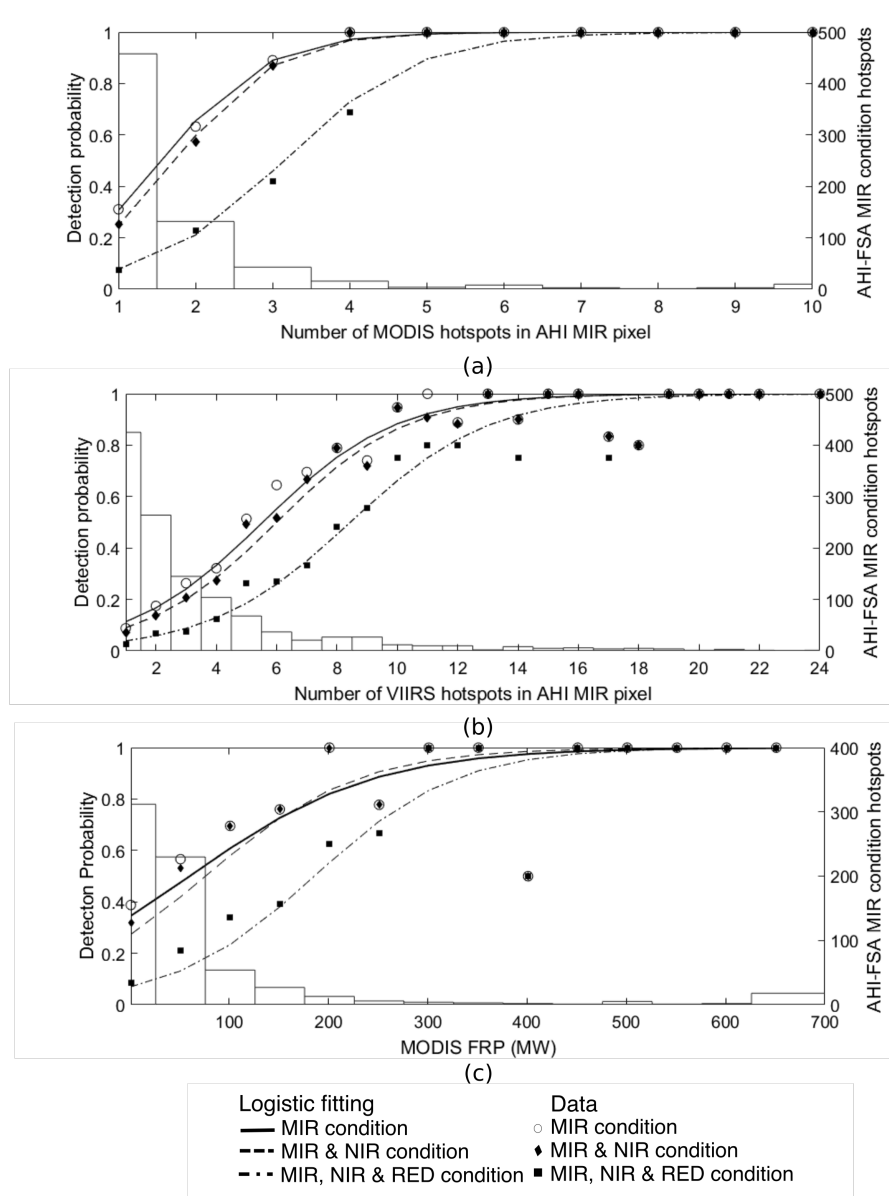


FIGURE 3.4: AHI-FSA MIR condition thermal anomaly detection probability compared to MODIS, VIIRS hotspots and MODIS FRP values. AHI-FSA MIR hotspot counts shown as a histogram.

4

Multi-level wildfire surveillance using geostationary satellites

This chapter is based on: *(in review) Wickramasinghe, C., Wallace, L., Reinke, K. and Jones, S., in review Remote Sensing*

Abstract

The geostationary satellite can play an important role in active wildfire surveillance. AHI(Advanced Himawari Imager) onboard Himawari-8 geostationary weather satellite covers the Asia and Australia region every 10 minutes providing high temporal data. AHI-FSA (Advance Himawari Imager-Fire Surveillance Algorithm) is a new algorithm that aims to utilise attribute of the next generation of geostationary weather satellites such as Himawari-8. Taking advantage of multi-resolution channels and the high temporal data. AHI-FSA provides two levels of information, 2 km thermal hotspots and the 500 m fire-line pixels. Initial testing over the Northern Territory of Australia has demonstrated the high potential of the algorithm for fire surveillance. This paper aims to inter-compare AHI-FSA products against existing VIIRS (Visible Infrared Imaging Radiometer Suite) hotspots. Looking at an annual data-set over different fire-prone landscapes in Australia. Results demonstrate the AHI-FSA capability to detect fires as small as 14 ha with around 40 % probability assuming the VIIRS product is correct in the Northern part of Australia. Further more AHI-FSA 500 m provides improved fire surveillance capability at 500 m ground resolution for large fires with relatively low commission error.

4.1 Introduction

Wildfire surveillance is an essential component of risk management in response to ignitions in fire prone landscapes(Stipani et al., 2010). While a number of systems exists for wildfire surveillance, a key component of modern wildfire surveillance approaches is the use of satellite detected hotspots. Geoscience Australia Sentinel Hotspots service provides a web mapping system that provides timely thermal anomalies detections to emergency services across Australia. The system uses three low earth orbiting (LEO) satellites based products to provide a combined total of six to seven observations per day over a given area. The three LEO sensors are; Moderate Resolution Imaging Spectroradiometer (MODIS) sensor onboard the Terra and Aqua satellites, providing 1 km hotspots with daily coverage of 3-4 observations per day (Giglio et al., 2016); Advanced Very High Resolution Radiometer (AVHRR) from the National Oceanic and Atmospheric Administration (NOAA) satellite that provides a single 1 km hotspots detections during the night and the Visible Infrared Imaging Radiometer Suite (VIIRS) on-board Suomi National Polar-orbiting (S-NPP) satellite provides a 375 m hotspot product with two observations per day (Data.gov.au).

LEO satellite based wildfire detection, as used in the Sentinel hotstop service, is limited by the low temporal resolution of the satellites. Geostationary satellite based systems on the other hand can provide high temporal frequency data every 10-30 min. For example, the Wildfire Automated Biomass Burning Algorithm (WF-ABBA) hotspots product has been operational since the year 2000 using Geostationary Operational Environmental Satellite (GOES)(Koltunov et al., 2012). WF-ABBA delivers a 4 km hotspots product covering both the Northern and Southern American regions every 30 minutes (Prins & Menzel, 1994b;

Prins & Schmetz, 1999). Over Europe and Africa, the SEVIRI (Spinning Enhanced Visible and Infrared Imager) sensor on-board the MSG (Meteosat Second Generation) satellite provides data for the SEVIRI Active Fire Monitoring (FIR) product, available every 15 minutes with 3 km ground resolution (Laneve et al., 2006; Sifakis et al., 2011b; Eumetsat). This examples demonstrate that the high temporal resolution data provided by geostationary satellites offers the ideal platform for active wildfire surveillance with regarding to temporal frequency. WF-ABBA and FIR respectively have reported capability to detect fires as small as 0.15 ha at 759 K and 0.22 ha at 750 K near the equator (Prins et al., 2001).

A number of recent studies have demonstrated the potential for using the Advanced Himawari Imager (AHI) sensor onboard the Himawari-8 geostationary satellite for wildfire detection and monitoring with a 2 km spatial resolution Hally et al. (2018, 2017); Xu et al. (2017); Xu & Zhong (2017). Xu et al. (2017), calculated an 8% active fire commission error and 66% omission error compared to MODIS when Fire Thermal Anomaly (FTA) active fire detection algorithm was applied. While Hally et al. (2017) utilised the multi-temporal information provided by AHI in order to further enhance the detection capabilities of this sensors. Nevertheless, in all of the fore mentioned studies the spatial resolution is limited to 2 km, thus making the high temporal data redundant.

To further enhance the capabilities of the geostationary sensors Wickramasinghe et al. (2016) introduced the AHI Fire Surveillance Algorithm (AHI-FSA). AHI-FSA provides multiple levels of wildfire surveillance data. AHI-FSA 2 km a thermal hotspots detection and the AHI-FSA 500 m which is a fire-line pixel detection. AHI-FSA 500 m achieves a higher spatial resolution by using a unique multi-resolution approach to map fire-line pixels. Furthermore, a recent implementation of the FSA algorithm on SEVIRI has demonstrated an improvement in spatial resolution from 3 km to 1 km during the daytime with similar detection accuracy in comparison to previously utilised algorithms (Wickramasinghe et al., 2018).

Initial studies under best-case scenario, with low cloud cover, in open woodland/grassland fire landscapes have shown the potential of the algorithm as a tool for near real-time fire surveillance over Australia. Given the potential use of AHI-FSA for wildfire monitoring it is imperative that AHI-FSA performance is further validated. This paper aims to validate the performance of AHI-FSA algorithm, work presented herein inter-compares AHI-FSA with VIIRS hotspot products over Australia's fire-prone landscapes using an annual data-set (2016).

4.2 Materials and Methods

4.2.1 VIIRS hotspots

VIIRS hotspot is a 375 m ground resolution thermal anomaly hotspot product with twice daily observations (Schroeder et al., 2014). VIIRS hotspots have a higher spatial resolution compared to the AHI-FSA 500 m

fire-line pixels making it the most suited LEO based hotspots product for intercomparison. VIIRS has demonstrated 100% detection capability of fires larger than 100 ha over the Northern Territory of Australia (Oliva & Schroeder, 2015), with an omission error of 60% for fires ranging from 10 to 25 ha in size. For this study, VIIRS fire hotspots (*VNP14IMGML*) data were used (available from <ftp://ladsweb.nascom.nasa.gov>).

4.2.2 Study Area

The initial study area was selected using 200×200 km grids every two degrees interval along a great circle between Batmans Bay in New South Wales, Australia and Mary Island in Western Australia, Australia. The great circle was selected as a latitudinal cross-section across Australia cutting across high fire frequency, low economical value native woodlands/forests as well as low fire frequency by high economical value agricultural areas to capture a detailed cross-section of land cover and environmental regions across Australia. An additional five study grids were also selected, identified as N1, Q1, Q2, V1 and W1 to ensure that the full range of tree cover classes are included in the study. As grids 3,4,5,6 and 7 did not satisfy the minimum number of 500, VIIRS hotspots during the year 2016, thus were removed from analysis in the study. The nine grids evaluated (1, 2, 8, 9, N1, Q1, Q2, V1 and W1) in the study covers an area of 360 000 km². Figure 4.1 shows the study grids placement over Australia. Table 4.1 below shows the count of VIIRS hotspots for each grid during the daytime for the year 2016.

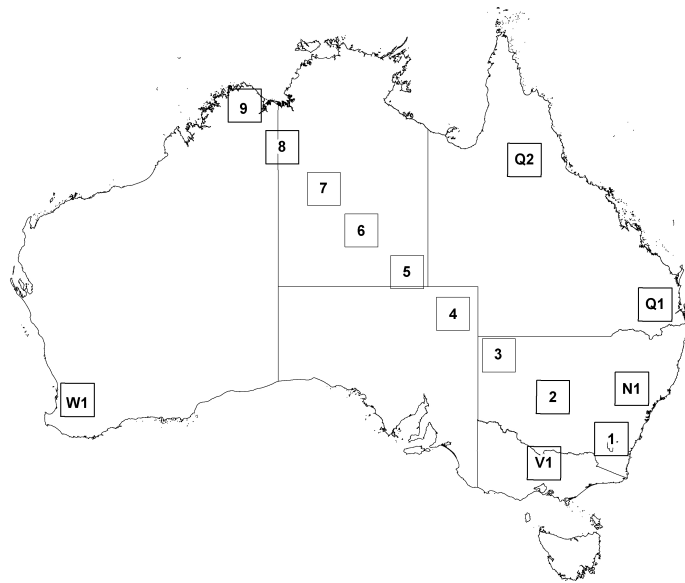


FIGURE 4.1: Study area grids selected across Australia for the study.

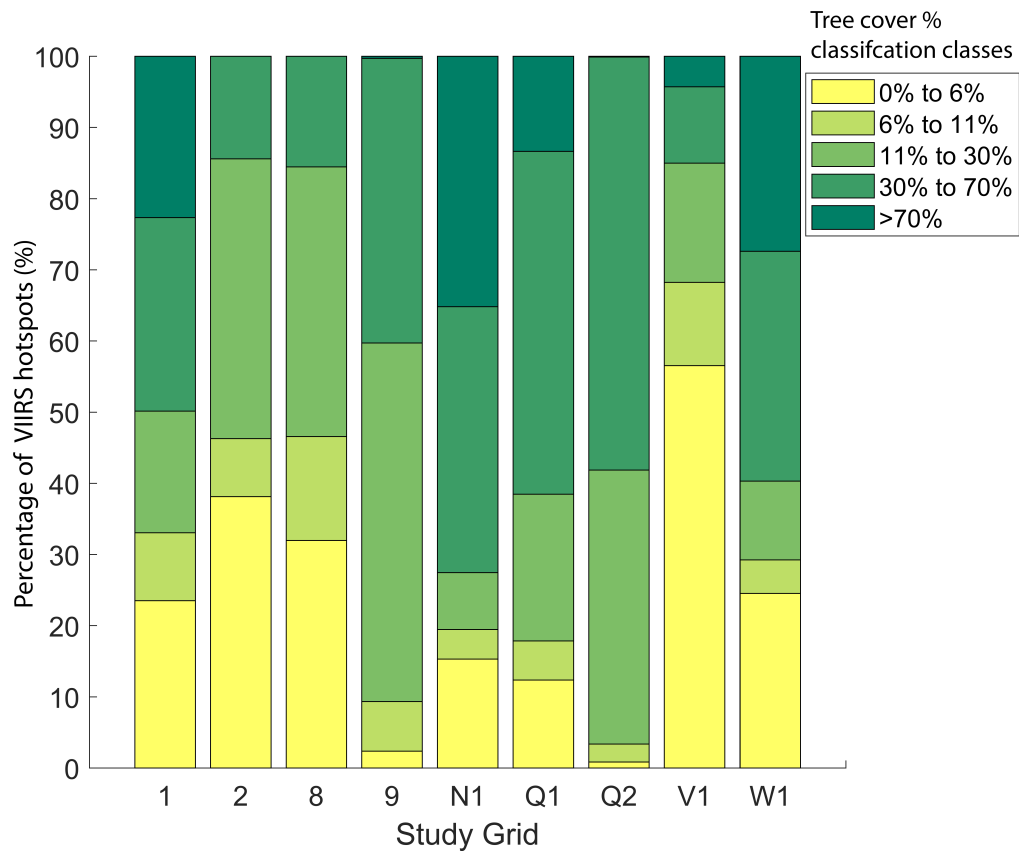


FIGURE 4.2: The percentage of VIIRS hotspots that fall within in each tree cover category in each grid for the year 2016. Tree cover data are based on Australia-wide vegetation height and structure data available at <http://data.auscover.org.au/> (Joint Remote Sensing Research Program, 2012).

4.2.3 Tree/Vegetation Cover

Tree canopy cover can obscure observation of smaller, lower intensity fires. Figure 4.2 shows the percentage of VIIRS hotspots in each grid based on the tree cover category. The tree cover percentage categories are based on tree structural formation (Vegetation height and structure - derived from ALOS-1 PALSAR, Landsat and ICESat/GLAS, Australia coverage) (Joint Remote Sensing Research Program, 2012). The structural formation of the tree cover categories is as follows; low scattered trees and medium scattered trees fall into the (0%-6%) category, medium open woodland and tall open woodland <17m (6%-11%), low woodland to very tall woodland over <27 m (11%-30%), low to very tall open forest ranging from 9-27 m are in the (30%-70%) category and tall closed forest >17 m falls in to the (>70%) category.

TABLE 4.1: The number of VIIRS hotspot within each study grid in the study period (2016). As grids 3, 4, 5, 6 and 7 have less than 500 VIIRS hotspots they were not analysed further.

Study Grid	VIIRS hotspots
1	1659
2	1295
3	0
4	50
5	0
6	74
7	285
8	2591
9	27881
N1	729
Q1	4411
Q2	4869
V1	932
W1	5461

4.2.4 AHI-Fire Surveillance Algorithm(AHI-FSA)

Existing fire detection algorithms utilise on only the thermal infrared (TIR) and middle infrared (MIR) channels and often only a single image to calculate the background temperature using a contextual threshold-based approach (Kaufman et al., 1998; Schroeder et al., 2008b, 2014; Giglio et al., 2008b). In contrast, the AHI-FSA depends on a cloud-free, non-fire day composite image to calculate the background temperature in addition to the fire day image. AHI-FSA also adopts a multi-resolution approach by including the MIR, near infrared (NIR) and RED channels available on the AHI sensor to provide improved spatial resolution.

The AHI-FSA applies three independent threshold conditions to MIR, NIR and RED channels to detect fire-line pixels(Wickramasinghe et al., 2016). In AHI-FSA, a fire day image is referred to the image captured on the day of the fire. A non-fire day image is a cloud and fire free composite image with the same time stamp as the fire day. The non-fire day composite image is generated using up to 14 day image composit (modified from 10 days as used in the original implementation of the algorithm) previous to the day of the fire. The three conditions are designed to detect thermal anomalies, changes in vegetation cover due to fire, and the edge between smoke and non-smoke pixels. The first condition is the MIR condition where thermal

anomalies are detected using a contextual based approach. Outputs from "MIR condition" are the first layer of data available for fire surveillance named AHI-FSA 2 km detections. The second layer of data available through AHI-FSA is the AHI-FSA 500 m fire-line pixels. AHI-FSA 500 m fire-line pixels are detected when all three AHI-FSA conditions are satisfied. Image selection and the three threshold conditions are briefly explained below. It should be noted that the MIR condition has been slightly modified from the original algorithm for this study. Please refer to Wickramasinghe et al. (2016) for detail description of the algorithm.

- Fire day image: Image captured on the day of the fire at a particular time.
- Non-fire day image; cloud-free and fire free composite image generated using the median value of the cloud free pixel values from 14 images captured at the same time to that of the fire day image within the previous fortnight.
- MIR Condition: The 3.9 μm MIR channel is used to detect thermal anomalies using a contextual threshold. We have slightly modified background temperature estimation rather than using the fire day and non-fire day difference image in the contextual thresholding equation (4.1). The modified condition uses the non-fire day image. A dynamic contextual threshold is then applied to the MIR difference image to detect thermal anomalies. The initial 3×3 kernel is expanded to 5×5 if 65% valid pixel threshold is not reached. Valid pixels are non-cloud, non-fire and non-water pixels. If f_i is over 1 the pixel is identified as a detection where $MIR - TH$ is a threshold constant.

$$f_i = \Delta M_i - [\mu_{M_{n_f}} + MIR - TH \times \sigma_{M_{n_f}}] \quad (4.1)$$

where ΔM_i is the MIR radiance differences of the target pixel between fire day and non fire day pixels with similar time stamp for the target pixel, $\mu_{M_{n_f}}$ and $\sigma_{M_{n_f}}$ are the mean and standard deviation of the MIR radiance difference of all background pixels in the kernel:

- NIR Condition: Change in the NIR channel is used to identify changes in vegetation cover. A NIR difference image is calculated using fire day and non-fire day imagery. The rate of change in the difference NIR image is then calculated. Pixels with higher than -1% slope are flagged as a pixel with a rapid negative change in vegetation cover.
- Red Condition: In this condition, the reflectance difference between a fire day and a non-fire day is calculated for the RED channel. A high pass filter is then applied to amplify variations in reflectance further. Edge detection is then used to determine the boundaries between the smoking and burnt/burning areas.

4.3 Intercomparison Method

Cloud cover is an important variable for many wildfire detection algorithms. Contextually based algorithms require cloud pixels to be masked out before calculating the local contextual threshold values as their inclusion leads to an incorrect estimation of background surface temperature. An accurate cloud mask can reduce mixed pixels that are included in the background temperature calculation. Cloud contaminated pixels leads to false detection as the cloud mixed pixel will have a lower thermal radiance compared to the ground surface. Thus, the accuracy of the AHI cloud mask plays an essential part in the overall performance of the algorithm. However, the validation of AHI cloud mask is beyond the scope of this paper.

Cloud masks can also introduce relative omission error when intercomparing products from two different satellites, further amplified when the two products have two different spatial resolutions. For example, AHI cloud mask has a ground resolution of 2×2 km compared to 0.37×0.37 km in VIIRS. If a cloud is only partially covering the 2×2 km pixel, the entire AHI pixel will be masked out. Whereas, the VIIRS having a higher spatial resolution will be able to detect fires within the cloud-free portion of the 2×2 km AHI pixel. Freeborn et al. (2014) calculated that 30% of the omission error in the SEVIRI FIR algorithm detections were due to cloud when compared to MODIS hotspots.

To overcome this problem in this study VIIRS hotspots are also filtered using AHI cloud mask leaving only the VIIRS hotspots that fell within an AHI non-cloud pixel. Figure 4.3 shows the intercomparison method work flow used in this paper. As shown in Figure 4.3, the AHI-FSA 2 km product is intercompared with both the VIIRS hotspots and VIIRS hotspots that have been masked using the AHI cloud mask. This allows for the quantification of false negatives introduced by the AHI cloud mask when intercomparing the two products. The majority of the fires detected by AHI-FSA will be sub-pixel fires. Thus it is essential to understand the AHI-FSA fire detection probability relative to fire size. In this study a single VIIRS hotspot pixel was used as the minimum fire size to calculate the AHI-FSA 2 km fire detection probability. Finally, AHI-FSA 500 km fire-line pixels commission and omission errors were calculated to evaluate the performance of the improved spatial resolution available via the AHI-FSA algorithm.

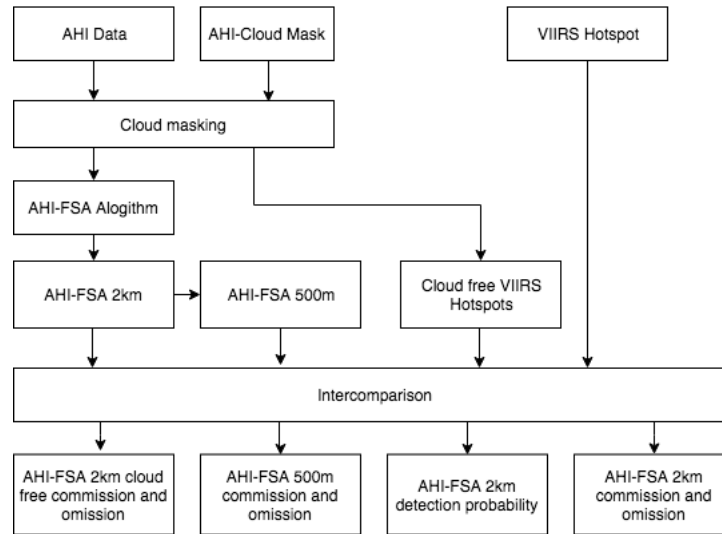


FIGURE 4.3: The intercomparison work flow illustrating how the AHI cloud mask is used when intercomparing AHI-FSA with VIIRS hotspots. AHI-FSA 2 km commission and omission errors are calculated with, and without, the AHI cloud mask. AHI-FSA 500 km commission/omission errors and AHI-FSA 2 km fire detection probability was calculated with the AHI cloud masked VIIRS hotspots data.

4.3.1 Cloud cover

The original AHI-FSA algorithm considers a 10 day period before the fire to compute the non-fire day image. As this paper is looking at an annual data-set through different climate zones, the number of days used to compute the non-fire day image was extended to 14 days as the 10 day period is not sufficient to generate the cloud free non-fire day image. The non-fire day image is computed by taking the median value of the cloud-free pixels in the 14 day period. The higher the number of valid non-fire day pixels, the more accurate the background temperature calculation is likely to be. However, in temperate climates getting a considerable number of valid non-fire pixels can be challenging due to the high presence of cloud cover. Thus, it is important to look at the impact of cloud cover on the non-fire day image computation. Furthermore, as described earlier, cloud cover on a fire day can also introduce omission errors in the intercomparison calculations. To quantify the number of VIIRS hotspots that are masked out by AHI cloud mask, the number of VIIRS hotspots available for intercomparison after applying the AHI cloud mask is shown in Table 4.2 as a percentage of the total VIIRS hotspots for three scenarios. 1) When only the fire day AHI cloud mask is applied to VIIRS hotspots. The second and third scenarios also takes in to account the null pixels in the AHI-FSA non-fire day image due to the cloud. For example, if non-fire day image computation requirement is three minimum cloud-free images and a particular pixel has only two cloud-free days within the 14 day period, the pixel will have a null value in the non-fire day image. 2) when a minimum of three days of cloud free imagery from the 14 pre-fire days are required to compute the non-fire day image, and (3) when a minimum

of four days of cloud free imagery are required to compute the non-fire day image. Based on these results the minimum number of cloud-free images required to compute the non-fire day image was fixed to three images.

4.3.2 AHI-FSA 2 km commission and omission error calculations

Previous studies which intercompared SEVIRI thermal hotspot products against MODIS hotspots, assigned each MODIS detection to overlapping SEVIRI pixels removing the resolution difference between the products (Roberts et al., 2015; Freeborn et al., 2014). This effectively re-sampled the MODIS products to 3 km grids. This approach was also adopted by Xu et al. (2017) to evaluate the implementation of FTA algorithm on AHI. We adopted the same approach to intercompare VIIRS hotspots with AHI-FSA 2 km. VIIRS hotspots were selected over MODIS for intercomparison in this study as VIIRS hotspots provide 375 m ground resolution at nadir, which is higher than the AHI-FSA 500 m fire-line pixel ground resolution of 500 m.

VIIRS detections were mapped to overlapping AHI 2 km MIR grid. Each VIIRS detection was then intercompared with AHI-FSA 2 km detections within ± 6 min of VIIRS observation. Omission error was calculated by considering a 5×5 window surrounding VIIRS detections. When the AHI-FSA 2 km detection does not fall within this window the VIIRS detection is considered a false detection. The error of commission was triggered when an AHI-FSA 2 km detection has no matching VIIRS hotspots within the corresponding 5×5 pixel window (Freeborn et al., 2014). As the current study evaluates the performance of the algorithm in different landscapes and climate conditions, it is only fitting that the need of optimization of AHI MIR condition threshold (MIR-TH) value is also evaluated. Thus, AHI-FSA 2 km commission and omission errors were calculated for a range of MIT-TH values.

4.3.3 AHI-FSA 2 km fire detection probability

Commission and omission error calculations do not provide a complete understanding of the fire detection capabilities of the algorithm. To quantify the sub-pixel fire detection capabilities of AHI-FSA 2 km, AHI cloud masked VIIRS hotspots were used. By taking the single VIIRS hotspots as the smallest unit the AHI-FSA 2 km fire detection probability was calculated compared to VIIRS. The number of VIIRS hotspots within each AHI 2 km pixel was calculated. AHI-FSA detection probability was then calculated through statistical logistic regression model defined below in equation 4.2. (Schroeder et al., 2008a; Morissette et al., 2005a).

$$a = \alpha + \sum_{j=1}^n \beta_j x_{ij} \quad (4.2)$$

$$P(x_i) = \frac{e^a}{1 + e^a} \quad (4.3)$$

where $p(x_i)$ is the probability of detection (0-1) of LEO hotspots, $\sum_{j=1}^n \beta_j x_{ij}$ represents the linear combination of n LEO hotspots within the AHI MIR pixel j , α and β_j are parameters derived from the data (Agresti, 2003; Morisette et al., 2005b; Schroeder et al., 2008a).

4.3.4 AHI-FSA 500 m commission and omission error calculation

AHI-FSA 500 m fire-line pixels provide relatively higher resolution wildfire surveillance capabilities during the daytime as compared to the AHI-FSA 2 km. AHI-FSA fire-line pixels map the edge between smoke and burnt area, effectively identifying the location of the sub-pixel fire within the AHI 2 km MIR pixel. The difference in spatial/temporal resolution between the VIIRS hotspot products and the AHI-FSA 500 m fire-line pixels makes it difficult to directly compare the two products. Thus when comparing AHI-FSA 500 m against VIIRS hotspots a ± 30 minute temporal window was used, thus providing AHI-FSA 500 m more opportunity to detect fire-line pixels. Similar pixel-based approach to that of AHI-FSA 2 km commission and omission error calculation was then used. The kernel size was expanded to 10×10 to have the same search area as with the AHI-FSA 2 km commission and omission error calculations.

4.4 Results

4.4.1 Fire occurrence

A total of 12,999 VIIRS hotspots were intercompared in this study. A breakdown of the hotspots in each grid is shown in Table 4.1. Due to lack of fire activity (less than 500 hotspots), only 9 grids out of the initial 14 grids were examined in detail. Grid 9 has the highest amount of fire activity with almost four times the number of hotspots than the second highest grid W1. Just over 50 % of the fires in grid 9 were in the 11 %-30 % tree cover percentage as shown in Figure 4.2. Grid V1 shows the highest percentage (56 %) of fire with very low tree cover in the 0 %-6 % range. Based on the location, fire in the 0 %-6 % tree cover area are predominantly pasture land fires in grids 1, 2, N1, Q1 and V1. Whereas fires in grids 8 and W1 tended to be in grasslands. High tree cover fires were observed in grids N1, W1, 1, Q1 and V1 with the highest percentage of fires occurring in grid N1.

4.4.2 Background temperature estimation

AHI-FSA background temperature is computed using 14 days of pre-fire imagery. By only using the cloud and fire free pixels from the 14-day preceding a fire the algorithm tries to minimize the impact of cloud on the background image. However, due to constant cloud cover in temperate regions, it is not possible to compute a 100 % cloud-free non-fire day image for the study grids. As pointed out earlier when intercomparing products

TABLE 4.2: The percentage of VIIRS hotspots pixels that are unobstructed by the AHI cloud mask for three scenarios. When AHI cloud mask is applied only for the fire day, when a minimum of three days of cloud free data are available to compute the non-fire day image from 14 day period and finally when minimum of four day of cloud free data are required for non-fire days image computation.

Study Grid	Cloud on fire day (%)	Three minimum non-fire days (%)	Four minimum non-fire days(%)
1	54.8	47.5	40.4
2	79.0	66.7	59.1
8	73.7	59.7	55.9
9	82.5	68.5	57.7
N1	56.6	35.8	24.6
Q1	68.2	51.4	41.2
Q2	76.4	62.4	45.7
V1	63.5	52.1	43.2
W1	63.1	42.7	30.3

cloud masks can introduce omission errors. This can lead to problems where the fire pixel is masked out by the low-resolution sensor cloud mask.

Table 4.2 shows the available VIIRS hotspots for inter-comparison after applying AHI cloud mask as a percentage of the total VIIRS hotspots for each grid. In grid 1, 45.2% of VIIRS hotspots are masked out by AHI cloud mask on the fire day. This number increases to almost 59.6% when the background image computation requires a minimum of four cloud-free days. Based on the Bureau of Meteorology, Australia average annual cloud distribution data; grids 1,2, Q1, Q2, V1 and W1 have an okta (okta is a unit of measurement used to describe the amount of cloud cover at any given location such as a weather station) value of 3 to 4 Bureau of Meteorology (2018). Okta value ranges from 0 oktas (completely clear sky) through to 8 oktas (completely overcast) and a value of 3-4 is considered as scattering clouds. These grids also fall into the temperate climate zones with constant cloud cover through out the year. The highest percentage of VIIRS hotspots available for intercomparison after applying the AHI cloud mask was 82% in grid 9, when only the fire day cloud mask is applied. This number also drops to 57% when the minimum cloud-free pixels required to compute the non-fire day image is set to four. Similar drops were recorded in the other grids with grids N1 and W1 losing almost 70% of VIIRS hotspots. Based on the above results the minimum number of cloud-free images required to compute the non-fire day image was fixed to three images.

4.4.3 AHI-FSA 2 km Commission and Omission

AHI-FSA 2 km commission and omission errors are calculated with (Cloud free intercomparison) and without (intercomparison) the AHI cloud mask applied to VIIRS hotspots. Figure 4.4 compares the two commission and omission errors with varying MIR-TH values. Commission error values in both scenarios showed very similar variation gradually decreasing with the increase in MIR-TH value. Starting in the 80–90 % mark and progressively reducing down to almost 50 %. Omission error shows a gradual increase as expected with MIR-TH value. The omission error introduced by the AHI cloud mask is visible from the gap between the intercomparison and cloud-free intercomparison results. Grids N1, Q1 and W1 show almost 60 % difference between the two omission errors, whereas the grids 2 and 9 only shows a 20 % difference. Intercomparison omission error starts just over the 50 % mark for most of the grids except for grids 2 and 9. Cloud-free intercomparison omission error starts at a much lower level and stays below 30 % mark for most of the grids at the MIR-TH value of 5. The highest algorithm omission error is observed in grid 1 and Q1 with 46 % and 34 % respectively at the MIR-TH value of 5.

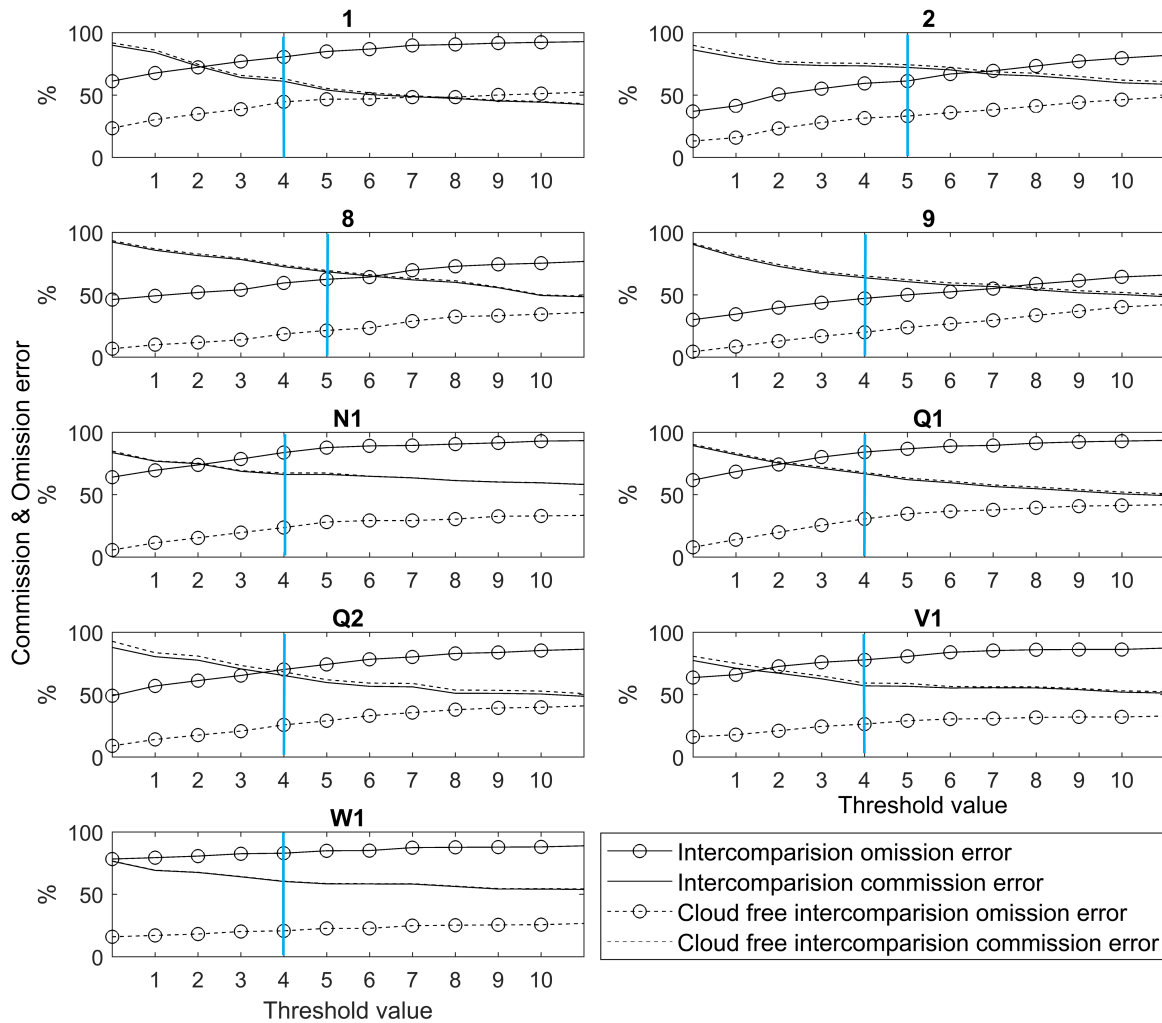


FIGURE 4.4: Commission and omission error calculation compared to VIIRS hotspots. Results for both intercomparison and cloud-free intercomparison are computed for a range of threshold values. The blue vertical lines mark the MIR threshold values used to calculate the balance AHI-FSA 500 m fire-line pixels in Section 4.4.5.

4.4.4 Detection probability VIIRS hotspots

Detection probability estimates the likelihood of AHI-FSA detecting a VIIRS hotspot. The possibility of detecting a single VIIRS hotspot which is 25 times smaller compared to AHI MIR pixel provides a good estimation of the sub-pixel detection capability of the AHI-FSA 2 km. Detection probability discussed below refers to detection probability at MIR-TH value of 5 unless specified. Figure 4.5 shows there is a 40% probability of detecting a single VIIRS hotspot in grids 8 and 9. Grids 2, Q1 and Q2 shows 22% & 31% detection probability. The lowest detection values were reported in grid 1 (8%). As expected the detection probability increases with the number of VIIRS hotspots in all grids except grid Q2. Grid Q2 has low

fluctuating detection probability that is not increasing with the size of the fire (number of VIIRS hotspots). Grid Q2 also shows three fires with 18 VIIRS hotspots within the AHI MIR pixels. These fires could cover almost 72% of the AHI MIR pixel, a considerably large fires. Out of these three fires, only one was detected at MIR-TH values 1 and 5, none of the fires were detected at MIR-TH 10, indicating these are most likely very low-intensity grass fires.

4.4.5 AHI-FSA 500 m Commission and Omission

AHI-FSA 500 m provides 500 m ground resolution fire-line pixels. Figure 4.6 compares the AHI-FSA 500 m commission and omission error calculations for three scenarios based on the MIR-TH values. 1) Balance commission and omission error, 2) minimum omission error, 3) minimum commission error for AHI-FSA 500 m fire-line pixels. Demonstrating the flexibility of AHI-FSA to control AHI-FSA fire-line pixel commission and omission error based on the end user requirement by adjusting the MIR-TH value. MIR-TH values selected for balanced commission and omission error calculation are marked with blue vertical lines in Figure 4.4 calculated by taking the MIR-TH values with the mean combined error. To calculate the minimum omission and minimum commission error MIR-TH values 1 and 10 were used respectively.

Figure 4.6 (a) shows the results for balanced MIR-TH commission and omission values. With an average commission error of 32% and average omission error of 45% across all grids. Lowest commission error was in 23% in grid V1 and lowest omission error was in grid 8 which was 30%. Figure 4.6 (b) shows results when MIR-TH values were adjusted to provide minimum omission error. This reduces the grid 9 and Q1 omission error by 14% and 9% respectively. On the other hand increases the commission error in all grids with the highest increase observed in grid 1, 23% increase. In comparison the average omission error only improved by 5% relative to the balanced approach, with a 14% jump in the average commission error.

When MIR-TH values were adjusted to reduce commission errors, the average commission error dropped to 25%. Grids 1,N1,Q1, Q2 and V1 showed commission errors below 20%. Least improvement in commission error was in grid 8 which only dropped by around 2%. The average omission error for all the grids was 59% .

4.5 Discussion

AHI-FSA provides a two-tier product for wildfire surveillance, AHI-FSA 2 km provides a hotspots detection and AHI-FSA 500 m provides fire-line pixels. AHI-FSA 2 km detections are directly comparable to VIIRS hotspots which is a thermal anomaly product. Even though the AHI-FSA 2 km detection has a ground resolution of 400 ha (2 km × 2 km), results show AHI-FSA 2 km could detect fires smaller than 14 ha (375 m × 375 m) in size. The detection probability of small fire varies between the grids. The highest detection probability was reported over grids 8 and 9 which was over 40% for a single VIIRS hotspots fire. Grids 8 and 9 falls over the North Western Australia region, with relatively low cloud cover compared to other grids. Tree cover data in

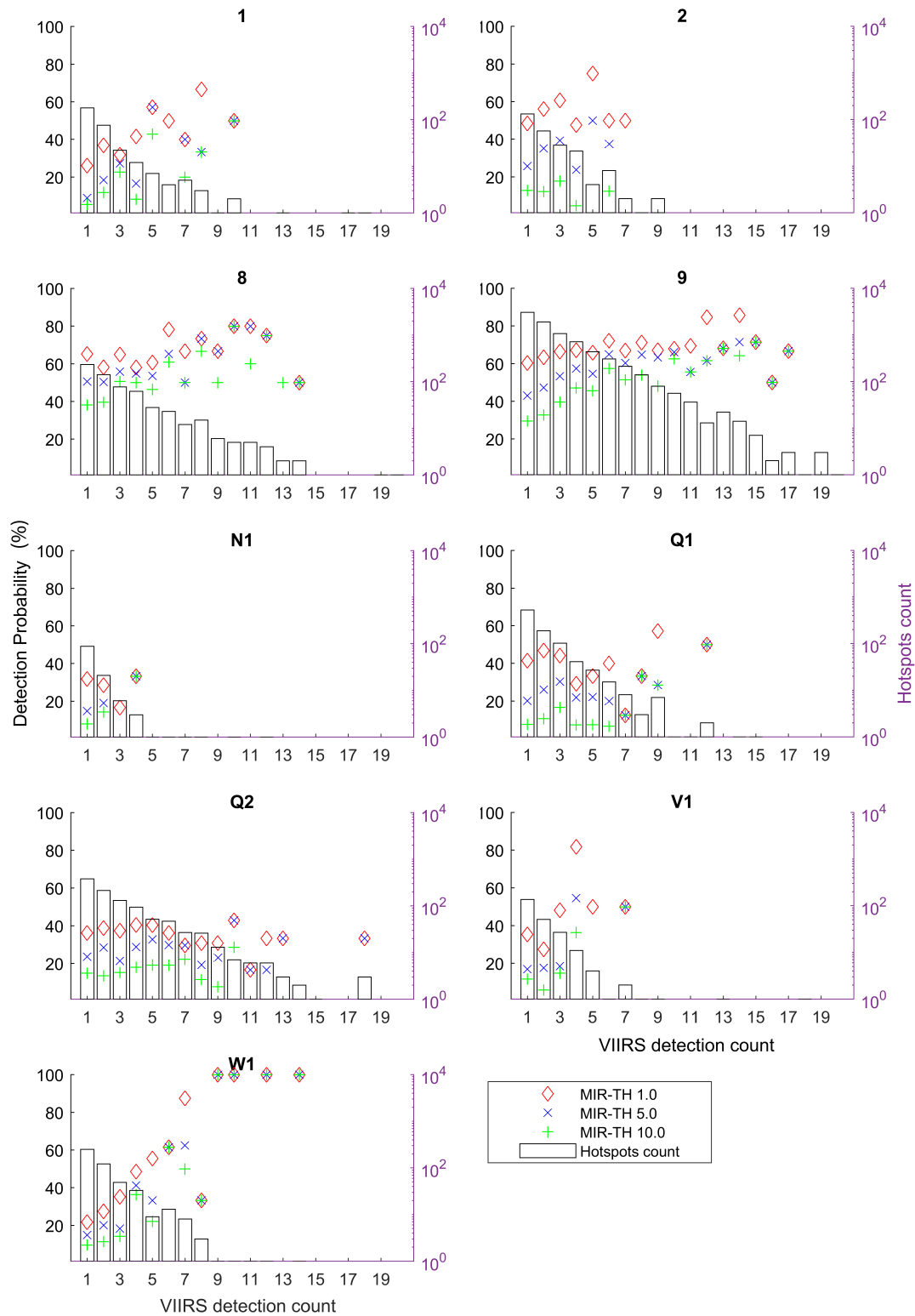


FIGURE 4.5: AHI-FSA 2 km detection probability of fires based on the number of VIIRS hotspots within the over lapping AHI MIR pixel. Detection probability is computed for three MIR-TH scenarios 1.0,5.0 and 10.0. Count of recorded number of fires for each fire class is shown by the column value in the right y-axis (on \log_2 scale) and the detection probability is shown in the left y-axis as a percentage of total hotspots in each class.

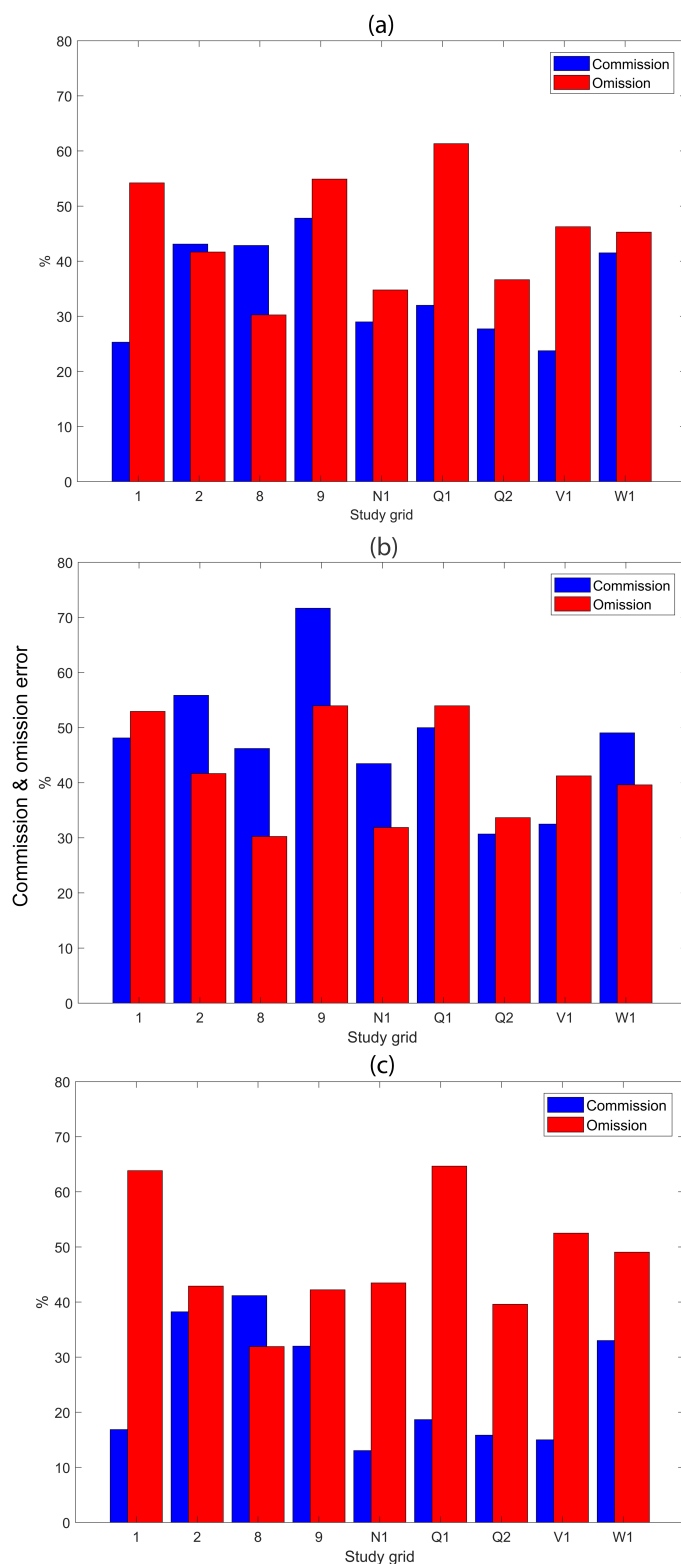


FIGURE 4.6: AHF-FSA 500 m commission and omission error are shown for compared to VIIRS cloud-free intercomparison data. (a) MIR-TH threshold values are selected to optimize AHF-FSA 500 m commission and omission error; (b) MIR-TH values are selected to minimize omission error; (c) MIR-TH values are selected to minimize commission errors.

Figure 4.2 indicates the majority of fires in this region are woodland fires. Grids Q1 and Q2 also showed relatively high detection probability of single VIIRS hotspot fires compared to other grids.

Impact of AHI 2 km cloud mask clearly visible in Table 4.2. With almost 20% of VIIRS hotspots masked out by the AHI cloud mask from the fire day cloud mask. This was also reflected in the AHI-FSA 2 km omission error calculations from the large gap between intercomparison omission error and cloud-free intercomparison omission error. Freeborn et al. (2014) also calculated 30% of the SEVIRI omission error compared to MODIS was due to SEVIRI cloud mask. Thus, by masking out VIIRS hotspots using the AHI cloud mask an accurate estimation of the AHI-FSA performance is facilitated to an extent. Impact of error inherited through the cloud mask cannot be fully eliminated due to errors in cloud mask products.

AHI-FSA 500 m is the second layer of informative data available via AHI-FSA as fire-line pixels. It is better identified as a wildfire visualisation tool as it maps the fire activity at the edge of the fire. Wickramasinghe et al. (2016) have shown how fire-line pixels maps the fire activity when monitoring the fire throughout the day. AHI-FSA 500 m depend on smoke and changes in vegetation cover to map fire-line pixels. Thus, VIIRS hotspots are not directly comparable to AHI-FSA 500 m fire-line pixels due to the differences between the products. However, this intercomparison tries to quantify the number of VIIRS hotspots that can be mapped by AHI-FSA 500 m fire-line pixels. In this study, AHI-FSA 500 m commission/omission errors were calculated for three possible scenarios based on MIR-TH value. The average AHI-FSA 2 km commission and omission errors across all grids when balanced MIR-TH values were selected was 66% and 27% respectively. AHI-FSA 500 m was able to bring down the commission error to 32% when balance MIR-TH values were used. However, the omission error was increased to 45%. When minimum commission values were selected AHI-FSA 500 m commission error dropped to 25%. AHI-FSA 500 m omission error is relatively high compared to AHI-FSA 2 km. The 7% difference in the AHI-FSA 500 m average omission error when MIR-TH values 1 and 10 were used demonstrates AHI-FSA 500 m omission error is due to lack of detectable smoke and changes in vegetation due to fire.

The two products of AHI-FSA are likely to play different roles in wildfire monitoring. For example in terms of wildfire management where early detection is of importance AHI-FSA 2 km can be utilized with high false detection. In terms of recoding wildfire activity and monitoring of large fires AHI-FSA 500 m is more suited, providing lower commission errors and higher spatial resolution.

4.6 Conclusions

In this study, we intercompare AHI-FSA against VIIRS hotspots using an annual data-set across Australia. AHI-FSA 2 km showed the capability to detect small 14 ha fires 40% of the time in North Western Australia. The need to adopt a dynamic threshold value for different regions to achieve the optimum AHI-FSA performance was also demonstrated. This threshold will also be influenced by end user requirements, for example in applications where the focus is in on early detection, a lower threshold value can be adopted.

The average omission error was only 27% balanced MIR-TH value for the study period. AHI-FSA 2km showed high commission errors of around 66% (balanced MIR-TH). In operational applications of AHI-FSA 2km this value could be reduced by using a temporal composite of AHI-FSA 2km detections to reduce false detections. AHI-FSA 500m demonstrates an, improved the commission error of 25% while at the same time improving the spatial resolution to 500m. AHI-FSA is impacted by AHI cloud mask when intercompared with VIIRS hotspots. Due to the large difference in the spatial resolution between the two products. Overall this study contributes to the evaluation of AHI-FSA algorithm over Australia for wildfire surveillance. The advantage of AHI-FSA two-tier data is demonstrated as well as the flexibility of the algorithm to be adjusted based on the end-user requirements. It is expected the results here provide direction for further improvement of the algorithm. Further evaluation of AHI-FSA 500m data must be conducted with high temporal data. Possible integration of AHI-FSA 500m for wildfire modelling to improve fire path prediction could also be investigated.

5

Implementation of a new algorithm resulting in improvements in accuracy and resolution of SEVIRI hotspot products

This chapter is based on: *Wickramasinghe, C., Wallace, L., Reinke, K. and Jones, S., 2018. Implementation of a new algorithm resulting in improvements in accuracy and resolution of SEVIRI hotspot products. Remote Sensing Letters, 9(9), pp.877-885.*

Abstract

Active wildfire detection, surveillance and mapping is an important application of satellite remote sensing. The Active Fire Monitoring (FIR) products, from the Spinning Enhanced Visible and Infrared Imager (SEVIRI) on board the Meteosat Second Generation (MSG) satellites, provide rapid-fire detection data every 5 to 15 min over the European and African continents. However, the real world application of this high temporal frequency data is hindered due to the product spatial resolution of 3×3 km, thus limiting the application in fire surveillance and mapping activities. This letter implements a modified version of the Advanced Himawari-8 Imager - Fire Surveillance Algorithm (AHI-FSA) for SEVIRI with the aim of improving the spatial resolution of fire activity mapping. Initial results demonstrate the algorithm was able to improve the resolution of fire detection from 3×3 km to 1×1 km and simultaneously reduce the commission and omission errors by 25 % and 16 % respectively.

5.1 Introduction

The launch of a new generation of geostationary satellites, covering most areas of the globe has seen a rapid uptake of this data as a source for wildfire detection and monitoring applications. Sensors on satellites, such as the European Meteosat Second Generation (MSG)(Calle et al., 2008), Geostationary Environmental Operational Satellite (GEOS)(Schroeder et al., 2008a) and the Japanese Himawari-8 satellite(Wickramasinghe et al., 2016), offer large area coverage at high temporal resolution allowing fires to be detected earlier than possible with Low Earth Orbiting satellites (LEO). Nevertheless, in comparison to LEO satellites, such as MODIS (Moderate Resolution Imaging Spectroradiometer)(Justice et al., 2002b) and VIIRS (Visible Infrared Imaging Radiometer Suite)(Schroeder et al., 2014), the spatial resolution of detection is significantly coarser. The MSG fire product, Active Fire Monitoring (FIR)(Tekeli et al., 2009), has a spatial resolution of 3×3 km. This coarse resolution limits the practical application of the high temporal resolution data available. Prins et al. (1998) have shown in their study that GEOS (4×4 km ground resolution Middle Infrared (MIR) channel) can detect fires as small as 0.5 ha at 759 K. Thus subpixel fires can be detected, but the usefulness is limited by being unable to locate the fire within the coarse resolution pixel. In the case of SEVIRI, it is reported 1 ha fires at 600 K can be detected (Calle et al., 2006a). This would mean a fire size of 1 ha could be anywhere within an area of 900 ha (3×3 km).

5.1.1 The AHI-Fire Surveillance Algorithm(AHI-FSA)

The AHI-Fire Surveillance Algorithm (AHI-FSA) is a newly developed algorithm designed for wildfire mapping using the Himawari-8 satellite (Wickramasinghe et al., 2016). Himawari-8 based fire detections using existing algorithms are limited to a 2×2 km ground resolution due to the spatial resolution of the MIR channel. To

overcome this limitation, AHI-FSA utilizes a multi-temporal and multi-band approach to improve the spatial resolution of fire surveillance to 0.5 km. This method takes advantage of the higher resolution Near Infrared (NIR) and Red channels, at 1 km and 0.5 km respectively. At present, the AHI-FSA algorithm has been tested on case study fires in environments with low relief and canopy cover in Western/Northern Australia. Initial results from that study demonstrate low omission (2%) and commission (7%) rates against LEO fire products with 0.5 km spatial resolution.

5.1.2 Objectives

In this study of a wildfire in Portugal on the 8th of August 2016, we implement a modified version of the AHI-FSA algorithm for SEVIRI (Spinning Enhanced Visible and Infrared Imager) to improve the spatial resolution of SEVIRI fire products. The new outputs are then compared with SEVIRI FIR (Active Fire Monitoring) products, and both products intercompared with MODIS hotspots and Landsat-8 burnt areas detections within the case study area.

5.2 SEVIRI Active Fire Monitoring (FIR)

Spinning Enhanced Visible and Infrared Imager has 11 spectral channels at 3×3 km spatial resolution. This includes three visible channels (0.75, 0.63, and 0.81 μm), one short-wave infrared (1.6 μm), and eight infrared channels (3.9, 6.2, 7.3, 8.7, 9.7, 10.8, 12.0, and 13.4 μm). SEVIRI also has a High-Resolution Visible (HRV) channel with a 1×1 km resolution (Roberts et al., 2005). Currently, Active Fire Monitoring (FIR) products are available through the EUMETSAT (European Organisation for the Exploitation of Meteorological Satellites) website (<https://www.eumetsat.int>). FIR fire products are based on detecting the radiation difference in the 3.9 μm and 10.8 μm channels (Tekeli et al., 2009; Amraoui et al., 2010). FIR uses four threshold condition values to detect fires using 3.9 μm and 10.8 μm channels (Tekeli et al., 2009). Validation of FIR products by Calle et al. (2008) and Stoyanova et al. (2008) has shown FIR is reliable at a continental scale or over large areas. For example, FIR has shown a correlation value of 0.79 compared to MODIS when using 40×40 km grid area (Calle et al., 2008). However, a FIR product validation over Turkey showed that only 15.6% of reported fires were detected accurately (Tekeli et al., 2009).

5.3 SEVIRI-FSA

In this study, the AHI-FSA algorithm was modified to work with the available spectral channels and spatial resolutions of the SEVIRI instrument. The modified AHI-FSA algorithm is referenced henceforth as the SEVIRI-FSA algorithm. In comparison, both AHI and SEVIRI sensors have a 3.9 μm MIR channel, with the AHI MIR channel having a higher spatial (2×2 km) and radiometric resolution of 14 bits, compared to (3

$\times 3$ km) and 10 bits on SEVIRI. The central wavelength of the defined NIR channel for the two sensors is different, as shown in Table 5.1. The SEVIRI HRV channel has the highest spatial resolution (1×1 km) with a wide bandwidth ranging from 0.4 to 0.8 μm . Due to its higher resolution, the SEVIRI HRV channel was selected as comparable to the AHI RED channel instead of SEVIRI RED channel. This was also deemed an appropriate substitution as the required response to smoke in the RED channel will be similar across the visible spectrum.

TABLE 5.1: AHI and SEVIRI channel comparison.

Channel	AHI		SEVIRI	
	Central wave length (μm)	Resolution (km)	Central wave length (μm)	Resolution (km)
MIR	3.88	2	3.90	3
NIR	0.85	1	1.64	3
RED/HRV	0.64	0.5	0.4-0.8	1

The direct implementation of AHI-FSA for SEVIRI was not possible mainly due to the fact that the spatial resolution of the SEVIRI NIR channel is the same as its MIR channel. AHI-FSA uses the 1×1 km AHI NIR channel to detect sub-pixel changes in vegetation cover due to fire within the 2×2 km AHI MIR pixel. Although the SEVIRI NIR channel likely demonstrates a similar response, no spatial resolution gains are achieved over the SEVIRI MIR channel. As the MIR channel is expected to be a more reliable indicator of fire, the SEVIRI-FSA (modified AHI-FSA algorithm for SEVIRI) algorithm was limited to, MIR condition and the RED condition in the original AHI-FSA algorithm. No other changes were made to the algorithm. The algorithm requires a non-fire day image to calculate the thermal changes in the MIR due to fire, and the RED channel reflectance changes due to smoke. A non-fire day image is a composite of the eight days preceding the day of the fire. In the current case study the non fire day image was initialized using MODIS hotspot products to identify non-fire days prior to the study period. Fire day imagery is from the day of the fire. Wickramasinghe et al. (2016) provides a detailed description of the following two conditions.

MIR Condition: The MIR band is used to detect thermal anomalies using a contextual threshold. A fire day and a non-fire day MIR band imagery are taken to calculate the radiance difference. A dynamic contextual threshold is then applied to the MIR difference image to detect thermal anomalies. If f in equation 5.1 is equal or greater than 1, the pixel is flagged as a possible fire pixel.

$$f = \Delta M - [\mu_{\Delta M_{bp}} + 0.5 \times \sigma_{\Delta M_{bp}}] \quad (5.1)$$

where ΔM is the MIR radiance differences of the target pixel between a fire day and a non fire day pixels with similar time stamp for the target pixel, $\mu_{\Delta M_{bp}}$ and $\sigma_{\Delta M_{bp}}$ are the mean and standard deviation of the

MIR radiance difference of all background pixels in the kernel. Initially, a 3×3 pixel kernel is used, which is incrementally expanded up to a 15×15 pixel kernel stopping when 65% of pixels are non-fire, non-cloud and non-water pixels.

RED Condition: In this condition, reflectance differences between a fire day and a non-fire day are calculated for the red channel. A high pass filter is then applied to amplify variations in reflectance. Sobel edge detection is used to determine the boundaries between smoking and burnt/burning areas. Those pixels that fall within the flagged MIR pixels are identified as SEVIRI-FSA hotspots.

$$\begin{aligned}\Delta R_{hp} &= \text{high_pass_filter}(\Delta R) \\ R_{edge} &= \text{edge}(\Delta R_{hp})\end{aligned}\tag{5.2}$$

where (ΔR) is difference in the red reflectance between fire and non-fire day imagery.

5.4 Intercomparison

The objective of this study was to enhance the fire surveillance and mapping potential of SEVIRI using a modified version of the AHI-FSA algorithm. Studies validating satellite active fire products have shown that good practice is to conduct an intercomparison using higher resolution products that have themselves been validated (Schroeder et al., 2008a; Ichoku et al., 2003; Koltunov et al., 2012; Freeborn et al., 2014; Calle et al., 2006a). MODIS MOD14 and MYD14 hotspots products are 1×1 km products, both widely used operationally for wildfire detection, and provide suitable data for this study. Validation and intercomparison of fire hotspot products require calculating the commission and omission errors. Differences in resolution make it difficult to compare the two products directly spatially. Therefore, in this study, omission error was computed using the euclidean distance between the MODIS hotspots (true hotspots) and the SEVIRI derived fire products. A detection was counted as a false detection if the distance was greater than 3 km (this is rounded up from 2.8 km which is the maximum possible distance between a SEVIRI pixel centre and MODIS pixel centre when the two pixels are adjacent) (Wickramasinghe et al., 2016). Commission error, on the other hand, was calculated using the burn scar data derived from a Landsat-8 post fire image. A Landsat-8 post fire image captured on 15th August 2016 was manually digitized to map burnt extent. Existing burn scar products, depends on semi-automated change detection techniques to identify sudden changes in landcover, which can introduce errors due to cloud and smoke cover (Goodwin & Collett, 2014), thus manual digitization technique was used to map the burn scars. Further more due to the 16-day revisit period manually identifying the burn area ensured, only burn scars during the study period was mapped.

Again, as with the omission error calculation, a 3 km buffering distance from the pixel centre point was used. Detection within the buffer was counted as a true detection. The 3 km buffer was chosen to account for single pixel geo-locational error.

5.5 Case Study

A large fire complex in Portugal surrounding the city of Coimbra in August 2016 was recorded as the worst fire in recent years with over 116 000 ha of forest destroyed. This made for an ideal case study due to the large number of active fire fronts and hotspots. The study area was selected and covered two Landsat-8 scenes (path 204 and rows 31 & 32) (Figure 5.1). The fire day for the case study was selected as 8th of August. MODIS MOD14A1 and MYD14A1 products were available at 10:30 UTC and 13:55 UTC respectively. SEVIRI FIR data was available as 30 minute composites reported over a 15 minutes moving window. For example all detections from 00:00-00:30 UTC are compiled as a single detection followed by a second data-set which is compiled from detections from 00:15-00:45. For the study, we used FIR 10:15-10:45 and FIR 13:45-13:45 data-sets to coincide with MODIS Aqua and Terra detections. To map the burn scars, Landsat-8 imagery captured on the 15th of August 2016 was manually digitized with Landsat-8 imagery from 14 July 2016 (pre fire day) used as reference to identify the burnt area.

5.6 Results and Discussion

In this study, we compare three active fire hotspot products; MODIS hotspots (1×1 km), SEVIRI FIR (3×3 km) and SEVIRI-FSA (1×1 km). All products are validated using the pixel centre point. Figure 5.2 shows two maps comparing the detections of three products at MODIS Terra and Aqua overpasses. Landsat-8 post fire image is used as the background to show the burn scars from the fires (dark brown patches). Fire activity appears very minimal in both MODIS and SEVIRI-FSA, both showing a small number of detections. The SEVIRI-FSA detections show an improved agreement with the MODIS hotspots and Landsat-8 burn scars compared to the SEVIRI FIR hotspots. Both figure 5.2 (a) and (b) shows FIR overestimates the fire area, whereas most of the SEVIRI-FSA detections fall well within the burn area and close to MODIS detections. This is further demonstrated in Figure 5.3 which shows 71 % of SEVIRI-FSA detections fall directly within the Landsat-8 burnt area, while 96.4 % fall within the 3 km buffered area. In comparison, only 55 % of FIR detections fell directly within a Landsat-8 burnt area and 69 % in the buffered area. In 5.2 the first SEVIRI-FSA column ranges from 0 to 700 m which is the diagonal distance from the centre point of the pixel to the corner of the pixel (700 m for 1×1 km pixel). If the burnt area intersects the 700 m buffer, the detection is counted as a true detection. Similarly, a 0 to 2.2 km buffer was used for FIR products. Figure 5.2(b) also shows that SEVIRI-FSA is capable of detecting small fires. For example, small fires along the river on the north boundary of the image are detected by SEVIRI-FSA. Single MODIS hotspots in the east-south-east corner of figure 5.2(b) was also detected by SEVIRI-FSA.

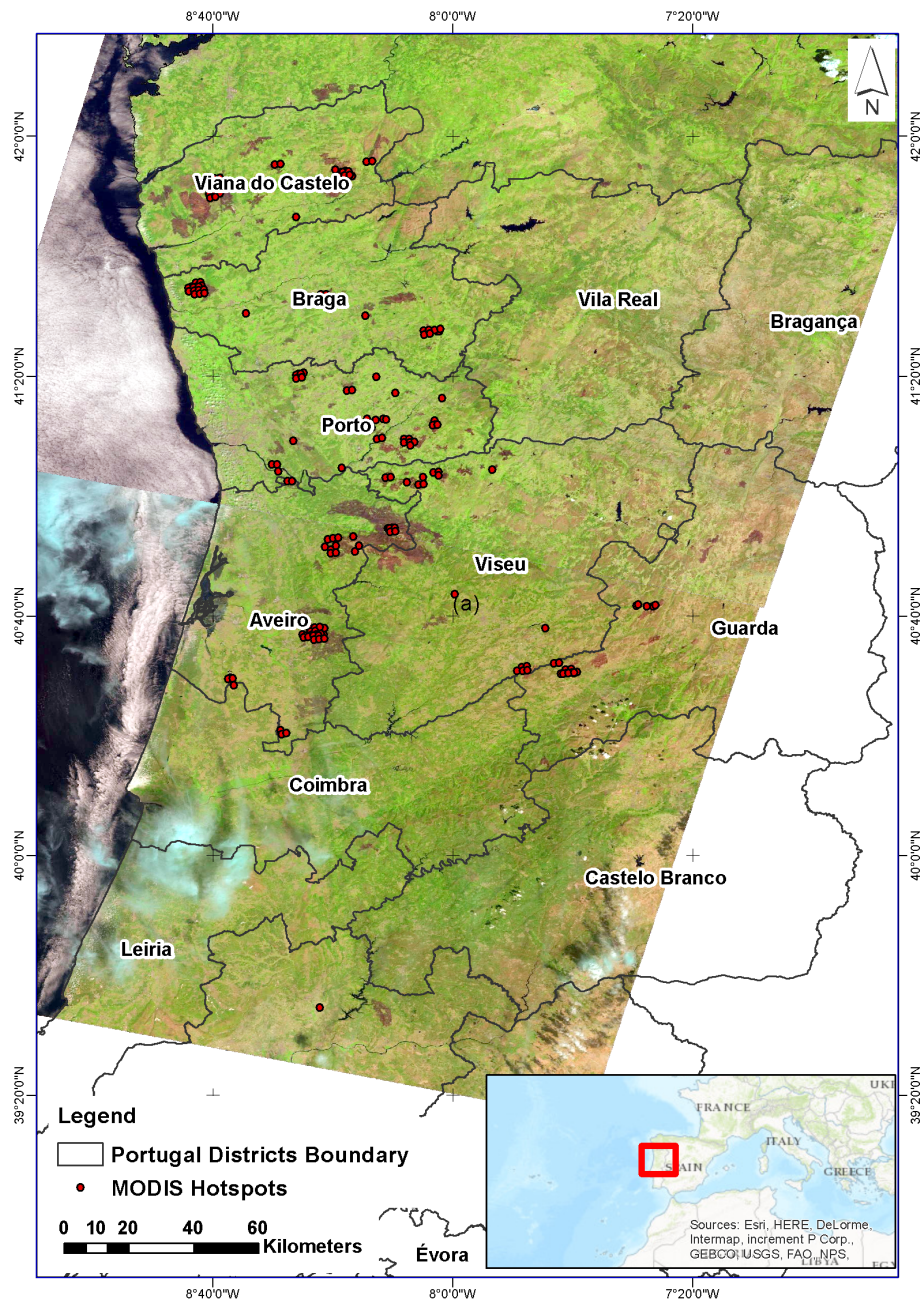


FIGURE 5.1: The study area covering two Landsat scenes path-204 row-31 and row-31 are shown. Background Landsat true colour imagery captured on 15th August 2016 shows the burnt area. MODIS MYD14A1(13:55 UTC) hotspots are also overlaid on top.

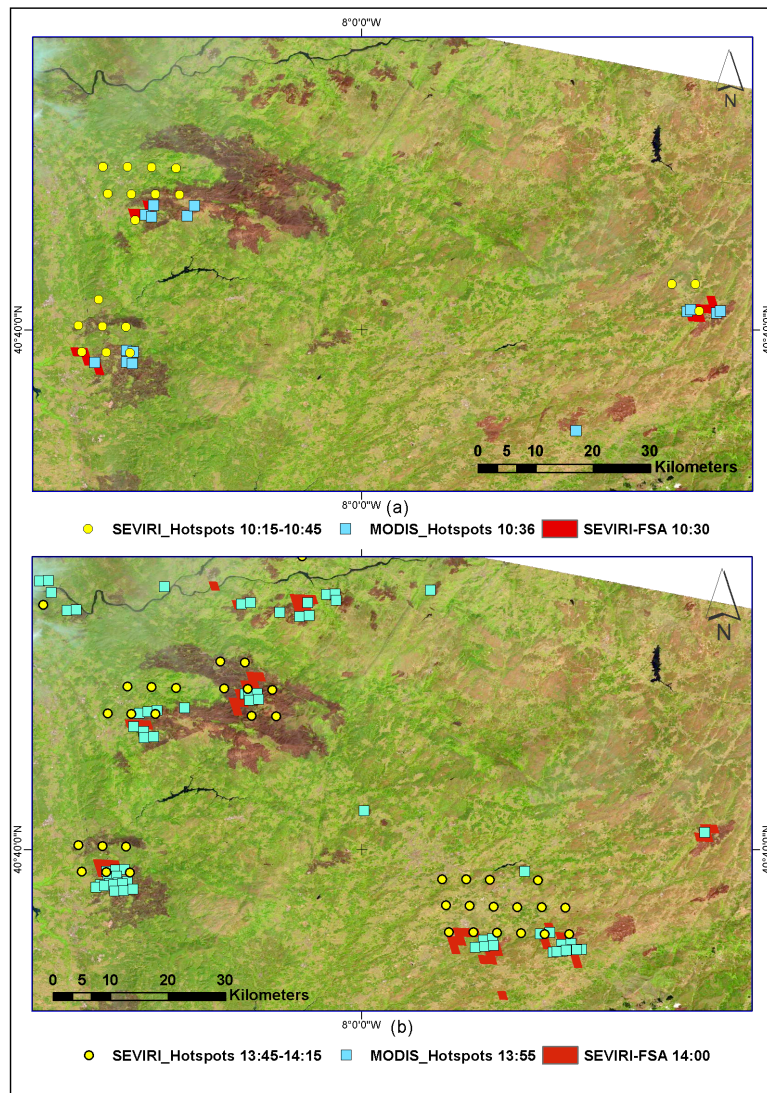


FIGURE 5.2: SEVIR-FSA, FIR and MODIS hotspots detected at 10:30 UTC (a) and 13:55 UTC.

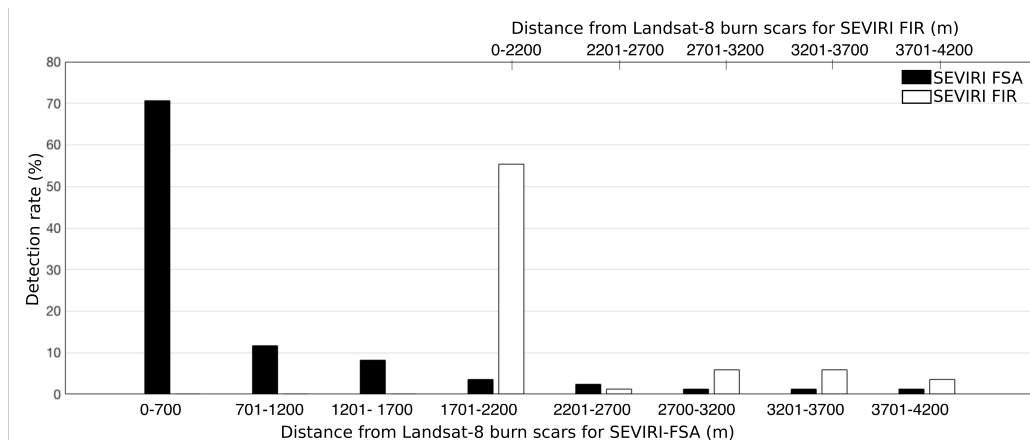


FIGURE 5.3: SEVIRI-FSA and SEVIRI-FIR detection as a percentage of the total detections and distance to Landsat-8 burn scars. Where distance categories are based on the maximum distance along the diagonal from the sensor pixel center.

Figure 5.4 shows the percentage of detections grouped by distance from the nearest MODIS hotspot. Approximately 11% of SEVIRI-FSA detections are within 500m of a MODIS hotspot and 53% are within 1500m of a MODIS detection. This is a considerable improvement compared to 5% and 14% for the FIR product over the same distances. As described above, omission error was calculated based on MODIS detections whereas commission error was calculated by comparison to Landsat-8 burn scars. Table 5.2 provides a summary of the total number of detections, and omission and commission error calculations. This demonstrates that the SEVIRI-FSA is capable of improving the SEVIRI active fire mapping product compared to the existing FIR product lowering omission error by 16% and commission error by almost 25%.

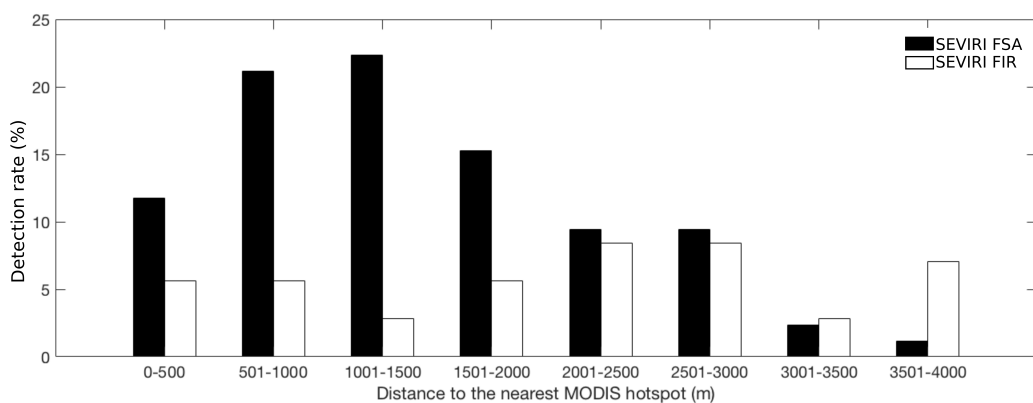


FIGURE 5.4: SEVIRI-FSA and SEVIRI-FIR detection as a percentage of the total detections and distance to the nearest MODIS hotspots.

TABLE 5.2: The Omission and Commission rates of the FIR and FSA algorithm. Omission error is calculated against MODIS hotspots, while commission is calculated against Landsat-8 burnscars.

Products	Total no. of detections	Omission Error(%)	Commission Error(%)
MODIS	143	–	–
SEVIRI FIR	71	53.1	31.0
SEVIRI FSA	85	37.7	3.6

5.7 Conclusion

Geostationary satellite-based active fire mapping is an important tool in wildfire surveillance and management activities due to the high temporal resolution offered. However, the low spatial resolution of products has limited their practical application as a fire surveillance tool (even though the fire detection algorithms can detect sub-pixel level fires, the location of the fire is limited by the coarse sensor resolution). The AHI-FSA algorithm developed for Himawari-8 active fire mapping and surveillance uses a multi-temporal and multi-resolution approach to improve the detection from 2 km to 0.5 km. In this case study fire, the AHI-FSA algorithm was modified for use with SEVIRI. SEVIRI-FSA demonstrated 3.6 % commission error and 37.7 % omission error. This is a 25 % and 16 % improvement over the existing FIR product for the case study fires. Results have also shown the SEVIRI-FSA detections have a higher spatial agreement with MODIS hotspots compared to FIR products. We demonstrate 53 % of SEVIRI-FSA detections fall within 1.5 km of MODIS detection which is around four times greater than FIR detections (14 %). Furthermore, around 70 % of SEVIRI-FSA detections were within the Landsat-8 burn scars. In contrast, only 55 % of FIR products were within the Landsat-8 burn scars. This case study has demonstrated the multi-resolution, and multi-temporal approach used by FSA was able to improve the fire surveillance ground resolution by a factor of three, overall significantly improving the commission and omission error. Results from SEVIRI-FSA also demonstrated good fire location agreement when compared to MODIS hotspots. These achievements suggest that fire detections from the SEVIRI sensor can be significantly improved with the SEVIRI-FSA algorithm.

6

Conclusion

Sensors on board geostationary earth observation satellites provide high temporal observations. However, the coarse spatial resolution of these sensors limits their application for wildfire surveillance. This research explores the possibility of improving wildfire surveillance capabilities of geostationary earth observations sensors using a new multi-resolution and multi-temporal approach. As a result, the Fire Surveillance Algorithm (FSA) was developed for the Advance Himawari Imager (AHI) on board the Himawari-8 satellite. The algorithm uses a multi-resolution and multi-temporal approach to provide multi-level wildfire surveillance information. Providing two products, a $2\text{ km}\times 2\text{ km}$ thermal hotspot detection and $500\text{ m}\times 500\text{ m}$ fire-line pixel detection. Even though the algorithm was initially developed for the AHI sensor, a modified version of the algorithm, SEVIRI-FSA, was developed and tested on the SEVIRI sensor on board the European MSG satellite. SEVIRI-FSA is capable of 1 km fire-line pixels, with improved location accuracy compared to the currently operational thermal anomaly product, demonstrating the cross-platform application of the algorithm on geostationary satellite sensors with similar spectral bands. The new algorithm was validated using a suite of evaluation methods. These evaluations raised new challenges in the intercomparison of high-frequency wildfire surveillance data and required a new validation method to be developed (Chapter 3). The AHI-FSA algorithm demonstrated an overall performance comparable to that of medium resolution LEO

hotspots products with the additional advantage of high temporal frequency.

6.1 Algorithm development

RQ 1: How can the attributes of geostationary satellites be combined to create a new algorithm to provide improved wildfire surveillance?

The successful utilisation of the Himawari-8 AHI 500 m RED and 1 km NIR channels has been fundamental to the improved wildfire surveillance capabilities achieved through the AHI-FSA. Implementation of an existing thermal anomaly detection algorithm to the Himawari-8 AHI sensor data would only be able to detect thermal hotspots at a 2 km spatial resolution, whereas, the AHI-FSA uses a multi-resolution and multi-temporal approach, providing two levels of wildfire surveillance data. AHI-FSA 2 km detects thermal anomaly hotspots and AHI-FSA 500 m maps fire-line pixels. AHI-FSA 2 km uses a contextual based approach to detect increases in thermal radiance using the MIR channel. The location of the sub-pixel fire within the 2×2 km MIR pixel is then identified by taking advantage of the higher resolution RED and NIR channels, and mapped as fire-line pixels. "Fire-line pixel" is a new term developed to better describe the nature of the AHI-FSA 500 m product, as it is a continuous series of 500 m pixels representing the active fire line within the 2 km MIR pixel.

6.2 Algorithm evaluation

RQ 2: What are the best methods for evaluating the performance of geostationary based wildfire surveillance algorithms?

Ground truthing geostationary satellite-based wildfire surveillance algorithms, such as the AHI-FSA, is challenging due to the difficulty in collecting synchronous high-frequency ground truth data across a large area. Evaluating AHI-FSA is then a challenge. Firstly, the high-resolution temporal data available through AHI have no direct comparable equivalent and secondly the AHI-FSA 500 m fire-line pixel is a new product that is not directly comparable to existing thermal hotspot products or burned area products available through LEO satellites. The majority of the satellite-based wildfire detection algorithm validation studies have adopted an intercomparison approach with a higher resolution satellite-based product as the means of validation. In this study, a number of techniques were used to intercompare AHI-FSA and SEVIRI-FSA with LEO thermal anomaly products as well as burn scars. It was demonstrated that by directly intercomparing the geostationary wildfire detection product to LEO hotspot products the presumed advantage of the high temporal-frequency is not evaluated. This was more prominent for AHI-FSA 500 m which depends on the smoke and the burning of vegetation from the fires for attribution. Based on this study, it is fair to say there is no single method for intercomparing geostationary and LEO wildfire detection products. It is suggested

at least three techniques must be used to evaluate the performance of geostationary wildfire surveillance products when intercomparing with LEO hotspots. 1) Minimum detectable fire size, this quantifies the detectable minimum thermal variation by the algorithm and also provides an approximate estimation of sub-pixel fire size of a single hotspot detection and the likelihood of a detection. 2) Commission and omission error calculation. This provides an estimation of the confidence factor in the detection. 3) Estimating the average fire detection time compared to LEO detections, this is useful information when the algorithm is used operationally with LEO products for wildfire surveillance.

***RQ 3:** What is the performance of the new algorithm intercompared with standard satellite fire products across selected fire-prone landscapes?*

AHI-FSA was intercompared against LEO hotspot products, and Landsat-8 burn scars using case study fires as well as an annual data-set across nine study grids covering an area of 3 600 000 km². Initially, case study fires over the northern grassland/woodlands of Australia were used for the intercomparison. The selection of the Northern Region of Australia for the initial evaluation of the algorithm was influenced by the existing literature that has focused on this region for validation of LEO thermal hotspots products. The relatively higher instance of wildfire activity in this region was also an important factor. AHI-FSA was able to detect single VIIRS hotspot fires, 40 % of the time over northern Australian woodland. AHI-FSA 2 km reported an average omission error of 27 % when intercompared with near-synchronous VIIRS hotspots over the whole of Australia. In northern Australia, AHI-FSA reported the early detection of fires up to three hours before LEO overpass. Furthermore, in comparison to MODIS, we also measured a 73 % chance of AHI-FSA detecting fire activity at the location of the MODIS hotspot before the MODIS overpass.

Analyses of these case study fires have also demonstrated the improved fire surveillance capabilities of AHI-FSA 500 m fire-line pixels. AHI-FSA 500 m can continuously track fire movement at 10 minute intervals, which could be used to derive fire behaviour information such as heading and speed. AHI-FSA 500 m demonstrated 25 % commission error Australia wide intercompared to VIIRS hotspots. Over northern Australia, this figure was 7 % intercompared to Landsat-8 burnt scars. AHI-FSA 500 m tends to have high omission error when compared to near synchronous LEO hotspots. However, when the daily comparison was used AHI-FSA 500 m reported a low 7 % omission error compared to MODIS hotspots in northern Australia. By taking a daily composite when comparing AHI-FSA 500 m with MODIS hotspots the temporal advantage of AHI-FSA is also taken into account.

6.3 Algorithm Versatility

***RQ 4:** Can the new algorithm be applied to other geostationary sensors?*

The AHI-FSA algorithm takes advantage of a common attribute of geostationary earth observation satellites; having a relatively higher spatial resolution in the visible channel compared to the MIR channel. Thus there is the potential for the algorithm to be implemented in other geostationary satellites. SEVIRI-FSA

algorithm used a modified version of AHI-FSA algorithm. The SEVIRI-FSA uses the MIR channel and the High-Resolution Visible (HRV) channel to provide 1 km fire-line pixels. The SEVIRI-FSA reported 28 % and 16 % improvement in commission and omission errors respectively over the existing FIR product in the case study fires over Portugal. The SEVIRI-FSA also demonstrated higher spatial agreement with MODIS hotspots compared to FIR hotspots. Furthermore, around 70 % of SEVIRI-FSA detections were within the Landsat-8 burn scars, thus demonstrating the platform-independence of the new algorithm developed in this study.

6.4 Synthesis

Increasing global temperature and longer periods of drought have seen an increase in wildfire activity across the globe Bowman et al. (2009). Wildfire season has extended with more frequent large fires that are becoming difficult to manage. Population increase has also led to more and more people becoming exposed to wildfire Jolly et al. (2015). Satellite-based wildfire surveillance plays a key part in large-scale wildfire monitoring and early detection. In Australia, the Sentinel Hotspots program provides a national-level bushfire monitoring system using MODIS, VIIRS and AVHRR derived products. The system allows emergency service managers across Australia to identify fire locations with a potential risk to communities and properties. Due to the dependence on LEO satellite-based sensors, the daily combined coverage over an area is limited to six to seven observations per day. A geostationary satellite-based system, on the other hand, can provide high temporal frequency observations ideal for wildfire surveillance. However, using existing fire detection algorithms developed for LEO satellites have limited their applications in wildfire surveillance due to the dependence on coarse ground sampling thermal channels on the geostationary sensors. The key challenge then is how to maximise the information retrievable from these high temporal datasets whilst at the same time managing for the reduced spatial resolution. This research aimed to address this issue through a novel multi-spatial resolution and multi-temporal approach that took advantage of attributes of geostationary sensors. The new algorithm enables geostationary sensor derived products to achieve spatial resolutions comparable to that of LEO hotspot products by taking advantage of the higher resolution RED and NIR channels to locate the sub-pixel fire within the larger MIR pixel. Implementation of the new algorithm on the AHI data from the Himawari-8 satellite demonstrated that it was able to provide wildfire mapping at 500 m spatial resolution. This is a considerable improvement compared to the 2 km that is achievable from existing fire detection algorithms. Compared to the LEO satellite-based hotspots products used in the Sentinel Hotspots program AHI-FSA 500 m sits in between the 1 km MODIS hotspots and 357 m VIIRS hotspots. This provides an ideal data-set to fill in the data gaps between the MODIS and VIIRS overpasses in the Sentinel Hotspots program. It can also facilitate near real-time wildfire surveillance, maximising the use of high-frequency observations available from geostationary satellites. The new algorithm is also platform independent as demonstrated through the implementation of SEVIRI-FSA algorithm on the European SEVIRI

sensor on board the MSG satellites. The SEVIRI-FSA demonstrated improvements in spatial resolution as well as in fire location accuracy compared to the existing FIR product. The next step would be to test the algorithm on the Advanced Baseline Imager (ABI) sensor onboard the new GOES-R series of satellites over North and South America. ABI has similar attributes to that of AHI, with a 500 m visible channel and 1 km NIR channel. The AHI-FSA algorithm could directly be implemented on the ABI sensor with a potential performance equivalent to the AHI-FSA. Implementation of the algorithm on the three main geostationary satellites Himawari-8, GOES-R and MSG could provide near-real-time wildfire surveillance covering all fire-prone continents. The system would be able to provide 500 m wildfire surveillance over North America, South America, Asia and Australia and 1 km wildfire surveillance over Europe and Africa during the daytime. Validation of high-frequency wildfire detections from geostationary satellite products has not been clearly documented in the literature, with the majority of studies using simple intercomparison with LEO products to assess the performance of their geostationary equivalents. These approaches overlook the advantage of high temporal data available via geostationary satellites and this needs to be taken into account when intercomparing with LEO hotspots. This study presents an optimum method for evaluating the high temporal frequency wildfire surveillance hotspots products intercompared with LEO hotspots products. A three-step process is put forward in this study that provides a quantitative performance matrix. The resulting matrix takes into account the high temporal data available via geostationary satellites and also provides information on how the geostationary wildfire surveillance algorithm could complement the existing LEO hotspot products. The new algorithm developed in this study has demonstrated a performance that is comparable to that of existing LEO hotspots products. It is known that the presence of cloud cover can have an effect on the performance of fire detection and mapping algorithms Schroeder et al. (2015); Kaufman et al. (1997). Whilst it was beyond the scope of this study to assess cloud mask accuracy and the impact on algorithm performance, therefore, this is an area for further research. A cloud mask product that overestimates the presence of cloud can reduce the number of valid pixels thereby causing the contextual threshold conditions to fail. Whereas an underestimated cloud mask causes lower background temperature estimations, which could increase the number of false detections. Therefore, a detailed analysis into the impact of cloud masking on the algorithm performance must be investigated. The balance between acceptable cloud cover percentage within the 2×2 km MIR pixel and the performance of the algorithm must also be investigated.

Smoke is an important part in the AHI-FSA algorithm, whilst radiance changes due to smoke is used to detect the fire-line pixels, the performance impact of smoke in the NIR and MIR channels needs to be investigated. Smoke is highly affected by changing wind conditions, which in turn impacts the performance of AHI-FSA. For example, changes in wind direction pushing wind back over the burnt area, could cause the NIR condition to fail in detecting change in vegetation cover due to the fires (section: 2.2.4) and the RED condition could fail to detect the edge between smoke/brunt area (section: 2.2.5) as the smoke is over the bunt area, thus impact of smoke and wind changes on AHI-FSA performance must be further investigated.

Radiative transfer modelling could potential be used to ascertain effect of smoke on these bands, allowing it to be better considered within the algorithm.

Tree canopy cover is another important factor in detecting fires, a recent study by Roberts et al. (2018) demonstrated that the FRP(Fire Radiative Power) from a fire reduces by 20% when the LAI(Leaf Area Index) exceeds 1.0. The AHI-FSA evaluation across Australia, completed in this research, also demonstrated the need for AHI-FSA to have varying threshold values in the MIR for optimum performance across different landscapes. Thus there is the possibility of using LAI mapping to enable dynamic MIR thresholds in the algorithm. This could improve the commission error across different landscapes. Furthermore, full disk wide implementation of the algorithm could also be achieved without having to test for optimum threshold values in each landscape. Existing thermal anomaly detection algorithms such as the MODIS thermal hotspots algorithm are based on a bi-spectral method, using both the MIR and TIR channels Kaufman et al. (1998); Giglio et al. (1999). In contrast, the AHI-FSA uses only the MIR channel due to the high radiance in the MIR wavelength range compared to the TIR by a grey body Wooster et al. (2005). However, the bi-spectral approach can reduce false detections compared to using a single channel Karam et al. (1995); Giglio et al. (1999). Even though AHI-FSA 500 m uses the NIR and RED channels to reduce false detections, adopting a bi-spectral method could also reduce 2 km false detections. It could also be possible to improve the commission error by creating a 30min/60min temporal composite of the AHI-FSA 2 km detections. This has the potential to minimise the number of false detections due to moving cloud. Therefore further investigation must be conducted to identify the optimum number of composite images that will provide improved commission error with minimum impact on the early detection capabilities. The AHI-FSA uses a composite image to estimate the background temperature, whereas existing thermal anomaly detection algorithms rely only on the fire day image Giglio et al. (2016). A detailed intercomparison of the two methods should be conducted to quantify the pros and cons of using the composite image for background temperature estimation compared to using only the fire day image.

The new algorithm also has the potential to be used for burnt area mapping, as the AHI-FSA 500 m fire-line pixels provide information by mapping the fire at the transition stage from burning to burnt. Furthermore, the AHI-FSA 500 m is looking at changes in vegetation cover and smoke due to the fire. Thus, fire-line pixels can be considered as burnt pixels after a period of time, providing a comparable spatial resolution to MODIS burn scar products with the advantage of high-frequency data, which will potentially minimise the false negatives due to cloud cover in the pre and post-fire imagery in the MODIS burn scare algorithm. AHI-FSA 500 m, high temporal edge detection can be used to track the fires through time, for near-real time fire monitoring and fire severity mapping. Duration of a fire at a particular location is a key parameter in fire severity mapping. AHI-FSA 500 m could be used to derive the duration of the fire at a particular location by counting the repeated AHI-FSA 500 m detections at a specific location. However, further test must be conducted using higher temporal ground based observations and aerial imagery to quantify the fire tracking potential of the algorithm. Finally, there is also the need to quantify the performance of the AHI-FSA 2 km

during the night time which was not examined in this study. Geostationary earth observations sensors are likely to improve spatial resolution in the future with visible channels having higher resolution compared to the thermal channels. Thus the AHI-FSA is likely to continue to improve the wildfire surveillance capabilities of geostationary earth observation sensors.

References

- Agresti, A. (1990). Models for matched pairs. *Categorical Data Analysis, Second Edition*, (pp. 409–454).
- Agresti, A. (2003). *Categorical data analysis* volume 482. John Wiley & Sons.
- Amraoui, M., DaCamara, C. C., & Pereira, J. M. C. (2010). Detection and monitoring of African vegetation fires using MSG-SEVIRI imagery. *Remote Sensing of Environment*, *114*, 1038–1052.
- Bessho, K., Date, K., Hayashi, M., Ikeda, A., Imai, T., Inoue, H., Kumagai, Y., Miyakawa, T., Murata, H., Ohno, T., Okuyama, A., Oyama, R., Sasaki, Y., Shimazu, Y., Shimoji, K., Sumida, Y., Suzuki, M., Taniguchi, H., Tsuchiyama, H., Uesawa, D., Yokota, H., & Yoshida, R. (2016). An Introduction to Himawari-8/9 New-Generation Geostationary Meteorological Satellites. *Journal of the Meteorological Society of Japan. Ser. II*, *94*, 151–183.
- Booth, T. H. (2009). *Bushfires in Australia Prepared for the 2009 Senate Inquiry into Bushfires in Australia*. Technical Report Commonwealth Scientific and Industrial Research Organisation, Australia.
- Bowman, D. M. J. S., Balch, J. K., Artaxo, P., Bond, W. J., Carlson, J. M., Cochrane, M. A., D'Antonio, C. M., DeFries, R. S., Doyle, J. C., Harrison, S. P., & Others (2009). Fire in the Earth system. *science*, *324*, 481–484.
- Bureau of Meteorology, A. (2018). http://www.bom.gov.au/jsp/ncc/climate_averages/cloud/index.jsp.
- Calle, A., Casanova, J., & Romo, A. (2006a). Fire detection and monitoring using msg spinning enhanced visible and infrared imager (seviri) data. *Journal of Geophysical Research: Biogeosciences*, *111*.
- Calle, A., Casanova, J. L., Mocil??n, C., Romo, A. J., Cisbani, E., Costantini, M., Zavagli, M., & Greco, B. (2005). Latest algorithms and scientific developments for forest fire detection and monitoring using MSG/SEVIRI and MODIS sensors. *RAST 2005 - Proceedings of 2nd International Conference on Recent Advances in Space Technologies, 2005*, 118–123.

- Calle, A., Casanova, J. L., & Romo, A. (2006b). Fire detection and monitoring using MSG Spinning Enhanced Visible and Infrared Imager (SEVIRI) data. *Journal of Geophysical Research: Biogeosciences*, *111*, 1–13.
- Calle, A., González-Alonso, F., & Merino De Miguel, S. (2008). Validation of active forest fires detected by msg-seviri by means of modis hot spots and awifs images. *International Journal of Remote Sensing*, *29*, 3407–3415.
- Colditz, R. R., Llamas, R. M., Gebhardt, S., Wehrmann, T., & Equihua, J. (2015). Comparison of change detection techniques for the yucatan peninsula using landsat image time series. In *Geoscience and Remote Sensing Symposium (IGARSS), 2015 IEEE International* (pp. 1650–1653). IEEE.
- Da, C. (2015). Preliminary assessment of the Advanced Himawari Imager (AHI) measurement onboard Himawari-8 geostationary satellite. *Remote Sensing Letters*, *6*, 637–646.
- Data.gov.au (). Sentinel Hotspots - Datasets - data.gov.au.
- Dozier, J. (1981). A method for satellite identification of surface temperature fields of subpixel resolution. *Remote Sensing of Environment*, *11*, 221–229.
- Eumetsat (). TitleActive Fire Monitoring - Eumetsat.
- Feltz, J. M., Moreau, M., Prins, E. M., McClaid-Cook, K., & Brown, I. F. (2003). Recent validation studies of the GOES wildfire automated biomass burning algorithm (WF_ABBA) in North and South America. In *2nd Int. Wildland Fire Ecology Fire Management Congress, 5th Symp. Fire Forest Meteorology, Orlando, FL*.
- Freeborn, P. H., Wooster, M. J., Roberts, G., & Xu, W. (2014). Evaluating the SEVIRI fire thermal anomaly detection algorithm across the Central African Republic using the MODIS active fire product. *Remote Sensing*, *6*, 1890–1917.
- Giglio, L., Csiszar, I., Restás, Á., Morisette, J. T., Schroeder, W., Morton, D., & Justice, C. O. (2008a). Active fire detection and characterization with the advanced spaceborne thermal emission and reflection radiometer (ASTER). *Remote Sensing of Environment*, *112*, 3055–3063.
- Giglio, L., Csiszar, I., Restás, Á., Morisette, J. T., Schroeder, W., Morton, D., & Justice, C. O. (2008b). Active fire detection and characterization with the advanced spaceborne thermal emission and reflection radiometer (ASTER). *Remote Sensing of Environment*, *112*, 3055–3063.
- Giglio, L., Descloitres, J., Justice, C. O., & Kaufman, Y. J. (2003). An enhanced contextual fire detection algorithm for MODIS. *Remote Sensing of Environment*, *87*, 273–282.

- Giglio, L., Kendall, J. D., & Justice, C. (1999). Evaluation of global fire detection algorithms using simulated AVHRR infrared data. *Int. J. Remote Sensing*, *20*, 1947–1985.
- Giglio, L., Loboda, T., Roy, D. P., Quayle, B., & Justice, C. O. (2009). An active-fire based burned area mapping algorithm for the MODIS sensor. *Remote Sensing of Environment*, *113*, 408–420.
- Giglio, L., Schroeder, W., & Justice, C. O. (2016). The collection 6 MODIS active fire detection algorithm and fire products. *Remote Sensing of Environment*, *178*, 31–41.
- Goodwin, N. R., & Collett, L. J. (2014). Development of an automated method for mapping fire history captured in landsat tm and etm+ time series across queensland, australia. *Remote Sensing of Environment*, *148*, 206–221.
- Hally, B., Wallace, L., Reinke, K., & Jones, S. (2017). A broad-area method for the diurnal characterisation of upwelling medium wave infrared radiation. *Remote Sensing*, *9*, 167.
- Hally, B., Wallace, L., Reinke, K., Jones, S., & Skidmore, A. (2018). Advances in active fire detection using a multi-temporal method for next-generation geostationary satellite data. *International Journal of Digital Earth*, .
- Hantson, S., Padilla, M., Corti, D., & Chuvieco, E. (2013). Strengths and weaknesses of modis hotspots to characterize global fire occurrence. *Remote Sensing of Environment*, *131*, 152–159.
- Hayes, D. J., & Sader, S. a. (2001). Comparison of ChangeDetection Techniques for Monitoring Tropical Forest Clearing and Vegetation Regrowth in a Time Series. *Photogrammetric Engineering & Remote Sensing*, *67*, No. 9, 1067–1075.
- Hefeeda, M., & Bagheri, M. (2007). Wireless sensor networks for early detection of forest fires. In *2007 IEEE International Conference on Mobile Adhoc and Sensor Systems* (pp. 1–6).
- Ichoku, C., & Kaufman, Y. (2005). A method to derive smoke emission rates from MODIS fire radiative energy measurements. *IEEE Transactions on Geoscience and Remote Sensing*, *43*, 2636–2649.
- Ichoku, C., Kaufman, Y., Giglio, L., Li, Z., Fraser, R., Jin, J.-Z., & Park, W. (2003). Comparative analysis of daytime fire detection algorithms using avhrr data for the 1995 fire season in canada: Perspective for modis. *International Journal of Remote Sensing*, *24*, 1669–1690.
- Imai, T., & Yoshida, R. (2016). Algorithm theoretical basis for himawari-8 cloud mask product. *Meteorological Satellite Center Technical Note*, *61*, 1–17.
- Joint Remote Sensing Research Program (2012). Vegetation height and structure - derived from ALOS-1 PALSAR, Landsat and ICESat/GLAS, Australia coverage.

- Jolly, W. M., Cochrane, M. A., Freeborn, P. H., Holden, Z. A., Brown, T. J., Williamson, G. J., & Bowman, D. M. (2015). Climate-induced variations in global wildfire danger from 1979 to 2013. *Nature Communications*, *6*, 1–11.
- Justice, C. O., Giglio, L., Korontzi, S., Owens, J., Morisette, J. T., Roy, D., Descloitres, J., Alleaume, S., Petitcolin, F., & Kaufman, Y. (2002a). The MODIS fire products. *Remote Sensing of Environment*, *83*, 244–262.
- Justice, C. O., Giglio, L., Korontzi, S., Owens, J., Morisette, J. T., Roy, D., Descloitres, J., Alleaume, S., Petitcolin, F., & Kaufman, Y. (2002b). The MODIS fire products. *Remote Sensing of Environment*, *83*, 244–262.
- Karam, M. a., Amar, F., Fung, A. K., Mougin, E., Lopes, A., Le Vine, D. M., & Beaudoin, A. (1995). A microwave polarimetric scattering model for forest canopies based on vector radiative transfer theory. *Remote Sensing of Environment*, *53*, 16–30.
- Kaufman, Y. J., Justice, C. O., Flynn, L. P., Kendall, J. D., Prins, E. M., Giglio, L., Ward, D. E., Menzel, W. P., & Setzer, A. W. (1998). Potential global fire monitoring from EOS-MODIS. *Journal of Geophysical Research-Atmospheres*, *103*, 32215–32238.
- Kaufman, Y. J., & Remer, L. A. (1994). Detection of forests using mid-IR reflectance: an application for aerosol studies. *IEEE Transactions on Geoscience and Remote Sensing*, *32*, 672–683.
- Kaufman, Y. J., Tanré, D., Remer, L. a., Vermote, E. F., Chu, a., & Holben, B. N. (1997). Operational remote sensing of tropospheric aerosol over land from EOS moderate resolution imaging spectroradiometer. *Journal of Geophysical Research*, *102*, 17051.
- Koltunov, A., Ustin, S. L., & Prins, E. M. (2012). On timeliness and accuracy of wildfire detection by the goes wf-abba algorithm over california during the 2006 fire season. *Remote sensing of environment*, *127*, 194–209.
- Laneve, G., Castronuovo, M., & Cadau, E. (2006). Assessment of the Fire Detection Limit using SEVIRI/MSG Sensor. *2006 IEEE International Symposium on Geoscience and Remote Sensing*, (pp. 4157–4160).
- Longley, P., Maguire, D. J., & Rhind, D. W. (2005). *Geographical information systems and science*. (2nd ed.). Hoboken: Wiley.
- Lyon, J. G., Yuan, D., Lunetta, R. S., & Elvidge, C. D. (1998). A change detection experiment using vegetation indices. *Photogrammetric Engineering and Remote Sensing*, *64*, 143–150.

- Martell, D. L. (2007). Forest fire management. In *Handbook of operations research in natural resources* (pp. 489–509). Springer.
- Melrose, J., Perroy, R., & Careas, S. (2006). *MODIS FIRE PRODUCTS (Version. Technical Report October NASA,USA*.
- Mengod, P. C. (2015). The influence of external factors on false alarms in an infrared fire detection system. *International journal of wildland fire*, (pp. 261–266).
- Merrill, D. F., Alexander, M. E., & Others (). *Glossary of forest fire management terms.*
- Merwe, M. V. D. (2015). *An optimisation approach for assigning resources to defensive tasks during wildfires*. School of Mathematical and Geospatial Sciences, RMIT University.
- Minas, J. P. (2013). *Operations Research for Decision Support in Wildfire Management*. School of Mathematical and Geospatial Sciences, RMIT University.
- Morgan, P., Hardy, C. C., Swetnam, T. W., Rollins, M. G., & Long, D. G. (2001). Mapping fire regimes across time and space: Understanding coarse and fine-scale fire patterns. *International Journal of Wildland Fire*, *10*, 329–342.
- Morisette, J., Giglio, L., Csiszar, I., & Justice, C. (2005a). Validation of the MODIS active fire product over Southern Africa with ASTER data. *International Journal of Remote Sensing*, *26*, 4239–4264.
- Morisette, J. T., Giglio, L., Csiszar, I., Setzer, A., Schroeder, W., Morton, D., & Justice, C. O. (2005b). Validation of MODIS active fire detection products derived from two algorithms. *Earth Interactions*, *9*.
- Oliva, P., & Schroeder, W. (2015). Assessment of VIIRS 375m active fire detection product for direct burned area mapping. *Remote Sensing of Environment*, *160*, 144–155.
- Pereira, J. M. C. (1999). A comparative evaluation of NOAA/AVHRR vegetation indexes for burned surface detection and mapping. *IEEE Transactions on Geoscience and Remote Sensing*, *37*, 217–226.
- Ploscariu, I. (2018). Largest Brush and Forest Fires In Recorded History - WorldAtlas.com.
- Prins, E., & Schmetz, J. (1999). Diurnal active fire detection using a suite of international geostationary satellites. In *Proceedings of GOFW workshop (Ispra, 3–5 November 1999)* (pp. 139–148). European Commission, DG JRC Italy.
- Prins, E. M., Feltz, J. M., Menzel, W. P., & Ward, D. E. (1998). An overview of goes-8 diurnal fire and smoke results for scar-b and 1995 fire season in south america. *Journal of Geophysical Research: Atmospheres*, *103*, 31821–31835.

- Prins, E. M., & Menzel, W. P. (1994a). Trends in South American biomass burning detected with the GOES visible infrared spin scan radiometer atmospheric sounder from 1983 to 1991. *Journal of Geophysical Research: Atmospheres*, *99*, 16719–16735.
- Prins, E. M., & Menzel, W. P. (1994b). Trends in south american biomass burning detected with the goes visible infrared spin scan radiometer atmospheric sounder from 1983 to 1991. *Journal of Geophysical Research: Atmospheres*, *99*, 16719–16735.
- Prins, E. M., Schmetz, J., Flynn, L., Hillger, D., & Feltz, J. (2001). An overview of diurnal active fire monitoring using a suite of international geostationary satellites. *Global and Regional Vegetation Monitoring from Space: Planning a Coordinated International Effort*, (pp. 145–170).
- Roberts, G., Wooster, M. J., Lauret, N., Gastellu-Etchegorry, J. P., Lynham, T., & McRae, D. (2018). Investigating the impact of overlying vegetation canopy structures on fire radiative power (FRP) retrieval through simulation and measurement. *Remote Sensing of Environment*, *217*, 158–171.
- Roberts, G., Wooster, M. J., Perry, G. L., Drake, N., Rebelo, L.-M., & Dipotso, F. (2005). Retrieval of biomass combustion rates and totals from fire radiative power observations: Application to southern africa using geostationary seviri imagery. *Journal of Geophysical Research: Atmospheres*, *110*.
- Roberts, G., Wooster, M. J., Xu, W., Freeborn, P. H., & Morcrette, J. (2015). LSA SAF Meteosat FRP Products : Part 2 Evaluation and demonstration of use in the Copernicus Atmosphere Monitoring Service (CAMS). *Atmospheric Chemistry and Physics Discussions*, *15*, 15909–15976.
- Roberts, G. G. J., & Wooster, M. M. J. (2008a). Fire Detection and Fire Characterization Over Africa Using Meteosat SEVIRI. *IEEE Transactions on Geoscience and Remote Sensing*, *46*, 1200–1218.
- Roberts, G. J., & Wooster, M. J. (2008b). Fire detection and fire characterization over Africa using meteosat SEVIRI. *IEEE Transactions on Geoscience and Remote Sensing*, *46*, 1200–1218.
- Robinson, J. M. (1991). Fire from space: Global fire evaluation using infrared remote sensing. *International Journal of Remote Sensing*, *12*, 3–24.
- Roy, D., Lewis, P., Schaaf, C., Devadiga, S., & Boschetti, L. (2006). The global impact of clouds on the production of modis bidirectional reflectance model-based composites for terrestrial monitoring. *Geoscience and Remote Sensing Letters, IEEE*, *3*, 452–456.
- Roy, D. P., Boschetti, L., Justice, C. O., & Ju, J. (2008). The collection 5 MODIS burned area product - Global evaluation by comparison with the MODIS active fire product. *Remote Sensing of Environment*, *112*, 3690–3707.

- San-Miguel-Ayanz, J., Ravail, N., Kelha, V., & Ollero, A. (2005). Active fire detection for fire emergency management: Potential and limitations for the operational use of remote sensing. *Natural Hazards*, *35*, 361–376.
- Schroeder, W., Oliva, P., Giglio, L., & Csiszar, I. a. (2014). The New VIIRS 375m active fire detection data product: Algorithm description and initial assessment. *Remote Sensing of Environment*, *143*, 85–96.
- Schroeder, W., Oliva, P., Giglio, L., Quayle, B., Lorenz, E., & Morelli, F. (2015). Active fire detection using Landsat-8/OLI data. *Remote Sensing of Environment*, .
- Schroeder, W., Prins, E., Giglio, L., Csiszar, I., Schmidt, C., Morisette, J., & Morton, D. (2008a). Validation of goes and modis active fire detection products using aster and etm+ data. *Remote Sensing of Environment*, *112*, 2711–2726.
- Schroeder, W., Prins, E., Giglio, L., Csiszar, I., Schmidt, C., Morisette, J., & Morton, D. (2008b). Validation of GOES and MODIS active fire detection products using ASTER and ETM+ data. *Remote Sensing of Environment*, *112*, 2711–2726.
- Sifakis, N. I., Iossifidis, C., Kontoes, C., & Keramitsoglou, I. (2011a). Wildfire detection and tracking over Greece using MSG-SEVIRI satellite data. *Remote Sensing*, *3*, 524–538.
- Sifakis, N. I., Iossifidis, C., Kontoes, C., & Keramitsoglou, I. (2011b). Wildfire detection and tracking over Greece using MSG-SEVIRI satellite data. *Remote Sensing*, *3*, 524–538.
- Slavkovikj, V., Verstockt, S., Van Hoecke, S., & Van de Walle, R. (2014). Review of wildfire detection using social media. *Fire safety journal*, *68*, 109–118.
- Stipani, D., Štula, M., Krstini, D., Šeri, L., Jakov, T., & Bugari, M. (2010). Advanced automatic wildfire surveillance and monitoring network. *VI International Conference on Forest Fire Research*, (p. 15).
- Stoyanova, J., Georgiev, C., Yordanova, D., & Mladenov, K. (2008). Active fire monitoring over bulgaria: validation of seviri fir product. In *EUMETSAT Meteorological Satellite Conference, Darmstadt, Germany* (pp. 8–12). Citeseer.
- Tekeli, A. E., Sönmez, İ., Erdi, E., & Demir, F. (2009). Validation studies of eumetsats active fire monitoring product over turkey. *International Journal of Wildland Fire*, *18*, 517–526.
- Watts, A. C., Ambrosia, V. G., & Hinkley, E. A. (2012). Unmanned aircraft systems in remote sensing and scientific research: Classification and considerations of use. *Remote Sensing*, *4*, 1671–1692.
- Wickramasinghe, C., Wallace, L., Reinke, K., & Jones, S. (2018). Implementation of a new algorithm resulting in improvements in accuracy and resolution of seviri hotspot products. *Remote Sensing Letters*, *9*, 877–885.

- Wickramasinghe, C. H., Jones, S., Reinke, K., & Wallace, L. (2016). Development of a multi-spatial resolution approach to the surveillance of active fire lines using himawari-8. *Remote Sensing*, *8*, 932.
- Williams, R. J., Cook, G. D., Gill, a. M., & Moore, P. H. R. (1999). Fire regime, fire intensity and tree survival in a tropical savanna in northern Australia. *Australian Journal of Ecology*, *24*, 50–59.
- Williams, R. J., Gill, A. M., & Moore, P. H. R. (1998). Seasonal changes in fire behaviour in a tropical savanna in northern Australia. *International Journal of Wildland Fire*, *8*, 227–239.
- Wolfe, R. E., Lin, G., Nishihama, M., Tewari, K. P., Tilton, J. C., & Isaacman, A. R. (2013). Suomi NPP VIIRS prelaunch and on-orbit geometric calibration and characterization. *Journal of Geophysical Research Atmospheres*, *118*, 11508–11521.
- Wolfe, R. E., & Nishihama, M. (2009). Trends in MODIS geolocation error analysis. *Proceedings of SPIE*, *7452*, 74520L–74520L–7.
- Wolfe, R. E., Nishihama, M., Lin, G., Tewari, K. P., & Montano, E. (2012). MODIS and VIIRS geometric performance comparison. *International Geoscience and Remote Sensing Symposium (IGARSS)*, (pp. 5017–5020).
- Wooster, M. J., Roberts, G., Perry, G. L. W., & Kaufman, Y. J. (2005). Retrieval of biomass combustion rates and totals from fire radiative power observations: FRP derivation and calibration relationships between biomass consumption and fire radiative energy release. *Journal of Geophysical Research*, *110*, D24311.
- Wooster, M. J., Zhukov, B., & Oertel, D. (2003). Fire radiative energy for quantitative study of biomass burning: derivation from the BIRD experimental satellite and comparison to MODIS fire products. *Remote Sensing of Environment*, *86*, 83–107.
- Xu, G., & Zhong, X. (2017). Real-time wildfire detection and tracking in australia using geostationary satellite: Himawari-8. *Remote Sensing Letters*, *8*, 1052–1061.
- Xu, W., Wooster, M. J., Kaneko, T., He, J., Zhang, T., & Fisher, D. (2017). Remote Sensing of Environment Major advances in geostationary fire radiative power (FRP) retrieval over Asia and Australia stemming from use of Himarawi-8 AHI. *Remote Sensing of Environment*, *193*, 138–149.
- Yu, F., Wu, X., Shao, X., & Kondratovich, V. (2016). Evaluation of himawari-8 ahi geospatial calibration accuracy using snpp viirs sno data. In *Geoscience and Remote Sensing Symposium (IGARSS), 2016 IEEE International* (pp. 2925–2928). IEEE.